Quantitative Convergent Beam Electron Diffraction and Charge Density Studies

by

Jesper Friis

Thesis submitted in partial fullfillment of the requirements for the Norwegian academic degree of Doktor Ingeniør

Department of Physics
Norwegian University of Science and Technology
Trondheim, Norway

November 2003

URN:NBN:no-7231

Source: The CBED art works gallery at Tanaka's group,
`http://xes.tagen.tohoku.ac.jp/gallery/thestarrynight.html`

URN:NBN:no-7231

Summary

Very accurate low-order structure factors have been measured in copper, magnesium and strontium titanate using quantitative convergent beam electron diffraction (QCBED). The charge density distribution in these materials has been studied using the measured structure factors. The results have also been compared to *ab initio* density functional theory (DFT) calculations.

In the case of copper, we combined our low-order structure factors with higher order γ-ray structure factors, in order to obtain a larger experimental data set for maximum entropy and multipole analysis. The results show that bond formation induces a large change in the $3d$ orbital radial function. As expected for metallic bonding, no asphericity of the orbitals has been observed. These results are in perfect agreement with DFT calculations.

For magnesium it was shown that the anisotropic displacement parameters could be determined accurately from the low order QCBED data, if structure factors from DFT calculations were used as a static lattice reference. This data set was combined with X-ray structure factor measurements and used to test some commonly used DFT functionals and self interaction correction (SIC) schemes. It was found that the local density approximation combined with the SIC of Lundin and Eriksson (2001) gave the best agreement with experiments. Using this functional no non-nuclear maximum was found in beryllium, but not in magnesium.

URN:NBN:no-7231

URN:NBN:no-7231

Preface

This thesis is the result of more than three and a half years studies at Department of Physics at the Norwegian University Science and Technology (NTNU). It can be seen as a continuation of the long tradition in Trondheim, established by Prof. Ragnvald Høier (Department of Physics, NTNU) and continued by Prof. Knut Marthinsen (now Department of Materials Technology, NTNU) and Prof. Randi Holmestad (Department of Physics, NTNU), to use convergent beam electron diffraction for accurate structure factor determination and charge density studies.

During this thesis I have visited Arizona State University (ASU) twice, first six months in spring 2001 and later one month in April 2002. Together with Dr. Bin Jiang's (Department of Physics and Astronomy, ASU) visits here in Trondheim (October 2001 and November 2002), these have been the most productive periods of the thesis.

This work is divided into four parts:

The first part is an introduction to quantitative convergent beam electron diffraction and methods for studying the charge density using experimentally derived structure factors. These methods include direct Fourier synthesis, multipolar modeling and maximum entropy. A brief description of density functional theory is also included in chapter 3.

The second and main part contains the papers:

Paper 1: *Quantitative Convergent Beam Electron Diffraction Measurements of Low Order Structure Factors in Copper*
J. Friis, B. Jiang, J. C. H. Spence and R. Holmestad.
Microscopy and Microanalysis. 9, 379-389. 2003.

Paper 2: *On the Consistency of QCBED structure factor measurements for TiO_2 (Rutile)*
B. Jiang, J. M. Zuo, J. Friis and J. C. H. Spence.
Microscopy and Microanalysis. 9, 457-467. 2003.

Paper 3: *Retrieval of anisotropic displacement parameters in Mg from convergent beam electron diffraction*
J. Friis, K. Marthinsen and R. Holmestad.
EMAG Proceedings 2003. Inst. Phys. Conf. Ser. No. 165.
In press.

Paper 4: *Magnesium: Comparison of Density Functional Theory Calculations with Electron and X-ray Diffraction Experiments*
J. Friis, G. K. H. Madsen, F. K. Larsen, B. Jiang, K. Marthinsen and

R. Holmestad.
In press, Journal of Chemical Physics. Expected in Vol 119, No. 21, December 2003.

Paper 5: *A Study of Charge Density in Copper*
J. Friis, B. Jiang, K. Marthinsen and R. Holmestad.
Aimed for Acta Cryst. A.

Paper 6: *Electron Density and Implication for Bonding in Cu and Ag*
B. Jiang, J. Friis, R. Holmestad, J. M. Zuo, M. O'Keeffe and J. C. H. Spence.
Submitted to Phys. Rev. B.

Paper 1, 5, and 6 are based on experiments on copper performed during my visit at ASU the spring 2001. My contribution to paper 2 is limited to the generation of figure 6. Paper 3 and 4 are based on experiments on magnesium during my second visit to ASU, April 2002.

After the papers follows a short chapter on the unpublished and unfinished results on strontium titanate.

Finally two appendices are included, one containing a derivation of the Mott formula and another containing derivation of formulas for error analysis of the experimental structure factors.

Acknowledgements

First of all I want to thank my supervisors Randi Holmestad and Knut Marthinsen for assistance, many clarifying discussions and their always good mood. Their overview, especially in dynamical diffraction theory, has been of great help. Randi was the driving force for my visits to ASU, on which all the published results are based. I also want to thank John Spence, who welcomed me in his group during my visits at ASU.

I also really want to thank Bin Jiang, who learned me everything I know about operating a transmission electron microscope, and has been an invaluable collaborator, teacher, and friend. The discussions with Jian Min Zuo (Department of Materials Science and Engineering, University of Illinois at Urbana-Champaign) have also been of great help.

The collaboration with Georg Madsen and Finn Krebs Larsen at Århus University resulted in my probably most important article, Paper 4. Many thanks to both for giving me the chance to work with them, and for their generosity. I am also grateful to Morten and Maria Fredriksen for welcoming me home whenever I visited Aarhus University and to Frode Mo, who suggested the contact.

Thanks to Vladimir Tsirelson (Mendeleev University of Chemical Technology, Moscow) and Kåre Olaussen for an interesting discussion which resulted in appendix A.

Thanks to the TEM group for their friendship and to Nils Sandberg and Rasmus Jansson for reading through this manuscript.

Above all I want to thank my always patient wife, Kris. Thanks also for reading through the manuscript and for your very inspiring illustrations.

The Norwegian Research Council (NFR), project 135270/410, is gratefully acknowledged for financial support and additional grants for the stay at ASU.

Jesper Friis
Trondheim, November 11, 2003

URN:NBN:no-7231

Contents

Part I

Introduction and background to quantitative convergent beam electron diffraction and charge density studies

URN:NBN:no-7231

URN:NBN:no-7231

Chapter 1

Introduction

The aim of this work has been to investigate theoretically and experimentally, different methods and aspects of the determination of charge density and bonding by convergent beam electron diffraction (CBED). This work is motivated by the fact that an increased knowledge of the microscopic properties, such as bonding and charge distribution, is required to design and use new and advanced materials.

Traditionally electron microscopy has been a qualitative science both for imaging and diffraction. A lot of information about crystal symmetry and crystal structure can be derived from the position of the diffraction spots. The first convergent beam electron diffraction pattern was produced already in 1937 by Kossel & Möllenstedt (1939) in order to further investigate the newly discovered Kossel and Kikuchi patterns seen in X-ray diffraction experiments. With the development of the dynamical theory in the 1950s and 1960s, it became clear that dynamical effects have to be taken into account in order to explain effects such as the occurrence of forbidden reflections (Gjønnes & Moodie, 1965) and small shifts in the Kikuchi-line positions (Uyeda, 1968; Høier, 1969; Gjønnes & Høier, 1971). Quantitative measurements of structure factors started in the early 1980s (Voss *et al.*, 1980), taking not only the position of the features in the diffraction pattern into account, but also the exact intensities. Shortly after, phase measurements of the structure factors for non-centrosymmetric crystals were also performed (Taftø & Spence, 1982; Taftø, 1983; Marthinsen & Høier, 1986, 1988). The use of energy filters, CCD cameras/image plates and the increase of computer power during the 1990s have greatly increased the accuracy and made convergent beam electron diffraction an accurate tool for measuring the low order structure factors in small unit-cell crystals (e.g. Zuo, 1993; Saunders *et al.*, 1993; Holmestad *et al.*, 1995; Høier *et al.*, 1993; Tsuda & Tanaka, 1995; Deininger *et al.*, 1995; Saunders *et al.*, 1996; Zuo *et al.*, 1997; Birkeland *et al.*, 1997;

Nüchter *et al.*, 1998; Saunders *et al.*, 1999; Holmestad *et al.*, 1999; Zuo, 1999; Jiang *et al.*, 2003).

The new challenge is to combine the low order structure factors from quantitative CBED with higher order structure factors from X-ray diffraction, in order to obtain a better description of the charge density (Zuo *et al.*, 1999; Streltsov *et al.*, 2001) and to test band theory (Zuo *et al.*, 1997; Friis *et al.*, 2003).

References

Birkeland, C. R., Høier, R., Holmestad, R. & Marthinsen, K. (1997). A convergent beam method for determination of structure factor phases and amplitudes from center disk intensity. In *Proc. Microscopy and Microanalysis*, 133–136.

Deininger, C., Mayer, J. & Ruehle, M. (1995). Determination of the charge density distribution of crystals by energy filtered CBED. *Optik* **99**, 135–140.

Friis, J., Madsen, G. K. H., Larsen, F. K., Jiang, B., Marthinsen, K. & Holmestad, R. (2003). Magnesium: Comparison of density functional theory calculations with electron and X-ray diffraction experiments. *J. Chem. Phys.* **119**. In press. Paper 4 in this thesis.

Gjønnes, J. & Høier, R. (1971). The application of non-systematic many-beam dynamic effects to structure factor determination. *Acta Cryst. A* **24**, 313–316.

Gjønnes, J. & Moodie, A. F. (1965). Extinction conditions in the dynamic theory of electron diffraction. *Acta Cryst. A* **19**, 65–67.

Høier, R. (1969). A method to determine the ratio between lattice parameter and electron wavelength from Kikuchi line intersections. *Acta Cryst. A* **25**, 516–518.

Høier, R., Bakken, L. N., Marthinsen, K. & Holmestad, R. (1993). Structure factor determination in non-centrosymmetric crystals by a two-dimensional CBED-based multi-parameter refinement method. *Ultramicroscopy* **49**, 159–170.

Holmestad, R., Birkeland, C., Marthinsen, K., Høier, R. & Zuo, J. M. (1999). Use of quantitative convergent beam electron diffraction in materials science. *Microscopy Research and Technique* **46**, 130–145.

Holmestad, R., Zuo, J. M., Spence, J. C. H., Høier, R. & Horita, Z. (1995). Effect of Mn on charge density in γ-TiAl by quantitative convergent beam electron diffraction. *Philos. Mag. A* **72**, 579–601.

Jiang, B., Zuo, J. M., Jiang, N., O'Keeffe, M. & Spence, J. C. H. (2003). Charge density and chemical bonding in rutile (TiO_2). *Acta Cryst. A* **59**, 341–350.

Kossel, W. & Möllenstedt, G. (1939). Elektroneninterferenzen im konvergenten. *Ann. Phys.* **36**, 113–140.

Marthinsen, K. & Høier, R. (1986). Many-beam effects and phase information in electron channelling patterns. *Acta Cryst. A* **42**, 484–492.

Marthinsen, K. & Høier, R. (1988). Determination of structure-factor phase invariants and effective structure factors in non-centrosymmetric crystals. *Acta Cryst. A* **44**, 558–562.

Nüchter, W., Weickenmeier, A. L. & Mayer, J. (1998). High-precision measurement of temperature factors for NiAl by convergent-beam electron diffraction. *Acta Cryst. A* **54**, 147–157.

Saunders, M., Bird, D. M., Holbrook, O. F., Midgley, P. A. & Vincent, R. (1996). The use of Bethe potentials in zone-axis CBED pattern matching. *Ultramicroscopy* **65**, 45–52.

Saunders, M., Bird, D. M., Zaluzec, N. J., Burgess, W. G. & Humphreys, C. J. (1993). Accurate structure factor refinement from zone-axis CBED patterns. In *Inst. Phys. Conf. Ser.*, 138, 125–128.

Saunders, M., Fox, A. G. & Midgley, P. A. (1999). Quantitative zone-axis convergent-beam electron diffraction (CBED) studies of metals. I. structure-factor measurements. *Acta Cryst. A* **55**, 471–479.

Streltsov, V. A., Nakashima, P. N. H. & Johnson, A. W. S. (2001). Charge density analysis from complementary high energy synchrotron X-ray and electron diffraction data. *J. Phys. Chem. Solids* **62**, 2109–2117.

Taftø, J. (1983). Structure-factor phase information from two-beam electron diffraction. *Phys. Rev. Lett.* **51**, 654–657.

Taftø, J. & Spence, J. C. H. (1982). A simple method for the determination of structure-factor phase relationships and crystal polarity using electron diffraction. *J. Appl. Cryst.* **15**, 60–64.

Tsuda, K. & Tanaka, M. (1995). Refinement of crystal structure parameters using convergent-beam electron diffraction: the low-temperature phase of $SrTiO_3$. *Acta Cryst. B* **51**, 942–951.

Uyeda, R. (1968). Dynamical effects in high-voltage electron diffraction. *Acta Cryst. A* **24**, 175–181.

Voss, R., Lehmpfuhl, G. & Smith, P. J. (1980). Influence of doping on the crystal potential of silicon investigated by the convergent beam electron diffraction technique. *Naturforsch. A* **35**, 973–984.

Zuo, J. M. (1993). Automated structure-facor refinement from convergent-beam electron diffraction patterns. *Acta Cryst. A* **49**, 429–435.

Zuo, J. M. (1999). Accurate structure refinement and measurement of crystal charge distribution using convergent beam electron diffraction. *Microscopy Research and Technique* **46**, 220–233.

Zuo, J. M., Blaha, P. & Schwarz, K. (1997). The theoretical charge density silicon: Experimental testing of exchange and correlation potentials. *J. Phys.: Condens. Matter* **9**, 7541–7561.

Zuo, J. M., Kim, M., O'Keeffe, M. & Spence, J. C. H. (1999). Direct observation of d-orbital holes and Cu-Cu bonding in Cu_2O. *Nature* **401**, 49–52.

Chapter 2

Quantitative electron diffraction

This chapter is intended to introduce the reader to the quantitative electron diffraction (QED) theory needed for the papers following in Part II. A simple and general introduction to electron microscopy is given by Williams & Carter (1996). For an overview of the electron diffraction theory, the excellent review by Humphreys (1979) is recommended. A complete and very good introduction to quantitative convergent beam electron diffraction (QCBED) is given in Spence & Zuo (1992).

2.1 Electron diffraction

In transmission electron microscopy, a beam of (high-energy) electrons is sent through the specimen, with which the electrons interact, and is recorded on the other side. All modern transmission electron microscopes (TEMs) have two main modes, an imaging (or microscopy) mode, and a diffraction mode. In the image mode, the recorded pattern shows the projection of the spatial distribution of the scattering, while in the diffraction mode, the recorded pattern shows the angular distribution of the scattering. One of the great advantages of TEM, e.g. compared to X-ray diffraction, is the possibility to easily switch between these modes.

In "ordinary" parallel beam electron diffraction, the diffraction patterns consist of bright spots (see Fig. 2.2a), corresponding to beam directions that satisfy the well known Bragg's law

$$2d' \sin\theta_B = n\lambda \tag{2.1}$$

where d' is the spacing between lattice planes, θ_B is the Bragg angle, n is

an integer and λ is the electron wave length. However, it is convenient to introduce $d = d'/n$ which simplifies Bragg's law to

$$2d \sin\theta_B = \lambda \tag{2.2}$$

and to regard this as first order reflections from planes with spacing $d = d'/n$. The quantity $s = \sin\theta/\lambda$ is often referred to as the scattering angle. From Bragg's law it follows that $s = |\mathbf{g}|/2$ at the Bragg angle, where $\mathbf{g}$ is a reciprocal lattice vector corresponding to the planes d, with $|\mathbf{g}| = 1/d$.

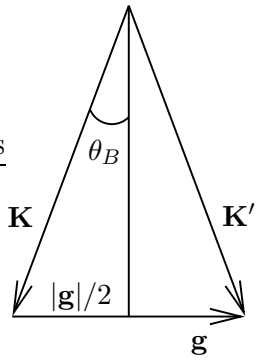

Figure 2.1: Relation between Bragg's law and the Laue condition.

Another condition for diffraction maximum, which is more suitable for quantitative work, is the *Laue condition*

$$\mathbf{K}' - \mathbf{K} = \mathbf{g}, \tag{2.3}$$

where $\mathbf{K}$ and $\mathbf{K}'$ are the incident and diffracted beams respectively. By assuming elastic scattering $|\mathbf{K}'| = |\mathbf{K}|$, Bragg's law (2.2) follows immediately, with the Bragg angle θ_B defined in Fig. 2.1.

2.2 Convergent beam electron diffraction

The principles of CBED are the same as for ordinary selected area diffraction (SAD), but instead of using a parallel beam, the electron probe is focused onto the specimen. As seen in Fig. 2.2, this causes the spots to broaden out into disks. Each incident beam direction (e.g. a in Fig. 2.3) gives rise to a complete diffraction pattern, with one diffraction spot a' contributing to each CBED disk. Thus, if an incoherent electron source is used, such as a LaB_6 filament, the CBED pattern can be seen as a superposition of independent diffraction patterns with different incident directions. For coherent sources, such as a field electron gun (FEG), one has to account for interference phenomena in the regions where the disks overlap (Zuo & Spence, 1993).

Figure 2.4 shows a CBED pattern tilted away from the major zone axis, to a position where the $(\bar{1}0\bar{1})$ and (101) reflections satisfy the Bragg condition along the lines pointed out in the figure. This is called a systematic row orientation. Three reflections, $(0\bar{3}\bar{1})$, $(1\bar{3}0)$ and $(2\bar{3}1)$, in the first order Laue zone (FOLZ), are also visible. At incident beam angles satisfying the Bragg conditions for these three reflections, intensity is scattered away from the

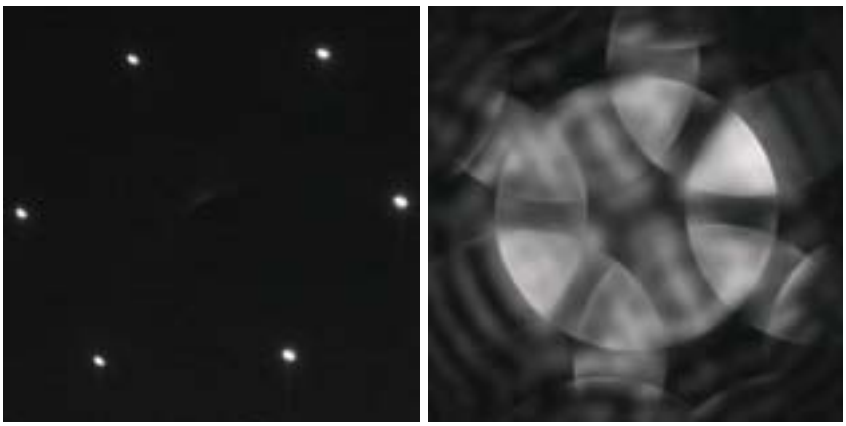

(a) (b)

Figure 2.2: Parallel (a) versus convergent beam (b) electron diffraction patterns of the [101] zone in Mg. In the SAD pattern (a) the direct beam is blocked in order to protect the CCD camera. *April 5, 2002.*

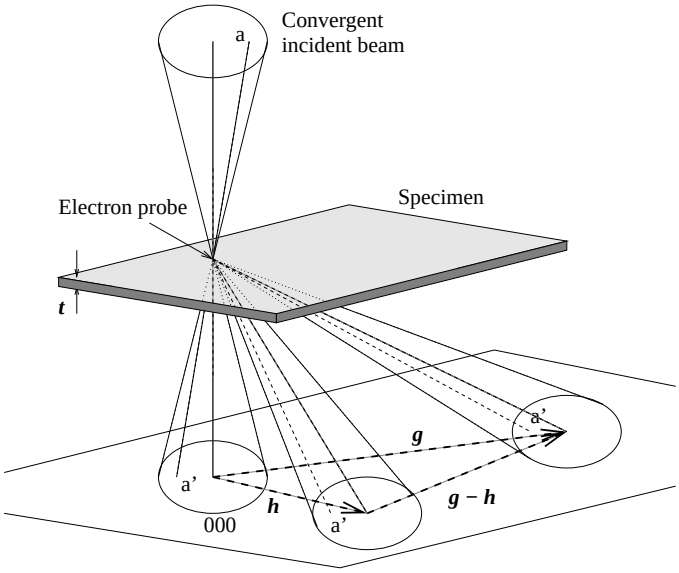

Figure 2.3: Schematic drawing of CBED. The CBED pattern is a superposition of diffraction patterns with slightly different incident beam directions. A CBED pattern is hence an image of the intensity variation as a function (called rocking curve) of incident beam direction.

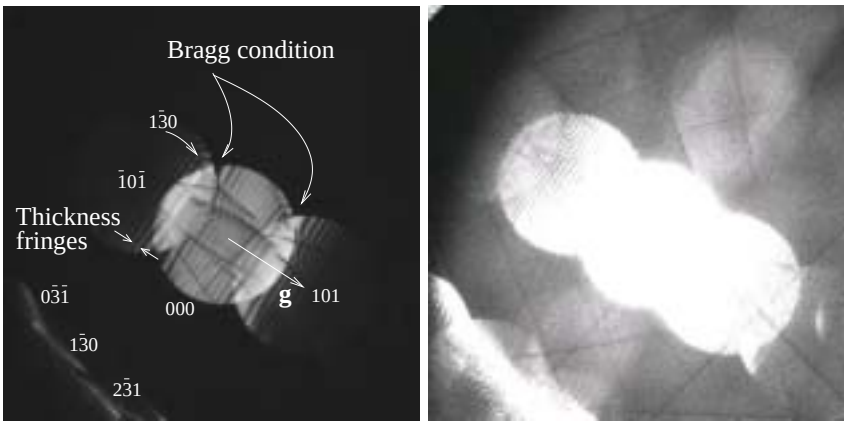

(a) (b)

Figure 2.4: CBED pattern of Mg in a symmetric (101) systematic row orientation. In (b) the low-count pixels of the pattern (a) are shown, making the Kikuchi line visible. See the text for a discussion of the features. *April 9, 2002.*

center disk to corresponding reflections. The dark FOLZ-line, corresponding to the (1$\bar{3}$0) reflection, is marked in figure 2.4a. From kinematic theory, one would expect this to be a straight line, like all the other thin dark lines visible in the center disk, but because of strong dynamical coupling between the (1$\bar{3}$0) and (2$\bar{3}$1) reflections, the line seems to split up and bend where it crosses the (2$\bar{3}$1) FOLZ-line. The position of the high order Laue zone (HOLZ)-lines, which are not strongly coupled to other lines, is easily determined from the incident beams $\mathbf{K}$ satisfying the Laue condition for reflection $\mathbf{g}$. For elastically scattered electrons[1], the absolute value of the scattered beam $|\mathbf{K}'| = |\mathbf{K} + \mathbf{g}|$ equals the absolute value of the incident beam $|\mathbf{K}|$, i.e.

$$\mathbf{K}^2 = |\mathbf{K}'|^2 = |\mathbf{K} + \mathbf{g}|^2 \tag{2.4}$$

from which it follows that

$$\mathbf{K} \cdot \mathbf{g} = -\mathbf{g}^2/2. \tag{2.5}$$

Since the amplitude $|\mathbf{K}| = 1/\lambda$ is fixed, this equation defines a circle of incident beams $\mathbf{K}$ making an angle of $90^\circ - \theta_B$ with the lattice vector $\mathbf{g}$, as illustrated in Fig. 2.5. The position of the HOLZ-lines corresponds to the projection of this ring onto the zero order Laue zone (ZOLZ)-plane (plane

[1]Thermal diffuse scattering (TDS) can also be regarded as nearly elastic, since the loss in energy (up to 0.1 eV) is much smaller than the beam energy. This is the reason why Kikuchi-lines just continue the HOLZ-lines outside the disk.

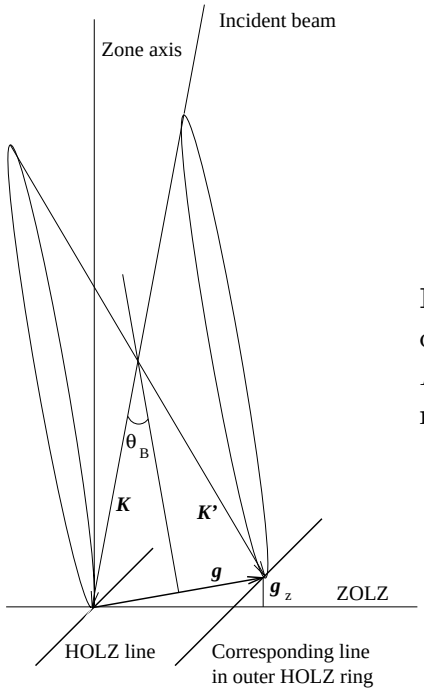

Figure 2.5: Geometry of HOLZ lines. The two cones define all incident K and diffracted beams K', which satisfies the Bragg condition for the reflection **g**.

perpendicular to the zone axis). For high-energy electrons, the HOLZ-lines appear straight since the radius of the cone is very large (λ is very small).

From Fig. 2.4b one sees that the HOLZ-lines continue out of the CBED disks. These lines, called Kikuchi-lines, are due to elastic scattering of inelastic scattered electrons. They are very useful for an initial determination of the crystal orientation.

The last important feature seen in Fig. 2.4a is the thickness fringes. These too have a dynamical origin and the distance between them is closely related to the crystal thickness (see Eq. 2.15). The thicker the crystal, the closer are the fringes.

Together with the huge amount of information, the most important advantage of CBED is the small probe size, typically 10 nm in a conventional TEM, and down to a few Ångström in a microscope with a FEG source. The small probe, combined with the image mode, makes it easy to find a perfect crystalline region of the specimen for the CBED experiment.

Because of the strong interaction between the incoming electrons and the crystal, multiple scattering occurs, despite the small sample thickness (500–2000 Å). Hence, dynamical theory is required when calculating the intensities in the CBED pattern. Since the scattering comes from a single-crystalline region, it is possible to use the Bloch-wave method (described in more detail in Section 2.3) resulting in very accurate simulations. This is the same

technique as is used in the X-ray Pendellösung method. However, the X-ray Pendellösung method is limited to very few materials, such as Si and diamond, for which large single crystals can be produced.

Since normal X-ray diffraction (not Pendellösung) utilizes kinematic theory, there will be problems with extinction (dynamical effects) for the strong low order reflections. However, these are exactly the reflections that can be measured with QCBED. Hence X-ray and QCBED can be seen as complementary techniques and their combination has proven very successful (Zuo *et al.*, 1999; Friis *et al.*, 2003b).

2.3 Dynamical intensities

There are two common methods for simulation of electron diffraction intensities, the Bloch-wave and the multi-slice method. For perfect crystals with relatively small unit cells, the Bloch-wave method is preferable because of its accuracy.

Since the exchange and correlation between the beam and crystal electrons can be neglected for high energy electrons (Rez, 1978), the propagation of an incident electron is described by the time-independent Schrödinger equation

$$\left(-\frac{h^2}{8\pi^2 m}\nabla^2 - |e|V(\mathbf{r})\right)\Psi = |e|E\Psi \tag{2.6}$$

where $V(\mathbf{r})$ is the crystal potential (in units of Volts) and $-E$ is the acceleration voltage. For a periodic potential

$$V(\mathbf{r}) = \sum_{\mathbf{g}} V_{\mathbf{g}}\, \mathrm{e}^{2\pi i \mathbf{g}\cdot\mathbf{r}} \tag{2.7}$$

equation (2.6) has the Bloch-wave solution

$$\Psi(\mathbf{r}) = \sum_{j} c^{(j)}\, \mathrm{e}^{2\pi i \mathbf{k}^{(j)}\cdot\mathbf{r}} \sum_{\mathbf{g}} C_{\mathbf{g}}^{(j)}\, \mathrm{e}^{2\pi i \mathbf{g}\cdot\mathbf{r}} \tag{2.8}$$

where $k^{(j)}$ is the wave-vector of the jth Bloch-wave and $\mathbf{g}$ is a reciprocal lattice vector. Substitution of Eq. (2.7) and (2.8) back into Eq. (2.6) yields the standard dispersion equation for high-energy electron diffraction

$$\left[\mathbf{K}^2 - (\mathbf{k}^{(j)} + \mathbf{g})^2\right] C_{\mathbf{g}}^{(j)} + \sum_{\mathbf{h}\neq\mathbf{g}} U_{\mathbf{h}-\mathbf{g}} C_{\mathbf{h}}^{(j)} = 0 \tag{2.9}$$

where we have introduced the electron structure factor

$$U_{\mathbf{g}} = \frac{2m|e|}{h^2} V_{\mathbf{g}}. \tag{2.10}$$

The amplitude of the incident beam wave-vector is related to the acceleration voltage by $\mathbf{K}^2 = 2m|e|(E+V_0)/h^2$ where V_0 is the mean inner potential. Even though V_0 is a very small quantity (around 5-25 V depending on material) compared to E (120 kV in the microscope used for the experiments in this thesis) it is not negligible (Friis *et al.*, 2003a).

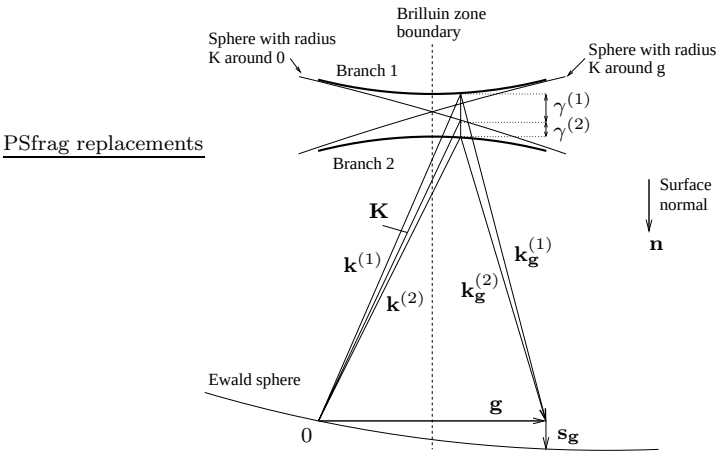

Figure 2.6: Two-beam dispersion surface construction, showing the quantities $\gamma^{(j)}$, $\mathbf{k}^{(j)}$, etc... The dispersion surface shows the allowed $\mathbf{k}$ vectors inside the crystal for a given electron beam energy.

It follows from continuity of $\Psi(\mathbf{r})$ at the entrance surface of the crystal, that the tangential components of $\mathbf{k}^{(j)}$ must equal the tangential components of $\mathbf{K}$, which can be expressed as $\mathbf{k}^{(j)} = \mathbf{K} + \gamma^{(j)}\mathbf{n}$, where $\mathbf{n}$ is the normal vector of the surface and the coefficient $\gamma^{(j)}$ is known as the *Anpassung*. Some of these quantities are shown for the two beam case in Fig. 2.6. Since backward scattering can be neglected for high energy electrons (Hirsch *et al.*, 1977), Eq. (2.9) can, after renormalization (Metherell, 1975) and assuming that the beam is nearly antiparallel to the entrance surface, be simplified to

$$2KS_\mathbf{g}C_\mathbf{g}^{(j)} + \sum_\mathbf{h} U_{\mathbf{g}-\mathbf{h}}C_\mathbf{h}^{(j)} = 2K_n\gamma^{(j)}C_\mathbf{g}^{(j)}, \tag{2.11}$$

where $S_\mathbf{g}$ is the deviation from the Bragg condition and $K_n = \mathbf{K}\cdot\mathbf{n}$ (Spence & Zuo, 1992). This is an eigenvalue problem, with eigenvalues $2K_n\gamma^{(j)}$ and eigenvector matrix $\mathbf{C}$. Because of continuity, no reflected beams can be excited at the entrance surface, leading to a condition $\sum_j c^{(j)}C_0^{(j)} = 1$ for the excitation coefficient $c^{(j)}$ of the jth Bloch-wave.

The diffraction intensities are given by the wave function at the exit surface. The intensity in a point specified by the incident beam $\mathbf{K}$ in disk $\mathbf{g}$

is given by

$$I_{\mathbf{g}}(\mathbf{K}) = |\Psi|^2 = \left| \sum_j C_0^{(j)} C_{\mathbf{g}}^{(j)*} \, \mathrm{e}^{2\pi i \gamma^{(j)} t} \right|^2 \tag{2.12}$$

where t is the thickness of the crystal.

Absorption can be included in a phenomenological way, by introducing a complex component to the crystal potential

$$V(\mathbf{r}) \rightarrow V(\mathbf{r}) + iV'(\mathbf{r}) \tag{2.13}$$

leading to a damping

$$\mathbf{k}^{(j)} \rightarrow \mathbf{k}^{(j)} + i\mathbf{q}^{(j)} \quad \text{and} \quad c^{(j)} \rightarrow c^{(j)} \, \mathrm{e}^{-2\pi i \mathbf{q}^{(j)} t} \tag{2.14}$$

of the intensity. From the Fourier transform of $V(\mathbf{r})$ and $V'(\mathbf{r})$ one obtains the, in general complex, electron structure factor $U_{\mathbf{g}}$, and absorption $U'_{\mathbf{g}}$, respectively.

If there is only one strongly exited beam ($\mathbf{g}$) beside the direct beam (0) (the so called *two beam condition*), it is easy to solve Eq. (2.11) analytically, resulting in the intensities

$$I_{\mathbf{g}}(\mathbf{K}) = 1 - I_0(\mathbf{K}) = \frac{|U_{\mathbf{g}}|^2 \sin^2\left(\pi t / K \sqrt{K^2 S_{\mathbf{g}}^2 + |U_{\mathbf{g}}|^2}\right)}{K^2 S_{\mathbf{g}}^2 + |U_{\mathbf{g}}|^2}. \tag{2.15}$$

This equation explains the oscillating "thickness fringes", seen in Fig. 2.4, when we move away from the Bragg condition. It also tells us that the intensity will oscillate with thickness variations. These simple observations are still valid, though more complicated, in the general n-beam condition.

2.4 Structure factor refinement

There exist several approaches for structure factor determination by QED (see Holmestad 1994, page 22 for an overview). For QCBED there are two main approaches, one using zone-axis patterns (Bird & Saunders, 1992a,b) and one using the systematic row orientation (Zuo & Spence, 1991). Both techniques can provide low order structure factors accurate enough for bonding studies. The zone-axis approach has the advantage that the diffraction patterns are easy to index and a lot of structure factors can be refined from a single experimental pattern. However, the computation might be more difficult since more parameters have to be refined and the patterns contain

a lot of HOLZ-lines, that are affected by the temperature factor[2] and lattice parameters. In the systematic row orientation, on the other hand, the specimen is tilted to a position with only a few strongly excited reflections. This makes the intensity around the Bragg position very sensitive to the corresponding structure factor. In addition it is possible to find regions with only few HOLZ-lines, reducing the problems with the temperature factor. In this work the systematic row approach has been used. The experimental setup and the importance of energy filtering and deconvolution of the point spread function are covered in Paper 1 and 4. More details are found in Zuo (1999).

2.4.1 The least square procedure

The EXTAL program by Zuo (1998) has been used for all structure factor refinements presented in this thesis. It follows the ideas of Goodman & Lehmpfuhl (1967), Voss *et al.* (1980) and Gjønnes *et al.* (1988), but has developed into an advanced algorithm for refining high voltage, lattice parameter, and structure factors. In short one chooses pixels along lines for which the intensity is extra sensitive to the parameters one wants to determine (see Fig. 2.7 and Friis *et al.* 2003b). A set of refined parameters (structure factors, absorption, thickness, beam direction, etc...) are varied until a best fit is obtained between the calculated and the experimental intensities. The SIM-

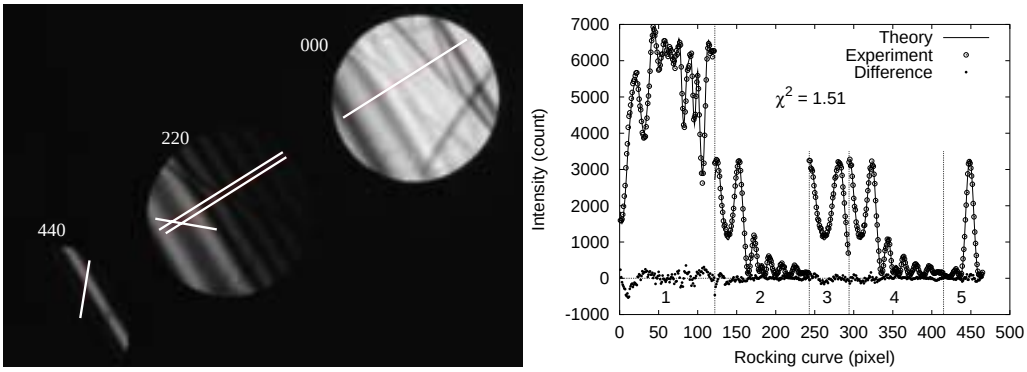

(a) (b)

Figure 2.7: (a) A CBED pattern of the (220) systematic row in copper. The line scans, along which pixels are compared with theory are marked. (b) Plot of pixel intensities for the best fit between calculation and experiment. *By B. Jiang, Sep. 2001.*

[2]This can, on the other hand, be used for measuring the temperature factor (Saunders *et al.*, 1999).

PLEX algorithm of Nelder & Mead (1965) is used for the minimization in EXTAL. This seems to give a good balance between robustness and efficiency.

If one removes outlier pixels arising from X-rays striking the CCD-camera, the errors can be assumed to be normal-distributed (see Zuo 1999 for a discussion). Hence a χ^2 test may be used as a goodness-of-fit criterion

$$\chi^2 = \frac{1}{n-p-1} \sum_{i=1}^{n} \frac{\left| I_i^{\mathrm{obs}} - cI_i^{\mathrm{calc}} - I^{\mathrm{bgr}} \right|^2}{\sigma_i^2}. \tag{2.16}$$

Here I_i^{calc} and I_i^{obs} are the calculated and observed intensities for pixel i while I^{bgr} is a refined background intensity, which is assumed constant for each disk (Saunders & Bird, 1995). n is the number of pixels, p the number of refined parameters and c a refined factor, which scales the calculated intensity to counts. Ideally χ^2 should be very close to one, provided normal-distributed errors and that correct values are used for the standard deviation of the intensities σ_i.

In order to ensure convergence of the refinement procedure, good starting values for the refined parameters must be chosen. First the thickness, which is a trivial but important parameter, and the incident beam direction have to be estimated. The beam direction is usually estimated by visually comparing the experimental Kikuchi- and HOLZ-line pattern with kinematic calculations (Zhu & Zuo, 1994). The absorption is estimated using the ATOM subroutine of Bird & King (1990), even though better routines are available nowadays (Weickenmeier & Kohl, 1991, 1998).

The initial structure factors can either be taken from density functional theory (DFT) calculations, or be calculated from the electron scattering factor as

$$U_{\mathbf{g}} = \frac{2m|e|}{h^2} \frac{1}{\Omega} \sum_j f_j^{\mathrm{e}}(s) T_j(\mathbf{s})\, \mathrm{e}^{-2\pi i \mathbf{g}\cdot\mathbf{r}_j}, \tag{2.17}$$

where f_j^{e} is related to the X-ray scattering factor (via Eq. A.7), for which good extrapolations to Hartree-Fock calculations exist (Doyle & Turner, 1968; Su & Coppens, 1997). In either case, the atomic temperature factor $T_j(\mathbf{s})$ at the experimental temperature also has to be estimated. It is important to get a good estimation of the displacement parameters[3] (DPs), since all the non-refined structure factors depend on them.

[3] $T_j(\mathbf{s})$ is in the harmonic approximation given by $T_j(\mathbf{s}) = \exp(-2\pi\langle u^i u^k\rangle_j\, g_i g_k)$, where the elements of the atomic displacement tensor $\langle u^i u^k\rangle_j$ are the anisotropic DPs. Summation over repeated indices is assumed. In the isotropic case this equation reduces into $T_j(s) = \exp(-B_j s^2)$, where $B_j = 8\pi^2\langle u^2\rangle_j$ is known as the Debye-Waller factor in the electron microscopy literature. However, this name is not recommended according to a commission on nomenclature sat down by IUCr (Trueblood *et al.*, 1996).

Good isotropic estimates for the DPs can in many cases be obtained from analytical fits to phonon density-of-state calculations (Sears & Shelley, 1991). A problem with this approach, as well as using X-ray or neutron diffraction results, is that the exact temperature of the specimen is unknown. A better method is therefore to determine the DPs directly from the CBED data (Holmestad *et al.*, 1993; Nüchter *et al.*, 1998; Saunders *et al.*, 1999; Friis *et al.*, 2003c).

2.4.2 Beam selection and Bethe perturbation

Since Eq. (2.11) has to be solved for each pixel along the chosen line scans, one has to limit the number of beams included in the diagonalization. This is solved by only including the strongest beams in the diagonalization (~ 50), and treating the rest of the non-negligible beams by perturbation (~ 300). See Zuo & Weickenmeier (1995) and Birkeland *et al.* (1997) for a discussion of beam selection criteria. Using the effective Bethe potential, the following perturbations of the eigenvalue system (2.11) can be derived (Spence & Zuo, 1992)

$$\begin{aligned} U_{\mathbf{g}}^{\text{eff}} &= U_{\mathbf{g}} \left(1 - \sum_{\mathbf{h}} \frac{U_{\mathbf{g}-\mathbf{h}} U_{\mathbf{h}}}{2KS_{\mathbf{h}} U_{\mathbf{g}}} \right) \\ 2KS_{\mathbf{g}}^{\text{eff}} &= 2KS_{\mathbf{g}} - \sum_{\mathbf{h}} \frac{U_{\mathbf{g}-\mathbf{h}} U_{\mathbf{h}-\mathbf{g}}}{2KS_{\mathbf{h}}} \end{aligned} \tag{2.18}$$

that are caused by dynamical interaction between the strong beam $\mathbf{g}$ and the weak beams $\mathbf{h}$. Eq. 2.18 is used in EXTAL with the beam selection criterias of Zuo & Weickenmeier (1995).

References

Bird, D. M. & King, Q. A. (1990). Absorbative from factors for high-energy electron diffraction. *Acta Cryst. A* **46**, 202–208.

Bird, D. M. & Saunders, M. (1992a). Inversion of convergent-beam electron diffraction patterns. *Acta Cryst. A* **48**, 555–562.

Bird, D. M. & Saunders, M. (1992b). Sensitivity and accuracy of CBED pattern matching. *Ultramicroscopy* **45**, 241–251.

Birkeland, C. R., Holmestad, R., Marthinsen, K. & Høier, R. (1997). Efficient beam-selection criteria in quantitative convergent beam electron diffraction. *Ultramicroscopy* **66**, 89–99.

Doyle, P. A. & Turner, P. S. (1968). Relativistic Hartree-Fock X-ray and electron scattering factors. *Acta Cryst. A* **24**, 390–397.

Friis, J., Jiang, B., Spence, J. C. H. & Holmestad, R. (2003a). Quantitative convergent beam electron diffraction measurements of low order structure factors in copper. *Micros. and Microanal.* **9**, 379–389. Paper 1 in this thesis.

Friis, J., Madsen, G. K. H., Larsen, F. K., Jiang, B., Marthinsen, K. & Holmestad, R. (2003b). Magnesium: Comparison of density functional theory calculations with electron and X-ray diffraction experiments. *J. Chem. Phys.* **119**. In press. Paper 4 in this thesis.

Friis, J., Marthinsen, K. & Holmestad, R. (2003c). Retrieval of anisotropic displacement parameters in Mg from convergent beam electron diffraction experiments. In *EMAG Proceedings. Inst. Phys. Conf. Ser. No. 165*. The University of Oxford, 3-5 Sep. Paper 3 in this thesis.

Gjønnes, K., Gjønnes, J., Zuo, J. M. & Spence, J. C. H. (1988). Two-beam features in electron diffraction patterns - application to refinement of low-order structure factors in GaAs. *Acta Cryst. A* **44**, 810–820.

Goodman, P. & Lehmpfuhl, G. (1967). Electron diffraction study of MgO h00-systematic interactions. *Acta Cryst. A* **22**, 14–24.

Hirsch, P. S., Howie, A., Nicholson, R. B., Pashley, D. M. & Whelan, M. (1977). Electron Microscopy of Thin Crystals. Robert E. Krieger Publ. Co. Inc, Florida.

Holmestad, R. (1994). *Quantitative Electron Diffraction*. PhD thesis, Universitetet i Trondheim-NTH.

Holmestad, R., Weickenmeier, A. L., Zuo, J. M., Spence, J. C. H. & Horita, Z. (1993). Debye-Waller factor measurements in TiAl from HOLZ line intensities. In *Inst. Phys. Conf. Ser.*, 138, 141–144.

Humphreys, C. J. (1979). The scattering of fast electrons by crystals. *Rep. Prog. Phys.* **42**, 1825–1887.

Metherell, A. J. F. (1975). Electron microscopy and materials science. In Valdré, U. & Reudl, R., editors, *Electron Microscopy in Material Science*, 397. Commission of European Communities.

Nelder, J. A. & Mead, R. (1965). A simplex method for function minimization. *Computer Journal* **7**, 308–313.

Nüchter, W., Weickenmeier, A. L. & Mayer, J. (1998). High-precision measurement of temperature factors for NiAl by convergent-beam electron diffraction. *Acta Cryst. A* **54**, 147–157.

Rez, P. (1978). *Theory of inelastic scattering in electron microscopy of thin crystals*. PhD thesis, Univ. of Oxford, England.

Saunders, M. & Bird, D. M. (1995). Measurement of low-order structure factors for silicon from zone-axis CBED patterns. *Ultramicroscopy* **60**, 311–320.

Saunders, M., Fox, A. G. & Midgley, P. A. (1999). Quantitative zone-axis convergent-beam electron diffraction (CBED) studies of metals. II. Debye-Waller-factor measurements. *Acta Cryst. A* **55**, 480–488.

Sears, V. F. & Shelley, S. A. (1991). Debye-Waller factor for elemental crystals. *Acta Cryst. A* **47**, 441–446.

Spence, J. C. H. & Zuo, J. M. (1992). Electron Microdiffraction. Plenum Press, New York.

Su, Z. & Coppens, P. (1997). Relativistic X-ray elastic scattering factors for neutral atoms z=1-54 from multiconfiguration Dirac-Fock wavefunctions in the 0-12 Å^{-1} $\sin\theta/\lambda$ range, and six-Gaussian analytical expressions in the 0-6 Å^{-1} range. *Acta Cryst. A* **53**, 749–762.

Trueblood, K. N., Bürgi, H.-B., Burzlaff, H., Dunitz, J. D., Gramaccioli, C. M., Schulz, H. H., Shmueli, U. & Abrahams, S. C. (1996). Atomic displacement parameter nomenclature - report of a subcommittee on atomic displacement parameter nomenclature. *Acta Cryst. A* **52**, 770–781.

Voss, R., Lehmpfuhl, G. & Smith, P. J. (1980). Influence of doping on the crystal potential of silicon investigated by the convergent beam electron diffraction technique. *Naturforsch. A* **35**, 973–984.

Weickenmeier, A. L. & Kohl, H. (1991). Computation of absorptive form factors for high-energy electron diffraction. *Acta Cryst. A* **47**, 590–597.

Weickenmeier, A. L. & Kohl, H. (1998). The influence of anisotropic thermal vibrations on absorbative form factors for high-energy electron diffraction. *Acta Cryst. A* **54**, 283–289.

Williams, D. B. & Carter, C. B. (1996). Transmission Electron Microscopy. Plenum Press, New York.

Zhu, S. & Zuo, J. M. (1994). *IdealMicroscope, EMLab software.*

Zuo, J. M. (1998). Quantitative convergent beam electron diffraction. *Materials Transaction, JIM* **39**, 938–946.

Zuo, J. M. (1999). Accurate structure refinement and measurement of crystal charge distribution using convergent beam electron diffraction. *Microscopy Research and Technique* **46**, 220–233.

Zuo, J. M., Kim, M., O'Keeffe, M. & Spence, J. C. H. (1999). Direct observation of d-orbital holes and Cu-Cu bonding in Cu_2O. *Nature* **401**, 49–52.

Zuo, J. M. & Spence, J. C. H. (1993). Coherent electron nanodiffraction from perfect and imperfect crystals. *Philos. Mag. A* **68**, 1055.

Zuo, J. M. & Spence, J. H. C. (1991). Automated structure factor refinement from convergent-beam patterns. *Ultramicroscopy* **35**, 185–196.

Zuo, J. M. & Weickenmeier, A. (1995). On the beam selection and convergence in the Bloch-wave method. *Ultramicroscopy* **57**, 375–383.

Chapter 3

Charge density

3.1 The independent atom model

Since only a minor part of the electrons of an atom belongs to the valence shell, the atomic electron density is well described by a spherically averaged density (except for the lightest elements H, He...). If one furthermore assumes that the radial dependence is equal to that of the theoretical ground state atom, one ends up with the *independent atom model* (IAM), in which the atoms are assumed independent of each other. It describes a *procrystal* where independent atoms are brought from infinity to the lattice positions of the crystal. From calculations of the spherical atomic charge density $\rho_{\text{atom}}(r)$ the atomic IAM X-ray scattering factors are given by

$$f^X(s) = \mathcal{F}\{\rho\} = 4\pi \int_0^\infty r^2 \rho_{\text{atom}}(r) \frac{\sin(4\pi sr)}{4\pi sr}\, dr, \tag{3.1}$$

where $\mathcal{F}$ is the Fourier transform and $s = \sin\theta/\lambda$ is the scattering angle.

In International Tables for Crystallography (1992, page 500) interpolated coefficients for the scattering factors are listed for many common elements and ions based on the relativistic Hartree-Fock calculations of Doyle & Turner (1968). More recent similar tables have been published by Su & Coppens (1997) based on multiconfiguration Dirac-Hartree-Fock calculations.

The IAM model gives very good values of f^X for large scattering angles and is a good approximation for small scattering angles too. However, by construction, it contains no information about the fine charge redistribution due to bonding. For this, one needs a model which takes the interaction between atoms into account.

3.2 Deformation density

The shape of the deformation of the electron charge distribution, when bonding features are added to the IAM model, gives a good qualitative measure of chemical bonding. This deformation is given by the deformation density, defined as

$$\Delta\rho = \rho(\mathbf{r}) - \rho^{\mathrm{IAM}}(\mathbf{r}) \tag{3.2}$$

where ρ is the true charge density and ρ^{IAM} is the procrystal density.

The deformation density includes information about atomic orientation, hybridization, charge transfer, and covalent bond formation. A peak between atoms indicates covalent bonding. However, the opposite statement, that the absence of a peak implies no covalent bonding, is not necessarily true, since for elements with more than half-filled shells, the neutral spherical atoms that are subtracted have more than one electron per orbital (Coppens, 1997). Metallic bonding is typically recognized as a spherically charge depletion at the atomic sites (Friis *et al.*, 2003a).

The deformation density is normally obtained by Fourier synthesis of experimentally measured structure factors $F_{\mathbf{g}}^{\mathrm{obs}}$ as

$$\Delta\rho = \rho^{\mathrm{obs}}(\mathbf{r}) - \rho^{\mathrm{IAM}}(\mathbf{r}) = \frac{1}{\Omega}\sum_{\mathbf{g}} \left(F_{\mathbf{g}}^{\mathrm{obs}} - F_{\mathbf{g}}^{\mathrm{IAM}}\right) \mathrm{e}^{-2\pi i \mathbf{g}\cdot\mathbf{r}}. \tag{3.3}$$

An example of a deformation density map of the (110) plane in Cu is shown in Fig. 3.1a.

The deformation density calculated in this way contains uncertainties, arising both from the errors in measured structure factors and from the fact that the number of measured structure factors is limited, which may result in non-negligible truncation errors. An approximate expression for the variance of the deformation density was derived by Rees (1976) where it is assumed that all beams up to $\mathbf{g}_{\max}$ are measured. Rees puts all uncertainties of the measured values into a factor $\sigma^2(\rho_G^{\mathrm{obs}})$ corresponding to the variance at a general position

$$\sigma^2(\Delta\rho_G) \approx \frac{1}{\Omega}\sum_{\mathbf{g}\leq\mathbf{g}_{\max}} \sigma^2(F_{\mathbf{g}}^{\mathrm{obs}}). \tag{3.4}$$

The variance of $\Delta\rho$ at position $\mathbf{r}$ is then given by

$$\sigma^2(\Delta\rho)(\mathbf{r}) = \sigma^2(\Delta\rho_G)\left[1 + \sum_{i=2}^{n} C(2\pi|\mathbf{r} - \mathcal{T}_i\mathbf{r} - \mathbf{R}_i||\mathbf{g}_{\max}|)\right] \tag{3.5}$$

where the sum runs over the n symmetry equivalent positions, $\mathcal{T}_i$ is the ith symmetry operator and $\mathbf{R}_i$ is the crystal sub-lattice translation vector which

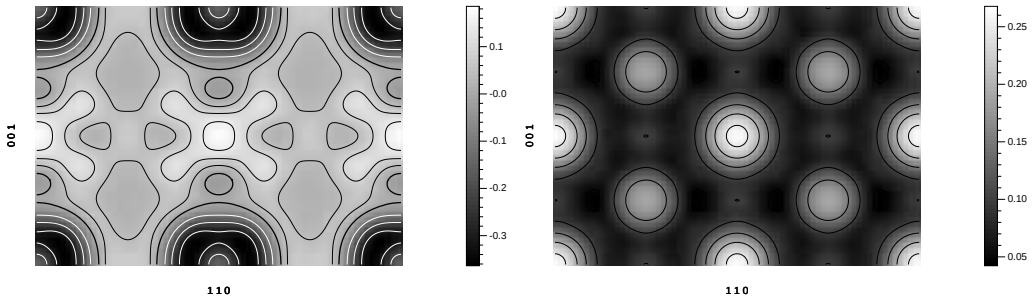

(a) (b)

Figure 3.1: (a) The deformation density of the (110) plane in Cu calculated from the 6 lowest order structure factors ($|\mathbf{g}_{\max}| = 1.58$ Å^{-1}). The zero level is marked with a thick black contour line. Positive (black) and negative (white) contour intervals are 0.05 eÅ^{-3} and 0.1 eÅ^{-3}, respectively. (b) A corresponding map of the standard deviations. Contour intervals are 0.05 eÅ^{-3}. *Source*: Friis *et al.* (2003a).

minimizes $|\mathbf{r} - \mathcal{T}_i\mathbf{r} - \mathbf{R}_i|$. The identity operator $\mathcal{T}_1 = I$ is moved out of the summation in order to simplify the discussion below, about the limit when $|\mathbf{g}_{\max}| \to \infty$. The function C is given by

PSfrag replacements

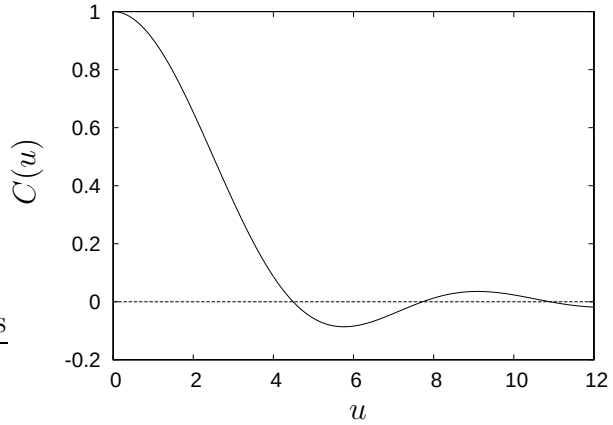

Figure 3.2: The function $C(u)$ in expression 3.6.

$$C(u) = 3(\sin(u) - u\cos(u))/u^3 \tag{3.6}$$

and is plotted in Fig. 3.2.

From Fig. 3.1b it is clear that the standard deviation of the deformation density $\sigma(\Delta\rho)$ shows large peaks close to high-symmetric positions. This is

because, when $\mathbf{r}$ is close to a high-symmetric position, $u = |\mathbf{r} - \mathcal{T}_i\mathbf{r} - \mathbf{R}_i||\mathbf{g}_{\max}|$ will be small and hence $C(u)$ will be large for all terms i in (3.5) for which $\mathcal{T}_i\mathbf{r} \approx \mathbf{r}$. From (Eq. 3.5) it follows that this is an effect caused by truncation errors. If $|\mathbf{g}_{\max}| \to \infty$ then $C(u) \to 0$ and the variance $\sigma^2(\Delta\rho)(\mathbf{r})$ will be flat and reduced to the variance of a general position $\sigma^2(\Delta\rho_G)$.

These truncation errors can be avoided in deformation densities derived from a multipole model or a maximum entropy simulation. In the former case, one fits a set of multipolar parameters to create a model reproducing the observed structure factors $F_{\mathbf{g}}^{\text{obs}}$. From this model it is possible to directly find ρ^{obs}, without any Fourier summation. In the latter case the Fourier summation is also avoided, since one is already working in real space.

3.3 Density functional theory

Density functional theory (DFT) has shown to be an efficient and accurate approach for solving the many-electron system of a crystal. It is based on the statement that there exists a one-to-one correspondence between the ground state density $\rho(\mathbf{r})$ of a many-electron system and the external potential V (Hohenberg & Kohn, 1964). From this statement it follows that the energy can be written as a functional of the electron density. In the formalism of Kohn & Sham (1965) the total energy is given by

$$E[\rho] = E_{\text{kin}}^{\text{KS}}[\rho] + E_{\text{eN}}[\rho] + E_{\text{ee}}[\rho] + E_{\text{xc}}[\rho] + E_{\text{NN}} \tag{3.7}$$

where the terms are, respectively, the kinetic energy[1], the attractive Coulomb electron-nucleus interaction, the repulsive Coulomb electron-electron interaction, the exchange-correlation energy and finally the nucleus-nucleus Coulomb repulsion, which does not depend on the electron density. The exchange-correlation term does not have a simple classical interpretation. It incorporates the effect of the Pauli principle, i.e. that the wave-function is anti-symmetric under the exchange of two electrons, and the Coulomb correlation between electrons, thus the name.

The energy of a system of electrons in an external field is given by minimizing the density functional[2] in Eq. (3.7). This is equivalent to solving a

[1] $E_{\text{kin}}^{\text{KS}}$ is the energy of a fictitious non-interaction system. A correction $(E_{\text{kin}} - E_{\text{kin}}^{\text{KS}})$ is built into the exchange correlation $E_{\text{xc}}[\rho]$ (Friedrich, 1999).

[2] This follows from the variational principle, which states that given a normalized wave function Φ, which satisfies appropriate boundary conditions, the expectation value of the Hamiltonian is an upper limit to the exact ground state energy $\langle\Phi|\mathcal{H}|\Phi\rangle \geq \mathcal{E}_0$.

set of Kohn-Sham equations, comprising a one-particle Schrödinger equation

$$\left[-\frac{\hbar^2}{2m}\nabla^2 + V^{KS}[\mathbf{r},\rho(\mathbf{r})]\right]\phi_i(\mathbf{r}) = \varepsilon_i\phi_i(\mathbf{r}) \tag{3.8}$$

with

$$V^{KS}[\mathbf{r},\rho(\mathbf{r})] = V_{\text{ext}}(\mathbf{r}) + V_{\text{ee}}(\mathbf{r}) + \frac{\partial}{\partial\rho(\mathbf{r})}E_{\text{xc}}[\rho(\mathbf{r})], \tag{3.9}$$

where the Kohn-Sham orbitals $\phi_i(\mathbf{r})$ are related to the electron density by

$$\rho(\mathbf{r}) = \sum_i f_i|\phi_i(\mathbf{r})|^2 \tag{3.10}$$

with orbital occupation numbers f_i. The terms in the Kohn-Sham potential (3.9) are, respectively, the external potential[3], the Coulomb potential corresponding to $\rho(\mathbf{r})$ (also known as the Hartree potential) and the functional derivative of the exchange-correlation with respect to the density, representing the many-body effects of the system. The Kohn-Sham equations (3.8) and (3.9) may be solved iteratively. Beginning with an initial potential, Eq. (3.8) is solved and the electron density is obtained from the orbitals via Eq. (3.10). Then this density is used to form a new potential for Eq. (3.8). This self-consistency cycle is continued until the potential and density satisfy some convergence criteria, which often involve many iterations, since the self-consistency procedure is inherently unstable. Sophisticated 'feedback' or 'mixing' techniques are necessary to prevent oscillations.

In order to solve the Kohn-Sham equations, one needs an approximation for the exchange-correlation term, which in general depends on $\rho(\mathbf{r})$ in every point $\mathbf{r}$. The traditional approximation, proposed by Kohn & Sham (1965), is referred to as the *local density approximation* (LDA) and takes the form

$$E_{\text{xc}} = \int\varepsilon_{\text{xc}}[\rho(\mathbf{r})]\rho(\mathbf{r})\,d\mathbf{r} \tag{3.11}$$

where ε_{xc} is the exchange correlation energy of a homogeneous electron gas with the density $\rho(\mathbf{r}) = \rho$. Although this form of the exchange correlation energy appears to be valid only when the electron density is slowly varying, it is a good approximation for a wide range of systems. A common extension of the LDA approximation is to include a dependence of $\nabla\rho(\mathbf{r})$. This is the *generalized gradient approximation* (GGA), which in general performs slightly better than LDA in estimating non-local properties, such as lattice parameters and bulk modulus. A popular variant of GGA is the parametrization of Perdew *et al.* (1996).

[3]The nucleus potential is normally called V_{ext}, since the electrons "see" the nucleus potential just like any other external potential.

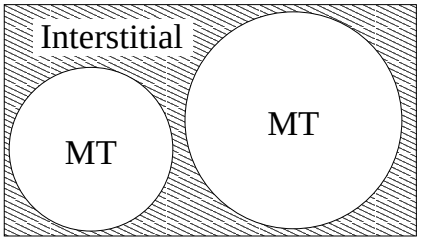

Figure 3.3: Partitioning of the unit cell into atomic-centered "Muffin-Tin" (MT) spheres and an interstitial region in the LAPW method.

When solving the Kohn-Sham equations, another important issue is to choose an appropriate basis set to represent the single particle wave-functions $\phi_i(\mathbf{r})$. All calculations in this thesis have been carried out with WIEN2k (Blaha *et al.*, 2001), which uses the *linearized augmented plane wave* (LAPW) or *augmented plane wave plus local orbital* (AWP+lo) basis sets, that are among the most accurate methods for performing electronic structure calculations for crystals. Here the unit cell is divided into non-overlapping atomic centered, so called "Muffin-Tin" spheres and an interstitial region (Fig. 3.3). Inside the spheres, the wave-function is represented by spherical harmonics and radial functions. Outside it is represented by plane waves, with the requirement that the wave-function and its first derivative have to be continuous on the sphere boundaries.

Although DFT is a very successful tool for studying properties of materials, and normally reproducing experimental results with errors less than a few percent, notable problems still exist. One of them is the unphysical self-interaction of an electron with itself, addressed in Friis *et al.* (2003b). The E_{ee} term of Eq. 3.7 contains the mean-field interaction energy of an electron with itself. This contribution would exactly have been canceled if the exchange-correlation functional is exact. However, for systems where the electrons are localized, or close to localized, the approximations in the exchange-correlation functional result in a non-negligible self interaction. Several corrections for this have been proposed (Perdew & Zunger, 1981; Lundin & Eriksson, 2001), but they are not yet a standard option in the WIEN2k program. Some modifications of the code was therefore necessary for Paper 4.

References

Blaha, P., Schwarz, K., Madsen, G., Kvasnicka, D. & Luitz, J. (2001). *WIEN2k, An Augmented Plane Wave Plus Local Orbitals Program for Calculating Crystal Properties.* Vienna University of Technology, Austria.

Coppens, P. (1997). X-Ray Charge Densities and Chemical Bonding. Oxford University Press.

Doyle, P. A. & Turner, P. S. (1968). Relativistic Hartree-Fock X-ray and electron scattering factors. *Acta Cryst. A* **24**, 390–397.

Friedrich, C. (1999). Introduction to density functional theory (and related stuff). Presentation, Fritz Haber-Institut der Max-Planck-Gesellschaft, Berlin, Abteilung Theorie. Available at: `http://www.physik.fu-berlin.de/~asmis/sfb546/C6friedrich.pdf`.

Friis, J., Jiang, B., Marthinsen, K. & Holmestad, R. (2003a). A study of charge density in copper. In production. Paper 5 in this thesis.

Friis, J., Madsen, G. K. H., Larsen, F. K., Jiang, B., Marthinsen, K. & Holmestad, R. (2003b). Magnesium: Comparison of density functional theory calculations with electron and X-ray diffraction experiments. *J. Chem. Phys.* **119**. In press. Paper 4 in this thesis.

Hohenberg, P. & Kohn, W. (1964). Inhomogeneous electron gas. *Phys. Rev. B* **136**, 864.

International Tables for Crystallography (1992). volume C. Dordrecht: International Union of Crystallography, Kluwer.

Kohn, W. & Sham, L. J. (1965). Self-consistent equations including exchange and correlation effects. *Phys. Rev.* **140**, A1133–A1138.

Lundin, U. & Eriksson, O. (2001). A novel method of self-interaction corrections in density functional calculations. *Int. J. Quantum Chem* **81**, 247–252.

Perdew, J. P., Burke, K. & Ernzerhof, M. (1996). Generalized gradient approximation made simple. *Phys. Rev. Lett.* **77**, 3865–3868.

Perdew, J. P. & Zunger, A. (1981). Self-interaction correction to density-functional approximations for many-electron systems. *Phys. Rev. B* **23**, 5048–5079.

Rees, B. (1976). Variance and covariance in experimental electron density studies, and the use of chemical equivalence. *Acta Cryst. A* **32**, 483–488.

Su, Z. & Coppens, P. (1997). Relativistic X-ray elastic scattering factors for neutral atoms z=1-54 from multiconfiguration Dirac-Fock wavefunctions in the 0-12 Å^{-1} $\sin\theta/\lambda$ range, and six-Gaussian analytical expressions in the 0-6 Å^{-1} range. *Acta Cryst. A* **53**, 749–762.

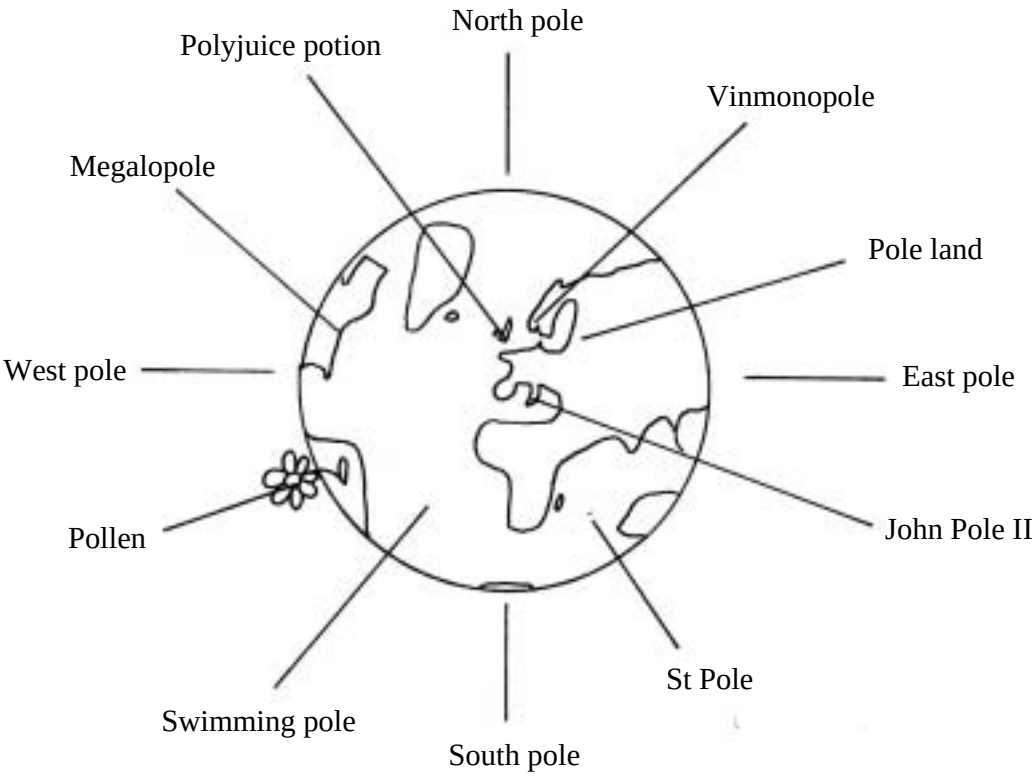

Chapter 4

Multipole formalism

When studying chemical bonding, it is necessary to account for the perturbation of the spherically IAM electron density caused by interaction with other atoms. In the multipole formalism by Hansen & Coppens (1978) the aspherical corrections to IAM density are described by a set of atom-centered multipolar functions, obeying the symmetry of the atomic site. The multipolar functions are strongly related to the well known spherical harmonics forming the solution of the hydrogen atom. It is possible to show, for an isolated atom, that the multipole formalism is equivalent to a single-Slater determinant atomic wave function description composed of orthogonal spin-orbitals (Koritsanszky *et al.*, 2003, sec. 1.8). In a multipole model, based on a set of measured structure factors, the population and expansion parameters for each included multipolar function are fitted in order to reproduce the observed structure factors.

In this chapter we will only give a brief resume of the multipole method and focus on the multipole refinement of electron diffraction data. The details and further development of the model are well described in Coppens (1997) and Coppens (2001).

4.1 The multipole model

In the multipole formalism of Hansen & Coppens (1978), the atomic electron density

$$\begin{aligned}\rho_{\text{atom}}(\mathbf{r}) &= P_c\rho_{\text{core}}(r) + P_v\kappa^3\rho_{\text{valence}}(\kappa r) \\ &\quad + \sum_{l=0}^{l_{\max}} \kappa_l'^3 R_l(\kappa_l' r) \sum_{m=0}^{l} \sum_{p=\pm} P_{lmp}\, d_{lmp}(\theta,\phi). \qquad (4.1)\end{aligned}$$

is described by three parts; a spherically core part populated with P_c electrons, a spherical valence part which is allowed to expand ($\kappa < 1$) or contract ($\kappa > 1$) with population P_v, and a series of multipolar functions accounting for an aspherically redistribution of the electron density, each populated with P_{lmp} electrons.

The multipolar functions are characterized by a radial function $R_l(\kappa' r)$ (which also may be expanded or contracted with the κ-parameter) and the density functions $d_{lm\pm}$, that are real spherical harmonics, normalized such that

$$\int |d_{lm\pm}| \, \sin\theta \, d\theta \, d\phi = \begin{cases} 1 & \text{for} \quad l = 0 \\ 2 & \text{for} \quad l > 0 \end{cases} . \tag{4.2}$$

This normalization implies that a multipole population $P_{lm\pm} = 1$ corresponds to one electron for the spherically symmetric d_{00}, and that both the positive and negative lobes of $d_{lm\pm}$ for $l > 0$ integrate to one electron each. The shape of the density functions for $l \leq 3$ are illustrated in Fig. 4.1.

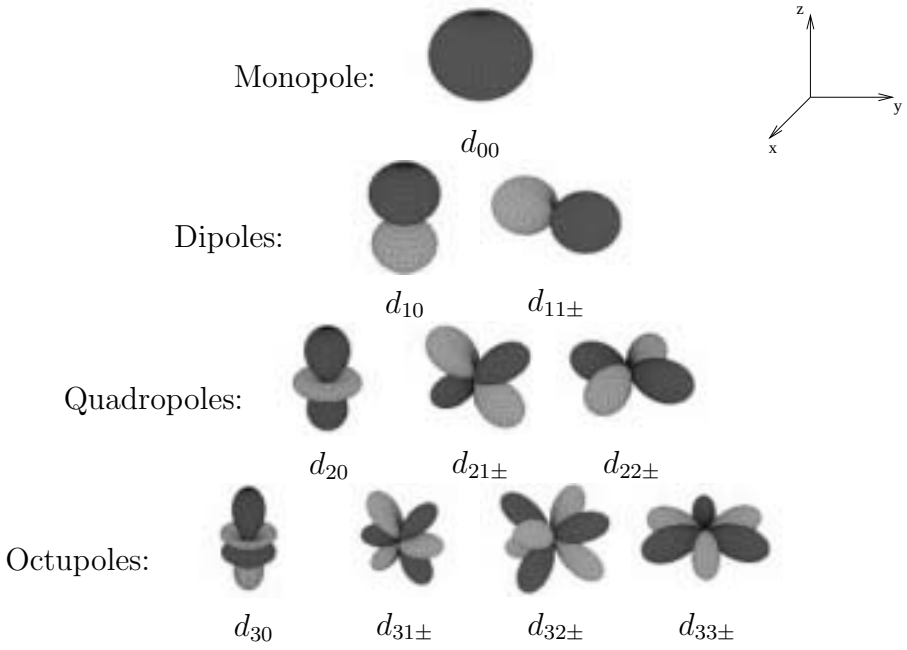

Figure 4.1: Multipolar functions. The difference between the d_{lm+} and d_{lm-} functions is that they are rotated 90° around the z-axis compared to each other. *Source*: `http://odin.math.nau.edu~jws/dpgraph/Yellm.html`.

Since the multipolar functions form the solution of the hydrogen atom, and approximate heavier atoms very well, the series in Eq. 4.1 converges very quickly. For second and third row elements, it is usually sufficient to include up to quadropoles (l=2), but for $3d$ transition metals hexadecapoles (l=4)

also have to be included (Stewart *et al.*, 2000). Occasionally, higher order multipoles might be necessary to include, which e.g. was the case in the old study of beryllium (Stewart, 1977), and might, for the same reasons, also be necessary in a future study of magnesium. The number of independent multipole functions is strongly reduced by the site symmetry of the atom. These symmetry-constrains are easily obtained by the *index picking rules* of Kurki-Suonio (1977). For instance, for the cubic site symmetry of the Cu atoms in pure fcc copper, all terms in the multipole expansion up to $l = 4$ vanish, except for the monopole and a linear combination of hexadecapoles (known as *cubic harmonics*, von der Lage & Bethe, 1947). In other words, the multipole model is a very flexible model for the electron distribution which incorporates the required symmetry, but at the same time only requires a limited set of parameters to be fitted to the experimental data.

The choice of the radial functions $R_l(r)$ is the most difficult part in multipole modeling. Even for the spherical parts, it is not obvious which electrons should be included in the core, valence, or monopole terms. Often the core and valence densities are calculated from Roothaan-Hartree-Fock atomic wave functions and expanded in terms of Slater-type basis functions

$$O_l(r) = \sqrt{\frac{(2\zeta_l)^{2n_l+1}}{2n_l!}} r^{n_l-1}\, \mathrm{e}^{-\zeta_l r}, \tag{4.3}$$

for which the expansion coefficients and the parameters n_l and ζ_l are tabulated by Clementi & Roetti (1974).

The radial dependence of the multipolar functions $R_l(r)$ is given by products of atomic orbitals of the form $O_{l'}O_{l''}$. Table 4.1 shows which multipoles can be constructed from the different orbital products. In the case of e.g. copper, which for $l \leq 4$ only has a hexadecapole, we see that the radial function must be constructed by the $3d \times 3d$ orbital product. It is often sufficient to describe the multipolar radial function by only one term $O_{l'}O_{l''}$, so called single zeta-functions.

Table 4.1: l values for the allowed multipoles formed by the orbital product $O_{l'}O_{l''}$, where $l', l'' = 0, 1, 2$ for s p and d orbitals, respectively (Koritsanszky *et al.*, 2003).

$l' \backslash l''$	s	p	d
s	0	1	2
p		0 2	1 3
d			0 2 4

4.2 Aspherical contribution to atomic scattering

From the Fourier transform of Eq. (4.1) aspherically atomic scattering factors are obtained as

$$f(\mathbf{s}) = P_c f_{\text{core}}(s) + P_v f_{\text{valence}}(s/\kappa) + \sum_{l=0}^{l_{\max}} \sum_{m=0}^{l} \sum_{p} P_{lmp} f_{lmp}(\mathbf{s}/\kappa'), \qquad (4.4)$$

where the deformation scattering factors $f_{lmp}(\mathbf{s})$ are given by

$$f_{lmp}(\mathbf{s}) = 4\pi i^l \langle j_l \rangle \, d_{lmp}(\beta, \gamma). \qquad (4.5)$$

The relation between the reciprocal angular coordinates β and γ and the real space angular coordinates θ and ϕ is shown in Fig. 4.2. $\langle j_l \rangle$ is the Fourier-Bessel transform of the radial function $R_l(r)$, defined as

PSfrag replacements

$$\langle j_l \rangle = \int_0^\infty j_l(2\pi sr) R_l(r) r^2 \, dr \qquad (4.6)$$

with j_l being the lth order Bessel function.

PSfrag replacements

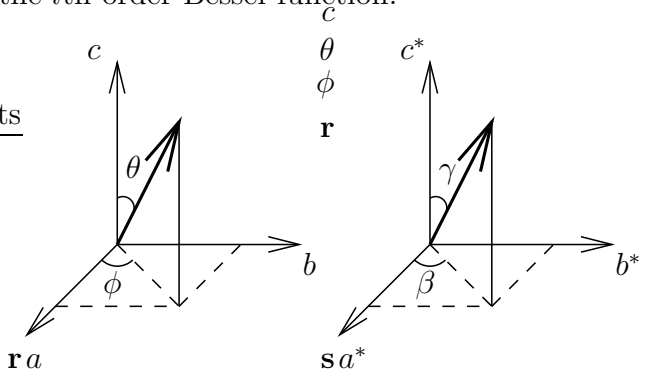

Figure 4.2: The angles θ, ϕ, β and γ.

4.3 Multipole refinement of electron diffraction data

In multipole refinement, the population and κ-parameters are determined from least square fitting between structure factors calculated from the multipole model $F_{\mathbf{g}}^{\text{calc}}$ and the observed structure factors $F_{\mathbf{g}}^{\text{obs}}$. The model structure factors are obtained from Eq. (4.4) as

$$F_{\mathbf{g}}^{\text{calc}} = \sum_j f_j(\mathbf{s}) T_j(\mathbf{s}) \, \mathrm{e}^{-2\pi \mathbf{g}\cdot\mathbf{r}_j}. \qquad (4.7)$$

where $T_j(\mathbf{s})$ is the temperature factor of atom j. For electron diffraction, one normally converts the observed structure factors to their corresponding static lattice values, at which the temperature factors $T_j(\mathbf{s})$ are set to one. The reason is that the temperature factors have to be determined anyway, in order to convert the measured electron structure factors $U_{\mathbf{g}}^{\text{obs}}$ into X-ray structure factors $F_{\mathbf{g}}^{\text{obs}}$ (see appendix A), since all well-tested multipole refinement programs (such as XD, VALRAY, MOLLY, etc...) are made for X-ray data and do not accept $U_{\mathbf{g}}^{\text{obs}}$ as input. Another reason is that one wants to refine as few parameters as possible. In the X-ray community a rule of thumb is a redundancy of about ten observed structure factors for each refined parameter. Such an overdetermination is not necessary with electron diffraction data, since the low order structure factors, containing almost all bonding information, are measured very accurately. In addition, the low order data is not very sensitive to the isotropic or anisotropic temperature parameters. However, in order to obtain reliable results, the electron diffraction data set is usually not large enough. As mentioned, the solution is to combine with X-ray (or γ-ray) measurements. In these cases one may as well convert the electron diffraction data to the temperature of the X-ray measurements.

The multipole refinement programs mentioned above offer a lot of corrections specific to X-ray or neutron diffraction data (such as scaling, extinction and absorption correction, etc...) that safely can be turned off, but that may be useful in the case electron diffraction data are combined with some high order X-ray structure factors. VALRAY was used for the multipole refinements in Paper 6.

References

Clementi, E. & Roetti, C. (1974). Roothaan-Hartree-Fock atomic wavefunctions. *Atomic Data and Nuclear Data Tables* **14**, 177–478.

Coppens, P. (1997). X-Ray Charge Densities and Chemical Bonding. Oxford University Press.

Coppens, P. (2001). Chemical applications of X-ray charge-density analysis. *Chem. Rev.* **101**, 1583–1627.

Hansen, N. K. & Coppens, P. (1978). Testing aspherical atom refinements om small-molecule data sets. *Acta Cryst. A* **34**, 909–921.

Koritsanszky, T., Mallinson, P. R., Howard, S., Volkov, A., Macchi, P., Su, Z., Gatti, C., Richter, T., Farrugia, L. J. & Hansen, N. K. (2003). *A Com-*

puter Program Package for Multipole Refinement and Analysis of Electron Densities from Diffraction Data.

Kurki-Suonio, K. (1977). Symmetry and its implications. *Isr. J. Chem.* **16**, 115–123.

Stewart, R. F. (1977). A charge-density study of crystalline beryllium. *Acta Cryst. A* **33**, 33–38.

Stewart, R. F., Spackman, M. A. & Flensburg, C. (2000). *VALRAY User's Manual*. Carnegie-Mellon University and University of Copenhagen.

von der Lage, F. C. & Bethe, H. A. (1947). A method for obtaining electronic eigenfunctions and eigenvalues in solids with application to sodium. *Phys. Rev.* **71**, 612–622.

Chapter 5

Maximum entropy

> You should call it 'entropy' and for two reasons: first, the function is already in use in thermodynamics under that name; second, and more importantly, most people don't know what entropy is, and if you use the word 'entropy' you will win every time!
>
> von Neumann

5.1 A short introduction to the maximum entropy method

The maximum entropy method (MEM) is based on information theory and was first developed for radioastronomy to enhance the information from incomplete and noisy data (Frieden, 1972; Gull & Daniell, 1978). MEM was first introduced into crystallography by Collins (1982) and has been very successful in order to optimize the information that can be extracted from an incomplete and noisy experimental data set and to produce the least possible biased density. An excellent review of modern applications of MEM in crystallography is given by Gilmore (1996).

The formalism is very similar to that of statistical thermodynamics. Both the statistical entropy and the information entropy deal with the most probable distribution. In thermodynamics, this is the distribution of particles, while in information theory it is the distribution of numerical quantities over the ensemble of pixels. Statistical arguments, taken from thermodynamics, can therefore be used to derive an expression for the entropy function to be maximized.

The probability for a distribution of N particles over m boxes, each with

the prior probability q_i to contain n_i particles, is given by

$$P = \frac{N!}{n_1!\, n_2!\, \ldots n_m!}\, q_1^{n_1} q_2^{n_2} \ldots q_m^{n_m}. \tag{5.1}$$

The entropy S is defined as $\ln P$. So, by using Stirling's formula ($\ln n \approx n \ln n - n$) the entropy, apart from a constant (only depending on $N = \sum_i n_i$), becomes

$$S = -\sum_{i=1}^{m} n_i \ln \frac{n_i}{q_i}. \tag{5.2}$$

If we digitize the unit cell (or an appropriate subunit) of volume V into M pixels, each with volume V/M and density $\rho(\mathbf{r}_j)$, the entropy of the electron distribution can, in accordance with Eq. (5.2), be written as

$$S[\rho(\mathbf{r})] = -\sum_{j=1}^{M} p_j \ln \frac{p_j}{m_j}, \tag{5.3}$$

where S now becomes a functional of the sought charge density $\rho(\mathbf{r})$. The quantities $p_j = p(\mathbf{r}_j)$, the probability of the density associated with pixel j, and $m_j = m(\mathbf{r}_j)$, the corresponding probability for the prior (model) density $\rho_0(\mathbf{r})$ at pixel j, are defined as

$$p_j = p(\mathbf{r}_j) = \rho(\mathbf{r}_j) \Big/ \sum_{i=1}^{M} \rho(\mathbf{r}_i) \tag{5.4}$$

$$m_j = m(\mathbf{r}_j) = \rho_0(\mathbf{r}_j) \Big/ \sum_{i=1}^{M} \rho_0(\mathbf{r}_i)\ . \tag{5.5}$$

We want to maximize the entropy functional $S[\rho(\mathbf{r})]$, given our knowledge of the prior density, the values $F_{\mathbf{h}}^{\text{obs}}$ and the standard deviation $\sigma_{\mathbf{h}}$ of the N measured structure factors. The observed structure factors are taken into account by introducing the constraint

$$C[\rho(\mathbf{r})] = \chi^2 = \frac{1}{N} \sum_{\mathbf{h}} \left| F_{\mathbf{h}}^{\text{obs}} - F_{\mathbf{h}}^{\text{calc}} \right|^2 / \sigma_{\mathbf{h}}^2 \lesssim 1, \tag{5.6}$$

where

$$F_{\mathbf{h}}^{\text{calc}} = \frac{V}{M} \sum_{j=1}^{M} \rho(\mathbf{r}_j)\, \mathrm{e}^{-2\pi i \mathbf{h}\cdot\mathbf{r}_j} \tag{5.7}$$

are structure factors calculated from the sought charge density. Note that Eq. (5.7) remains valid even when only a subunit of the unit cell is digitized into

M pixels, provided that this subunit remains a multiple of the asymmetric unit.

If the constraint (5.6) were not introduced, maximizing the entropy would result in a uniform distribution. To enforce the constraint, the maximization of $S = S[\rho(\mathbf{r})]$ is performed by introducing the Lagrangian function $L = S - \lambda\chi^2$, where λ is the Lagrange multiplier (Skilling & Bryan, 1984). At convergence $\nabla_\rho L = 0$ or, equivalently, $\nabla_\rho S = \lambda \nabla_\rho \chi^2$. For each pixel j, this corresponds to

$$\frac{\partial S}{\partial \rho_j} = \lambda \frac{\partial \chi^2}{\partial \rho_j}, \tag{5.8}$$

where $\rho_j = \rho(\mathbf{r}_j)$. Note that we here use the same Lagrangian multiplier λ for all observed structure factors, as is common in crystallographic applications (Collins, 1982; Gull & Skilling, 1991; Kumazawa, 1993; Burger, 1998; Tanaka *et al.*, 2002).

Equation (5.8) is non-linear, and has to be solved iteratively for both $\lambda(n+1)$ and $\rho_j(n+1)$ coming from $\lambda(n)$ and $\rho_j(n)$. The starting values are $\lambda(0) \gtrsim 0$ and the prior density $\rho_j(0) = \rho_0(\mathbf{r}_j)$. To achieve convergence, the $\chi^2 \lesssim 1$ constraint must first be satisfied, and thereafter the entropy S is maximized while keeping $\chi^2 \lesssim 1$.

Using Eq. (5.3), the left-hand side of Eq. (5.8) can be written as

$$\begin{aligned}
\frac{\partial S}{\partial \rho_j} &= -\sum_{j=1}^{M} \frac{\partial p_j}{\partial \rho_j} \left(\ln \frac{p_j}{m_j} + 1 \right) \\
&= -\sum_{j=1}^{M} \frac{\delta_{jk} - \rho_j}{\rho} \left(\ln \frac{p_j}{m_j} + 1 \right) \\
&= -\frac{1}{\rho} \left(\ln \frac{p_k}{m_k} - \sum_{j=1}^{M} p_j \ln \frac{p_j}{m_j} \right) \\
&= -\frac{1}{\rho} \ln \frac{\rho_k / \rho_{0k}}{B},
\end{aligned} \tag{5.9}$$

where $\rho = \sum_j \rho_j$ is the total number of electrons in the unit cell and $B = \exp(\sum_j p_j \ln \rho_j / \rho_{0j})$. Note that B is very close to unity when the prior density is very close to the true density. In the case of an uniform prior density, $\rho_0(\mathbf{r}_j) = \rho_{0j} = \rho/M$, B is reduced to $B = AM/\rho$, where $A = \exp(\sum_j p_j \ln \rho_j)$ is the weighted logarithmic average of the converged entropic density $\rho(\mathbf{r})$ over the unit cell. A corresponds to the expected density far away from any atom. Reconstructed density values smaller than A are considered unreliable.

Substitution of Eq. (5.9) into (5.8) leads to

$$\rho_j/\rho_{0j} = B\,\mathrm{e}^{-\lambda\rho\left(\partial\chi^2/\partial\rho_j\right)}. \tag{5.10}$$

From this we can set up the iteration formulas

$$\begin{aligned}\lambda(n+1) &= \left(\ln\rho_k(n)/\rho_{0k} - \sum_{j=1}^{M}\rho_j(n)/\rho_{0j}\right) \\ &\quad\times\left(F_0\sum_{\mathbf{h}}2\frac{|F_{\mathbf{h}}^{\mathrm{obs}}-F_{\mathbf{h}}^{\mathrm{calc}}(n)|}{\sigma_{\mathbf{h}}^2}\,\mathrm{e}^{-2\pi i\mathbf{h}\cdot\mathbf{r}_j}\right)^{-1}\end{aligned} \tag{5.11}$$

and

$$\begin{aligned}\rho_j(n+1) &= \rho_{0j}\exp\left(\sum_{j=1}^{M}p_j(n)\ln\rho_k(n)/\rho_{k0}\right. \\ &\quad\left.+\,\lambda(n+1)F_0\sum_{\mathbf{h}}2\frac{|F_{\mathbf{h}}^{\mathrm{obs}}-F_{\mathbf{h}}^{\mathrm{calc}}(n)|}{\sigma_{\mathbf{h}}^2}\,\mathrm{e}^{-2\pi i\mathbf{h}\cdot\mathbf{r}_j}\right),\end{aligned} \tag{5.12}$$

where $F_{\mathbf{h}}^{\mathrm{calc}}(n) = V/M\sum_{\mathbf{h}}\rho_j(n)\exp(-2\pi i\mathbf{h}\cdot\mathbf{r}_j)$ and $F_0 = V/M\,\rho$.

5.2 Weaknesses of MEM

For the old, but accurate, Pendellösung data of silicon by Saka & Kato (1968), it was found that the distribution of the discrepancies between $F_{\mathbf{h}}^{\mathrm{obs}}$ and $F_{\mathbf{h}}^{\mathrm{calc}}$ after the MEM analysis (Sakata & Sato, 1990) deviates from the ideal Gaussian distribution (Jauch & Palmer, 1993; Jauch, 1994). This points to a weakness in the constraint (5.6): It constrains the variance of the distribution, but not its shape. An improvement has been reported (De Vries *et al.*, 1994) by assigning a weighting factor proportional to $|\mathbf{h}|^{-4}$ to the summation of Eq. (5.7).

Another related weakness is that MEM tends to sharpen strong features but flatten weak features, when the dynamic range is large. This may be a problem when the aim is to recover the fine details of the density (which is often the case in bonding studies) (Papoular *et al.*, 1996; Iversen *et al.*, 1997). In the next section we will describe how the dynamic range can be greatly reduced by applying MEM to the deformation density instead of the full density.

5.3 Two-channel MEM

Since the probabilities $p(\mathbf{r})$ and $m(\mathbf{r})$ have to be positive, a positive charge density $\rho(\mathbf{r})$ is required over the whole unit cell. This is not the case for the deformation density $\Delta\rho(\mathbf{r}) = \rho^{\rm obs}(\mathbf{r}) - \rho^{\rm IAM}(\mathbf{r})$, which takes both positive and negative values. The average of $\Delta\rho(\mathbf{r})$ over the unit cell must be zero, since bonding effects only redistribute the electron density. In the *two-channel method*, the deformation density is written as $\Delta\rho(\mathbf{r}) = \rho^+(\mathbf{r}) - \rho^-(\mathbf{r})$, where the two functions $\rho^+(\mathbf{r})$ and $\rho^-(\mathbf{r})$ are positive and represent the densities of excess and lack of electrons, respectively. This method was first developed for magnetization densities (Papoular & Gillon, 1990) and for neutron scattering (Sakata *et al.*, 1993) for which both positive and negative scattering densities occur.

In each pixel j, the functions $\rho_j^+ = \rho^+(\mathbf{r}_j)$ and $\rho_j^- = \rho^-(\mathbf{r}_j)$ are mutually exclusive, and have the corresponding probabilities $p_j^+ = \rho_j^+/Q$ and $p_j^- = \rho_j^-/Q$, where $Q = \sum_j(\rho_j^+ + \rho_j^-)$. The prior deformation density $\Delta\rho_{0j}$, at pixel j, is in a similar way divided into two positive functions ρ_{0j}^+ and ρ_{0j}^- with the corresponding probabilities m_j^+ and m_j^-. In analogy to Eq. (5.3), the two-channel entropy is defined as

$$S[\Delta\rho] = -\sum_{j=1}^{M}\left(p_j^+\frac{p_j^+}{m_j^+} + p_j^-\frac{p_j^-}{m_j^-}\right). \tag{5.13}$$

Since $\partial\chi^2/\partial\rho_j^+ = -\partial\chi^2/\partial\rho_j^-$, the positive and negative scattering densities are related by

$$\rho_j^+\rho_j^- = B^2\rho_j^+\rho_j^-. \tag{5.14}$$

Inserting the entropy (5.13) into Eq. (5.8) leads, with the help of Eq. (5.14), to the following iteration formulas

$$\lambda(n+1) \;=\; -\frac{1}{Q}\frac{\ln\rho_{0j}^+ + \ln\rho_{0j}^-}{C_j'^+(n) + C_j'^-(n)} \tag{5.15}$$

$$\rho_j^\pm(n+1) \;=\; \rho_{0j}^\pm B(n)\,\mathrm{e}^{-\lambda(n+1)\,Q\,C'^\pm(n)}, \tag{5.16}$$

where

$$B(n) = \exp\left[\sum_{j=1}^{M}\left(p_j^+(n)\ln\frac{\rho_j^+(n)}{\rho_{0j}^+} + p_j^-(n)\ln\frac{\rho_j^-(n)}{\rho_{0j}^-}\right)\right] \tag{5.17}$$

and

$$C_j'^\pm(n) = \frac{\partial\chi^2}{\partial\rho_j^\pm}(n) = \mp\frac{V}{M}\sum_{\mathbf{h}} 2\frac{|\Delta F_{\mathbf{h}}^{\rm obs} - \Delta F_{\mathbf{h}}^{\rm calc}(n)|}{\sigma_{\mathbf{h}}^2}\,\mathrm{e}^{-2\pi i\mathbf{h}\cdot\mathbf{r}_j}. \tag{5.18}$$

A problem with applying the two-channel MEM to the deformation density $\Delta\rho(\mathbf{r})$, is that the quantity Q, the sum of positive and negative densities over the unit cell, is unknown (Nishibori, 2003). However, by introducing a rescaled Lagrangian multiplier $\mu = \lambda Q$, Eqs. (5.15) and (5.16) become

$$\mu(n+1) = -\frac{\ln \rho_{0j}^{+} + \ln \rho_{0j}^{-}}{C_j'^{+}(n) + C_j'^{-}(n)} \tag{5.19}$$

$$\rho_j^{\pm}(n+1) = \rho_{0j}^{\pm} B(n)\, \mathrm{e}^{-\mu(n+1)\, C'^{\pm}(n)}, \tag{5.20}$$

which are independent of Q. One can therefore use an ordinary two-channel MEM algorithm designed for neutron diffraction (e.q. the MEND algorithm by Burger (1998)) on deformation densities (Friis *et al.*, 2003).

5.4 Applications of MEM to QCBED

MEM is the method of choice when one wants to extract useful information from poor or limited experimental data. Since the data from QCBED is of outstanding quality, one would normally prefer to use other methods, e.g. multipole analysis, for charge studies. However, the QCBED data set often needs to be extended with structure factors of less quality. This may result in an inconsistent data set, especially if rescaling or other corrections are applied to the foreign data set (Friis *et al.*, 2003).

In these cases, MEM may be an alternative method to obtain a least biased charge density from all the observed data. As pointed out in section 5.2 it seems however to be important to use the two-channel method in order to reduce the dynamical range and avoid sharpening of strong and flattening of weak features.

References

Burger, K. (1998). *Enchanced Versions of the Maximum Entropy Program MEED for X-ray and Neutron Diffraction.* Inst. für Kristallographie, Universität Tübingen.

Collins, D. M. (1982). Electron density images from imperfect data by iterative entropy maximization. *Nature* **298**, 49–51.

De Vries, R. Y., Briels, W. J. & Feil, D. (1994). Novel treatment of the experimental data in the application of the maximum-entropy method to the

determination of the electron-density distribution from x-ray experiments. *Acta Cryst. A* **50**, 383–391.

Frieden, B. R. (1972). Restoring with maximum likelihood and maximum entropy. *J. Opt. Soc. Am.* **62**, 511–518.

Friis, J., Jiang, B., Marthinsen, K. & Holmestad, R. (2003). A study of charge density in copper. In production. Paper 5 in this thesis.

Gilmore, C. (1996). Maximum entropy and Bayesian statistics in crystallography: a review of practical applications. *Acta Cryst. A* **52**, 561–589.

Gull, S. F. & Daniell, G. J. (1978). Image reconstruction from incomplete and noisy data. *Nature* **272**, 686–690.

Gull, S. F. & Skilling, J. (1991). *MemSys5 User's Manual*. MEDC Ltd, 33 North End, Meldreth, Royston SG8 6NR, England.

Iversen, B. B., Jensen, J. L. & Danielsen, J. (1997). Errors in maximum-entropy charge-density distributions obtained from diffraction data. *Acta Cryst. A* **53**, 376–387.

Jauch, W. (1994). The maximum-entropy method in charge-density studies. ii. general aspects of reliability. *Acta Cryst. A* **50**, 650–652.

Jauch, W. & Palmer, A. (1993). The maximum-entropy method in charge-density studies: aspects of reliability. *Acta Cryst. A* **49**, 590–591.

Kumazawa, S. (1993). MEED: a program package for electron-density-distribution calculation by the maximum-entropy method. *J. Appl. Cryst.* **26**, 453–457.

Nishibori, E. (2002,2003). priv. comm.

Papoular, R. J. & Gillon, B. (1990). Maximum-entropy reconstruction of spin-density maps in crystals from polarized neutron-diffraction data. *Europhys. Lett.* **13**, 429–434.

Papoular, R. J., Vekhter, Y. & Coppens, P. (1996). The two-channel maximum-entropy method applied to the charge density of a molecular crystal: alpha-glycine. *Acta Cryst. A* **52**, 397–407.

Saka, T. & Kato, N. (1968). Accurate measurement of the Si structure factor by the Pendellösung method. *Acta Cryst. A* **42**, 469–478.

Sakata, M. & Sato, M. (1990). Accurate structure analysis by the maximum-entropy method. *Acta Cryst. A* **46**, 263–270.

Sakata, M., Uno, T. & Takata, M. (1993). Maximum-entropi-method analysis of neutron diffraction data. *J. Appl. Cryst.* **26**, 159–165.

Skilling, J. & Bryan, R. K. (1984). Maximum entropy image reconstruction: General algorithm. *Mon. Not. R. Astron. Soc.* **211**, 111–124.

Tanaka, H., Takata, M., Nishibori, E., Kato, K., Lishi, T. & Sakata, M. (2002). ENIGMA: maximum-entropy method program package for huge systems. *J. Appl. Cryst.* **35**, 282–286.

Part II

Papers

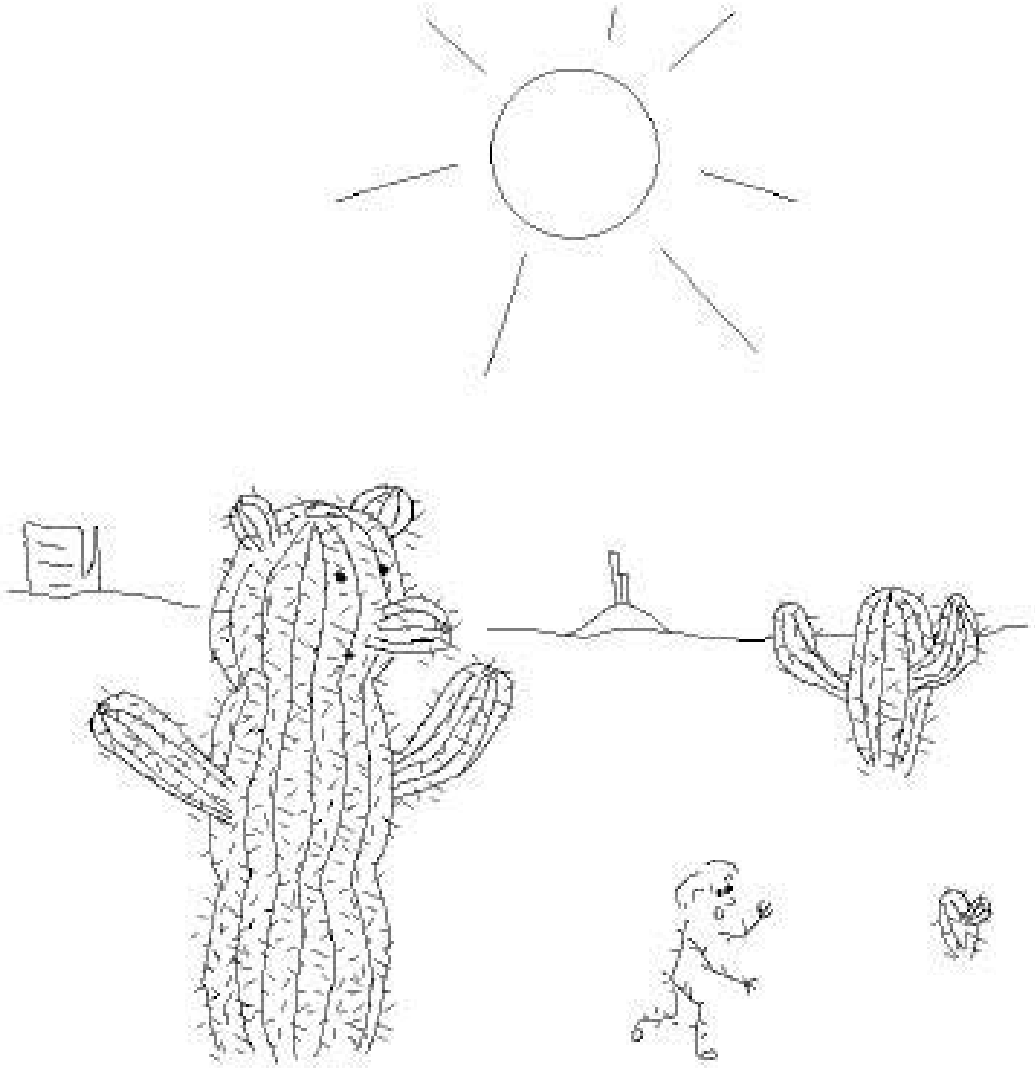

The Teddy Bear Cactus, Arizona 2001

URN:NBN:no-7231

Paper 1

Quantitative Convergent Beam Electron Diffraction Measurements of Low Order Structure Factors in Copper

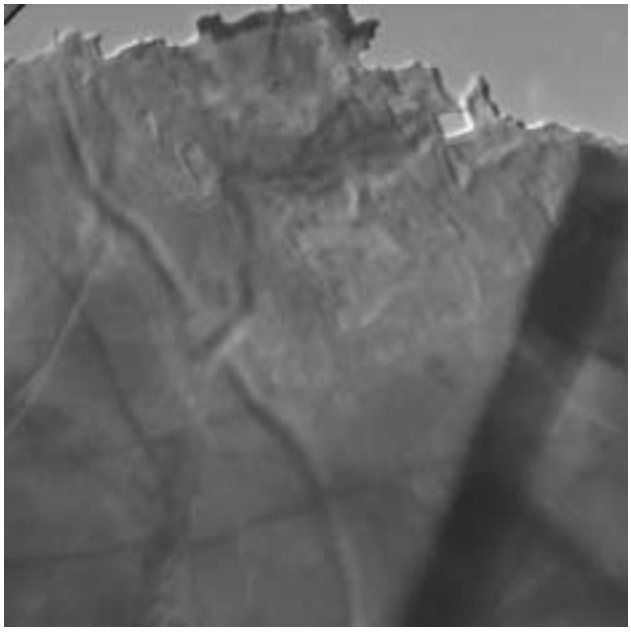

TEM image of the thin area of the Cu sample used for experiments. Magnification: 4000 times.

URN:NBN:no-7231

Microsc. Microanal. 9, 379–389, 2003
DOI: 10.1017/S1431927603030319

Microscopy AND Microanalysis

Quantitative Convergent Beam Electron Diffraction Measurements of Low-Order Structure Factors in Copper

Jesper Friis,[1]* Bin Jiang,[2] John C.H. Spence,[2] and Randi Holmestad[1]

[1]*Department of Physics, Norwegian University of Science and Technology (NTNU), 7491 Trondheim, Norway*
[2]*Department of Physics, Arizona State University, Tempe, AZ 85287-1504, USA*

Abstract: Accurate low-order structure factors for copper metal have been measured by quantitative convergent beam electron diffraction (QCBED). The standard deviation of the measured structure factors is equal to or smaller than the most accurate measurement by any other method, including X-ray single crystal Pendellösung, Bragg γ-ray diffraction, and high-energy electron diffraction. The electron structure factor for the (440) reflection was used to determine the Debye-Waller (DW) factor. The local heating of the specimen by the electron beam is determined to be 5 K under the current illumination conditions. The low-order structure factors for copper measured by different methods are compared and discussed. The new data set is used to test band theory and to obtain a charge density map. The charge deformation map shows a charge surplus between the atoms and agrees fairly well with the simple model of copper 2+ ions at the atomic sites in a sea of free uniformly distributed electrons.

Key words: quantitative convergent beam electron diffraction, QCBED, structure factor, copper, bonding, free electron model

Introduction

The aim of the present work is to get a better understanding of the role of the free electrons in the bonding of copper. The structure factors for copper have been studied by many researchers using different methods over the last 30 years. A new data set is added here using the quantitative convergent beam electron diffraction (QCBED) method (see Zuo, 1998; Holmestad et al., 1999, and references therein). The electron diffraction method measures Fourier coefficients of the ground state electrostatic Coulomb potential, including the nuclear contribution (electron structure factors). These may then be converted to X-ray structure factors (Fourier coefficients of the electron charge density) using the reciprocal space form of Poisson's equation if the temperature factors and nuclear coordinates are known. The operation of this equation provides the enhanced sensitivity of electron diffraction to bonding effects by comparison with X-ray diffraction, as does the elimination of extinction errors discussed further below. There has recently been considerable discussion of low-order structure factor measurement methods (Zuo et al., 2000; Jiang et al., 2002, 2003*a*, 2003*b*). The study of copper provides a good opportunity to compare the accuracy and credibility of different methods.

Low-order structure factors are crucial when studying bonding in crystals. The accuracy of the measurements should normally be below 1% in order to see the deformation of the charge density due to bonding effects.

Received December 10, 2001; accepted September 10, 2002.
**Corresponding author*. E-mail: jesper.friis@phys.ntnu.no

Various methods have been used for low-order structure factor measurements. They are: (1) Bragg X-ray or γ-ray diffraction, (2) critical voltage (CV), (3) X-ray single crystal Pendellösung, and (4) quantitative convergent beam electron diffraction. These methods all have their advantages and disadvantages, which will be discussed briefly here.

Bragg X-ray or γ-ray diffraction normally suffers from large extinction errors in the strong low-order reflections of inorganic crystals. The advantage is that these methods can very accurately measure high-order reflections, which are sensitive to atomic coordinates and Debye-Waller (DW) factors, and can be used for crystal structure determination.

The CV method is capable of measuring the ratio of two low-order structure factors. Errors may be as small as 0.1% (Spence & Zuo, 1992). The disadvantage of this method is that one structure factor must be accurately known to calculate the other.

The X-ray single crystal Pendellösung and the QCBED methods are similar techniques in terms of the underlying theory. Both use perfect crystals and are based on dynamical theory. Both give highly accurate low-order structure factor data. A disadvantage of the X-ray Pendellösung method is that it requires large perfect crystals, which limits its application to a few semiconductor crystals such as silicon, diamond, and so forth. The QCBED method, on the other hand, takes advantage of the small probe of a transmission electron microscope (TEM), which allows one to use a perfectly crystalline region of near nanometer size. This is smaller than the size of one mosaic block. The disadvantage of QCBED is that it cannot be used to measure high-order reflections accurately. Because of their high accuracy and credibility, structure factors measured by these two methods are often used to test band theory. In this way, random errors can be made very small—systematic errors can only be minimized by comparing the results of different techniques.

Experiment

Sample Preparation and Experimental Setup

The specimen was prepared by electrolytic polishing. The electrolyte was 33% phosphoric acid and 67% water (Hirsch et al., 1977). A pure copper foil (99.999%) of a 25-μm thickness was polished at 10 V and 4 A/cm^2 at room temperature.

We found that copper was easily oxidized when exposed to air, which may cause extra diffraction spots and introduce a large standard deviation in the refined data. Therefore, newly prepared samples were mounted on a Gatan liquid nitrogen holder and put into the microscope vacuum immediately after thinning.

A LEO 912B transmission electron microscope, operating at 120 keV, with in-column Ω-filter and a Gatan MSC CCD (14-bit dynamical range) camera, was used. The CCD camera was properly characterized to compensate for the point spread function (Jiang et al., 2003*a*, 2003*b*). The energy window used in the experiments was 10 eV. The experiments were done at liquid nitrogen temperature, using a Gatan double tilt cooling holder. This avoids contamination and reduces the phonon scattering background, which is otherwise difficult to fit. The temperature readout from the holder varied between the experiments from 107 K to 112 K. The CBED patterns were acquired using a probe size of less than 100 Å, using a systematic row orientation far away from major zone axes. This small probe eliminates any effects due to local bending of the ductile copper foil.

High-Voltage Calibration

The high voltage must be calibrated for accurate electron structure factor measurements (Spence & Zuo, 1992). An accurate value is also needed when converting the electron structure factors to X-ray structure factors. This was done using high-order Laue zone (HOLZ) lines. It is well known that the position of HOLZ lines is very sensitive to both electron beam energy and lattice parameters (Spence & Zuo, 1992). Because high voltage and lattice parameters have similar effects on the position of HOLZ lines, it is not possible to measure both these quantities simultaneously. The lattice parameter of silicon, however, is well known and so may be used to calibrate the high voltage. Figure 1 shows the central disk of a silicon [133] zone axis CBED pattern. The two triangles formed by HOLZ lines, shown enlarged in Figure 1b,c, were used for the calibration. The size of these triangles is very sensitive to the high voltage, because the HOLZ lines originate far out on the Ewald sphere. Furthermore, the HOLZ lines are arranged so that they all will move toward each other in Figure 1b and away from each other in Figure 1c, as the high voltage increases. The high voltage is therefore obtained by comparing the ratio between the areas of triangle (b) and (c) with dynamical Bloch wave simulations (Zuo, 1998) done at different voltages (Fig. 2). This gives a high voltage of 119.60 kV.

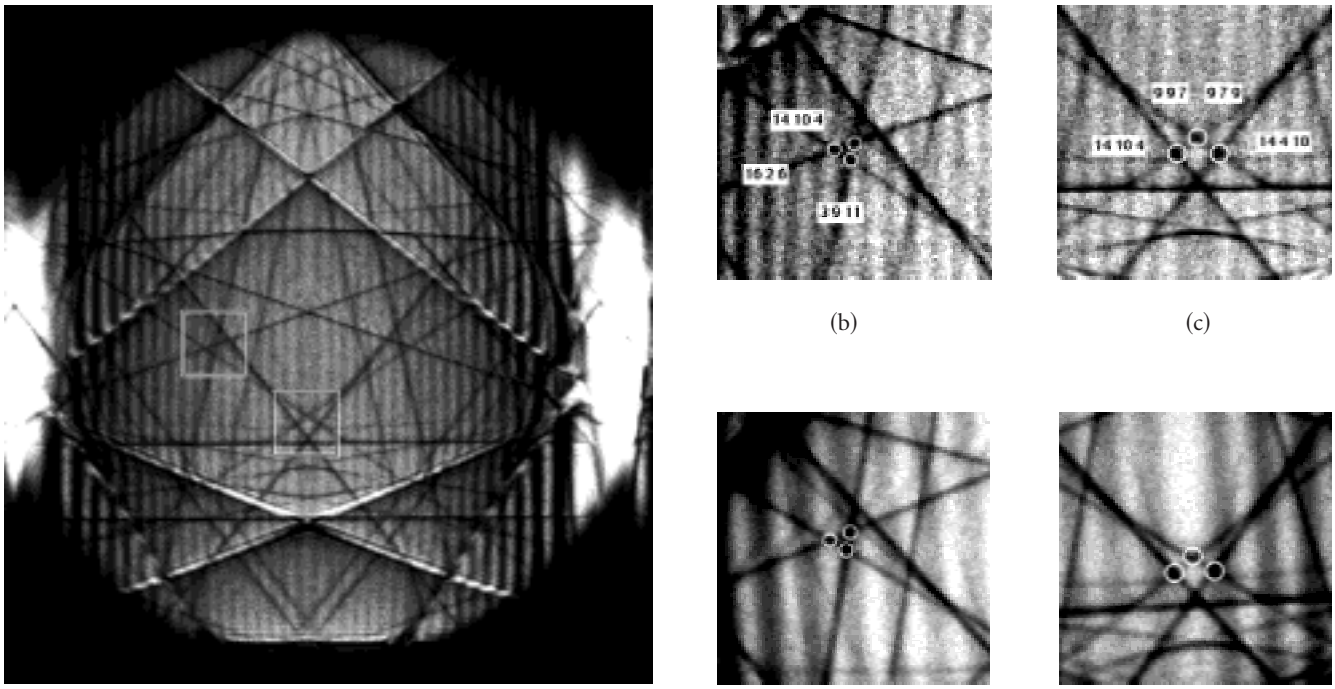

Figure 1. a: The (000) disk of Si [133] zone axis taken with the LEO 912B microscope at Arizona State University, June 2001. The high voltage was measured on this image to be 119.60 kV. **b,c:** Magnifications of the regions around the sensitive triangles made by HOLZ lines. **d,e:** Images are from the same sensitive regions, but taken May 1997 with the same microscope. At that time the high voltage was measured to be 119.52 kV.

The filament of the microscope was changed in March 2001. In Figure 1d,e, we compare the same pattern taken with the same microscope before the filament change (May, 1997). The high voltage was then found to be 119.52 V, which also was confirmed in May 2000 (Jiang et al., 2003*a*, 2003*b*). It can be seen that a change of 80 V in the electron beam energy is easily detected, corresponding to a change in wavelength from 0.0033553 nm to 0.0033563 nm.

Lattice Parameter

Highly accurate lattice parameters are needed for structure factor refinement. In particular, the lattice parameters are important to determine the HOLZ line positions, which define the beam direction ($\mathbf{k}_t$) in the patterns used for refinement.

The crystal structure of copper and its thermal expansion have been studied for many years. Accurate crystal data and the thermal expansion coefficient are available. The measured lattice parameter at room temperature is $a = 3.61496(2)$ Å (Schneider et al., 1981). From this, lattice parameters at other temperatures can be calculated by using the expansion coefficient of Hahn (1970). At 115 K we obtain $a = 3.60540(3)$ Å.

Experimental DW Factor and Temperature Determination

A knowledge of DW or temperature factors is essential for accurate QCBED refinement. Saunders et al. (1999) have shown that good χ^2 values (see equation (1) below) can only be obtained if the correct value of the DW factor is used. Even though the refined electron structure factors are not sensitive to the DW factor, the converted X-ray structure factors will depend on the DW factor. If an incorrect DW factor is used, it will introduce systematic errors in the converted X-ray structure factors, particularly at higher scattering angles. For example, a 5-K change in temperature (around 110 K) will introduce a 3% change in the DW factor and change the converted X-ray structure factor by ± 0.02 electrons/cell (0.025%) for the (200) reflection and by ± 0.4 electrons/cell (1.1%) for the (440) reflection. In addition, accurate temperature factors are needed for all the

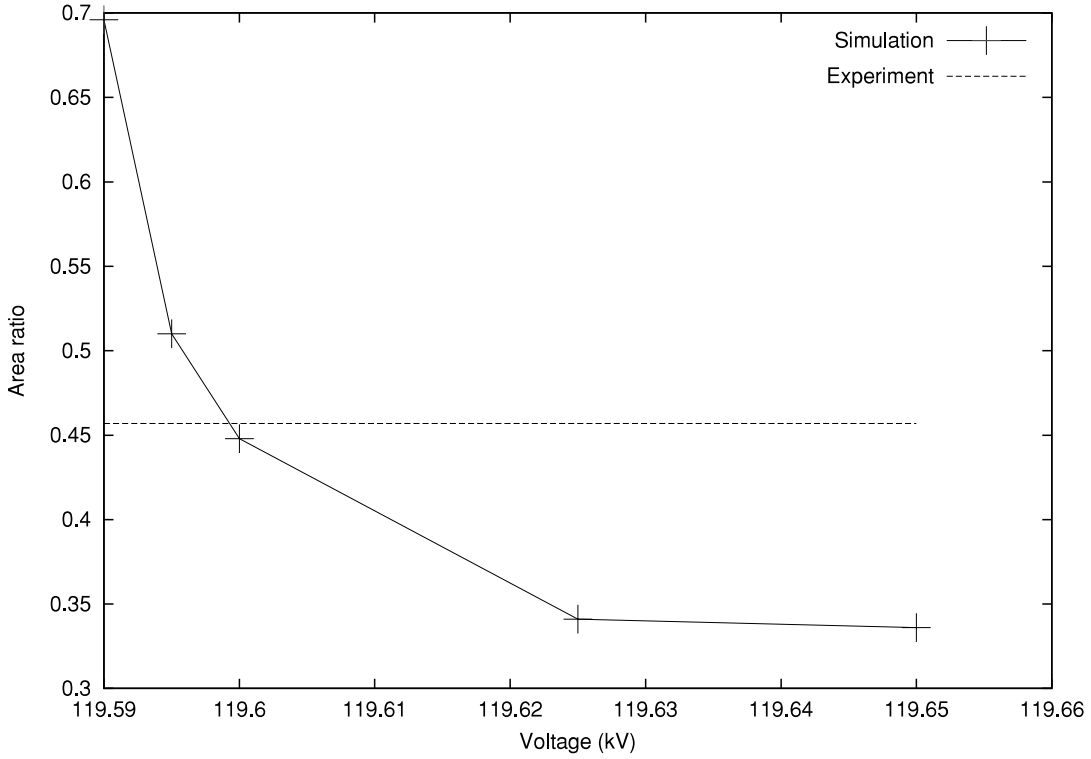

Figure 2. High voltage calibration curve. The *y*-axis shows the ratio between the area of the two sensitive triangles shown in Figure 1b,c. The circles show the ratio obtained from simulations at different voltages, and the horizontal line is the ratio measured on the experimental image. The high voltage is determined from the crossover to be 119.60 kV.

other reflections in the simulation not being refined that affect the refined value through multiple scattering.

The effective isotropic DW factor B for copper has been measured accurately by Schneider et al. (1981) to 0.167(8) Å^2 at 50 K and 0.544(7) Å^2 at room temperature. These values fit well with the expansion of B, given by Sears and Shelley (1991) using the phonon model. This gives us an opportunity to measure the sample temperature, by measuring the DW factor.

A well-known problem in electron diffraction experiments is that the local heating of the specimen by the illuminating electrons is unknown. The local heating depends on the thermal conductivity of the specimen and the illumination conditions. The sensitivity to the DW factor of the converted X-ray structure factor for the (440) reflection suggests that we can measure the DW factor and specimen temperature accurately.

Therefore, the systematic row of (220) and (440) was carefully measured to calibrate the temperature. A region with few HOLZ lines (which makes the refinement easier and more accurate) could be found by tilting about 16.6° from the (001)-zone axis. These data were collected with a temperature readout of 107 K. The U_{440} refined from different diffraction patterns and different rocking curves of the same diffraction pattern was then converted into X-ray structure factors using the Mott formula (Spence & Zuo, 1992). Because the (440) structure factor is not affected much by bonding, the value should be very close to the neutral atom value. Choosing the DW factor to be $B = 0.2478 \pm 0.0013$ Å^2 gave good agreement with the neutral atom X-ray structure factor (Doyle & Turner, 1968), considering the standard deviation in the measurement of U_{440}. This DW factor corresponds to 112.3 ± 0.7 K (Sears & Shelley, 1991). Thus, we conclude that the local specimen heating is about 5.3 K under the current TEM settings.

Because the TEM settings were kept constant, we assume the same local heating for all our experiments, even though the readout temperature of the GATAN holder varied between 107 K and 112 K, due to small leaks in the vacuum surrounding the nitrogen reservoir in the holder.

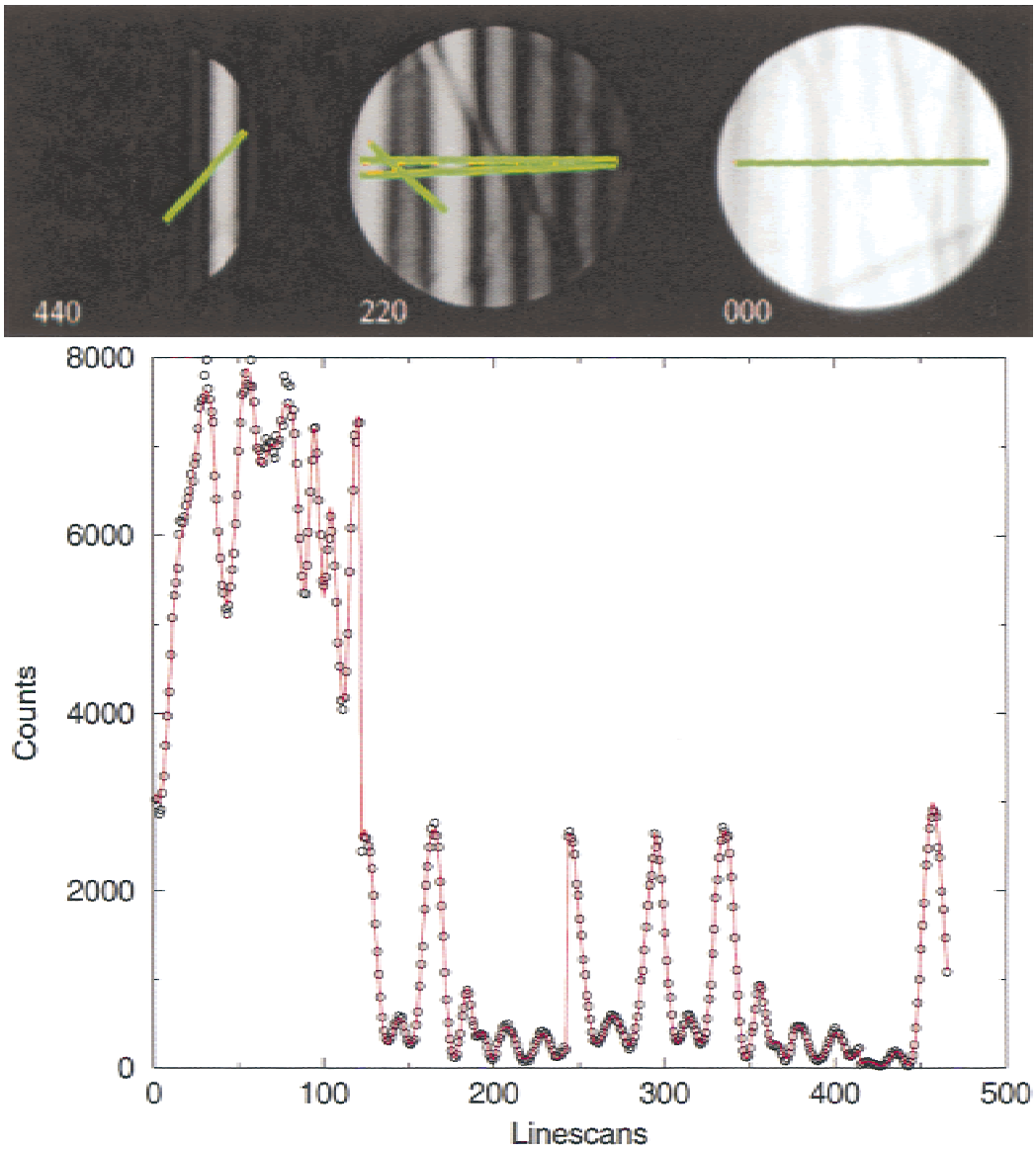

Figure 3. The top image shows the systematic row for (220) and (440) together with the rocking curves chosen for refinement. The graph below shows the pixel values along the above chosen linescans (circles) compared with calculated values (solid line). The χ^2 for this fit is 1.46.

Refinement

Low-Order Structure Factor Refinement

The idea behind the QCBED method is to refine the input parameters in a Bloch wave simulation until a best fit with experiment is obtained. Only pixel intensities along some carefully chosen rocking curves are calculated. In Figure 3, a CBED pattern from the (220) systematic row is shown, with some rocking curves drawn onto it together with the fit along these curves.

As a goodness-of-fit measure, we use χ^2, defined as

$$\chi^2 = \frac{1}{N-f-1}\sum_{i=1}^{N}\frac{(I_i^{(exp)} - cI_i^{(theo)} - I^{(bgr)})^2}{\sigma_i^2}, \qquad (1)$$

where N is the number of data points, f is the number of refined parameters, c a scaling factor, σ the standard deviation of the experimental intensities, and $I_i^{(exp)}$, $I_i^{(theo)}$, and $I^{(bgr)}$ are the experimental, theoretical, and background intensities, respectively. The sum goes over all pixels in the line scans shown in Figure 3. The refinement parameters are

Table 1. Experimental Results for the (200) Structure Factor of Copper[a]

Crystal	Orientation	Rocking curve	χ^2	U_{200} (Å^{-2})	$U_{200}^{(abs)}$ (Å^{-2})	F_{200} (e/atom)
Cryst 1	5.68°, 0.60°	1	1.26	0.08626	0.00346	20.090
Cryst 1	5.68°, 0.60°	2	1.12	0.08664	0.00343	20.068
Cryst 1	5.18°, 0.58°	1	1.40	0.08585	0.00382	20.114
Cryst 1	5.18°, 0.58°	2	1.25	0.08671	0.00383	20.064
Cryst 2	−35.3°, 0.73°	1	1.79	0.08673	0.00370	20.063
Cryst 2	−35.3°, 0.73°	2	2.00	0.08603	0.00390	20.103
Cryst 2	−11.1°, −0.76°	1	3.13	0.08760	0.00370	20.013
Cryst 2	−11.1°, −0.76°	2	3.14	0.08755	0.00385	20.016
Cryst 2	−11.1°, −0.76°	3	2.90	0.08760	0.00375	20.013
Cryst 2	5.25°, −0.65°	1	2.96	0.08784	0.00382	19.998
Average (μ)				0.08698	0.00373	20.054
Standard deviation (σ)				0.00072	0.00016	0.041
Relative standard deviation, (σ/μ, in %)				0.83	4.3	0.21
Standard error ($\sigma/\sqrt{n}$)				0.0002	0.00005	0.013

[a]Orientation is given as a tilt from the (001) zone around the *x*- and *y*-axes, respectively, where the *x*-axis is chosen to be in the (100) direction. The temperature was, in all cases, 114 K, except for the last case, where it was 115 K, corresponding to a DW factor of 0.251 Å^2 and 0.252 Å^2, respectively. A lattice constant of $a = 3.60542$ Å was used to calculate the X-ray structure factors in the last column. To show the consistency of the QCBED method and to improve the statistics, all together 10 refinements were done on two different crystals with different orientations and different rocking curves drawn on each pattern.

certain low-order complex structure factors (including absorption), beam direction $\mathbf{k}_t$, scaling factor c, background intensity $I^{(bgr)}$ (which is assumed constant for each disk), and sample thickness.

The Bethe potential approximation is used in the multiple-scattering calculations. Here, strong beams are treated exactly, whereas weak ones are calculated using perturbation theory. The beams were selected for diagonalization or perturbation according to three criteria (Zuo & Weickenmeier, 1995; Birkeland et al., 1996): (1) $2KS_g$ (proximity to the Ewald sphere), (2) length of g_{max}, (3) $|U_g/2KS_h|_{min}$ (perturbation strength). $2KS_g$ is used to select the beams included in the diagonal matrix, $|U_g/2KS_h|_{min}$ to select the weak beams for perturbation, and g_{max} as a cut-off parameter for high-order reflections. Normally, good convergence can be obtained by choosing values of 3.5 Å^2, 4.0 Å, and 35, respectively, for the three criteria. For more details on QCBED refinement we refer to Zuo (1998).

Consistency Test

To ensure that our results are consistent, refinements have been done on different crystals, at different orientations and with different rocking curves. We then take the average of the results. The relative standard deviation is less than 1% in all cases. In Table 1, all refinements of the (200) reflection are listed with their χ^2 and the corresponding X-ray structure factor. The data set is consistent for measurements from different crystals and different tilts.

Mean Inner Potential and Its Effects on the Refinements

The mean inner potential, V_0, is also considered in the current refinements. We use $V_0 = 23.5$ V for copper (Williams & Carter, 1996). Although this term produces only an unobservable phase factor on zero order Laue zone (ZOLZ) diffraction patterns, it may affect the intensity in three-dimensional multiple scattering. Our refinements show that including the mean inner potential has a small effect on the refined electron structure factors, but it improves the χ^2 values significantly. The reason may be that changes in the mean inner potential introduce significant HOLZ line shifts, which are critical in the determination of $\mathbf{k}_t$ for the experimental patterns. To avoid systematic errors, the mean inner potential was also considered in the high voltage calibration and in the conversion of electron structure factors to X-ray structure factors.

Table 2. List of Measured Static Lattice X-ray Structure Factors for Cu[a]

	Neutral atom	Bragg γ-ray diffraction			White X-ray Pendellösung		Electron diffraction		
hkl	Doyle and Turner (1968)	Schneider et al. (1981)	Mackenzie and Mathieson (1984)	Petrillo et al. (1998)	Takama and Sato (1982)	Smart and Humphreys (1980)	Fox and Fisher (1988)[b]	Saunders et al. (1999*a*)	This experiment (2001)
111	22.05	21.51(5)		21.68(14)	21.80(6)	21.786	21.72(4)	21.78(2)	21.69(4)
200	20.69	20.22(4)		20.38(13)	20.28(11)	20.454	20.45(4)	20.42(2)	20.44(4)
220	16.74	16.45(5)	16.76	16.60(12)	16.75(8)	16.696	16.68(8)	16.71(14)	16.68(3)
311	14.74	14.54(4)		14.68(11)	14.74(4)		14.76(7)		14.74(2)
222	14.19	14.07(5)		14.22(11)	14.36(6)				14.24(8)
400	12.42	12.29(6)		12.42(10)	12.46(6)				12.45(10)
440	8.82			8.92(11)					8.82(4)

[a]Calculated values for a neutral atom model are shown for comparison. Units are in electrons per atom.
[b]The results of Fox and Fisher (1988) were published in Tabbernor et al. (1990).

Results

Refinement Result

Because the temperature varies with each experiment, the refined structure factors were converted into static X-ray structure factors (for which $B = 0.0$ Å^2) by dividing with the temperature factor $\exp(-B \sin^2\theta/\lambda^2)$ before averaging. Approximately 10 refinements were completed for each reflection. The results are listed in Table 2 and compared with other measured X-ray structure factors for copper. In Figure 4, the difference between our experimentally measured X-ray structure factors and neutral atom calculations is shown as a function of scattering angle, $\sin\theta/\lambda$. A significant difference between the measurements and the neutral atom values is observed for the three lowest order structure factors.

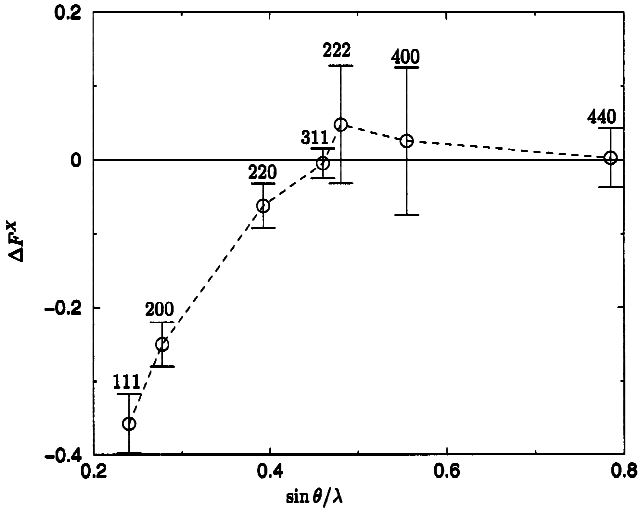

Figure 4. The difference between our measured structure factors (converted to static lattice X-ray structure factors) and calculated neutral atom values (Doyle & Turner, 1968) versus scattering angle.

Deformation Density

The deformation charge density, defined as

$$\Delta\rho(\mathbf{r}) = \frac{1}{\Omega}\sum_{\mathbf{g}}\left[F_{\mathbf{g}}^{X}(\text{crystal}) - F_{\mathbf{g}}^{X}(\text{free atom})\right]e^{2\pi i\mathbf{g}\cdot r}, \quad (2)$$

where Ω is the unit cell volume, measures the redistribution of charge due to bonding. As reference density $F_{\mathbf{g}}^{X}$(free atom), the interpolated relativistic Hartree-Fock structure factors of Doyle and Turner (1968) have been chosen. Because the difference between $F_{\mathbf{g}}^{X}$(crystal) and $F_{\mathbf{g}}^{X}$(free atom) is so small (around 1%), this requires careful consideration of the experimental errors. An electron deformation density map consisting of a section of the (110) plane passing through the nuclei is shown in Figure 5a. Only the six lowest structure factors, up to the (400) reflection ($\sin\theta/\lambda = 0.56$ Å^{-1}), were included. All others were assumed equal to their neutral atom values and will therefore not to contribute to the deformation density map. One has to be very careful when interpreting such a map because

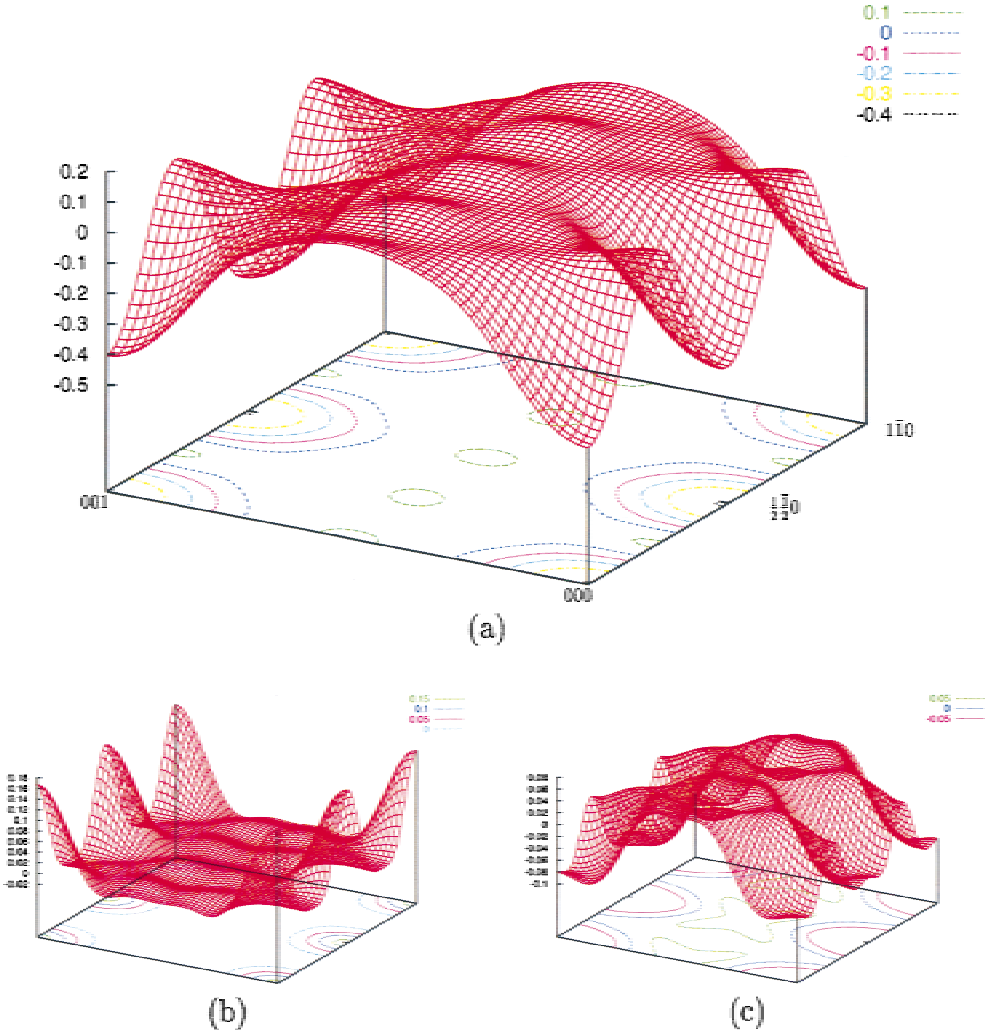

Figure 5. Charge density difference maps of the (110) plane of copper passing through the nuclei. Units are in electrons per cubic Ångström. The plots are calculated from the six lowest order structure factors obtained from (**a**) our QCBED measurements, (**b**) the Cu^{+1}, and (**c**) the Cu^{+2} free atom calculations of Doyle and Turner (1968).

of truncation errors and because the errors in the measured structure factors tend to accumulate at the high symmetry points. Anyway, the map shows a spherical charge depletion at the atomic sites and an evenly distributed charge surplus of about 0.1 e/Å^3 between the atoms.

In Figure 5b,c, we have made similar maps based on two very simple models, assuming (b) Cu^{+1} ions and (c) Cu^{+2} ions at the atomic sites in a sea of one and two fully delocalized electrons, respectively. The maps are created by setting $F_{\mathbf{g}}^{X}$(crystal) to the structure factors calculated from Doyle and Turner's interpolated Cu^{+1} and Cu^{+2} scattering factors, respectively. The $\mathbf{g} = 0$ term of equation (2) is, in this case, omitted in order to keep the total charge difference zero. The models with one free electron do not agree at all with our experimental map, whereas good agreement is achieved in the interstitial region with the model using two free electrons per atom.

Discussion

Various sets of experimental and theoretical structure factors have been published for copper (see, e.g., Mackenzie and Mathieson (1992) and Tabbernor et al. (1990)). We list here some of them for comparison with the current QCBED results. To compare the different sets, they have all been converted to static lattice values.

Table 3. List of Theoretical Calculated Static Lattice X-ray Structure Factors for Cu[a]

	Doyle and Turner (1968)			Wakoh and Yamashita	Bagayoko et al.	MacDonald et al.	Ekardt et al.	This experiment
hkl	Cu	Cu^{+1}	Cu^{+2}	(1971)	(1980)	(1982)	(1984)	(2001)
111	22.05	22.12	21.89	21.72	21.76	21.73	21.95	21.69(4)
200	20.69	20.76	20.61	20.46	20.42	20.39	20.68	20.44(4)
220	16.74	16.78	16.77	16.63	16.67		16.90	16.68(3)
311	14.74	14.76	14.76	14.64	14.76		14.94	14.74(2)
222	14.19	14.21	14.21	14.10	14.23	14.25	14.38	14.24(8)
400	12.42	12.42	12.42	12.34	12.48		12.62	12.45(10)
440	8.82	8.82	8.78				8.94	8.82(4)
R(%)	0.55	0.68	0.48	0.51	0.15	0.17	1.25	
a (Å)	3.6032	3.6032	3.6032		3.6032	3.6145	3.615	3.6054

[a]As a measure of agreement between calculation and our experiment, we use the residual, *R*, listed at the bottom of the table. Because different lattice parameters, *a*, were used in the calculations, they are also listed at the bottom of the table. Units are in electrons per atom.

Comparison with Other Experimental Data

In Table 2, we list some of the earlier diffraction results on copper derived from electron diffraction (CV), Bragg γ-ray diffraction, and white X-ray single crystal Pendellösung. The values obtained by electron diffraction measurement are in good agreement, with no significant differences from the current QCBED measurement. This demonstrates the consistency of the electron diffraction method. The reason is that all these electron diffraction results use perfect crystals as diffraction objects and the full dynamical theory in the calculations.

The difference is quite obvious for the Bragg γ-ray diffraction measurements of Schneider et al. (1981), which are systematically lower than all the other experimental values. This has been pointed out in several previous papers (Mackenzie & Mathieson, 1979, 1984, 1992; MacDonald et al., 1982). The γ-ray diffraction measurements may have scaling problems (Tabbernor et al., 1990). Mackenzie and Mathieson (1984) have also pointed out that the extinction correction used by γ-ray diffraction is not sufficient. They proposed a new correction method and obtained $F_{220}^X = 16.76$ e/Å^3 for the (220) reflection, which is close to the electron diffraction result $F_{220}^X = 16.68(3)$ e/Å^3, but still outside the standard deviation. Petrillo et al. (1998) reanalyzed the values of Schneider et al. (1981). They subtracted the kinematic correction Δ and scaled the original data to fit the neutral atom values for scattering angles greater than 0.5 Å^{-1}. These new values are close to the electron diffraction values but have large error bars.

As mentioned in the Introduction, the X-ray Pendellösung method can measure low-order structure factors very accurately because of its fully dynamical nature, but requires a large perfect wedge-shaped single crystal for accurate measurements. Takama and Sato (1982) have modified this method by doing experiments on relatively small single crystals using white X-ray radiation. This method has the advantage of easy specimen preparation and only requires a tiny single crystal. The accuracy, however, is lower than the conventional X-ray Pendellösung method and electron diffraction. Their original published data set (Takama & Sato, 1982) is, in general, close to the electron diffraction values, but it has large standard deviations for the low-order reflections.

Comparison with Solid-State Calculations

Because of the accuracy of QCBED, it can be used to test band theory, as has been done for silicon by Zuo et al. (1997). Over the past 40 years, many theoretical calculations have been completed for the X-ray structure factors of copper. In Table 3 we list the calculated structure factors of Wakoh and Yamashita (1971), Bagayoko et al. (1980), MacDonald et al. (1982), and Eckardt et al. (1984), together with our experimental values and the free atom values of Doyle and Turner (1968) for Cu, Cu^{+1}, and Cu^{+2}. As a measure of

how well these calculations fit our experiments, we give the residual R, defined as $R = 1/n \sum_i |F_i^X(\text{theory}) - F_i^X(\text{exp})|/F_i^X(\text{exp})$, at the bottom of the table. Because the calculations were done using different lattice parameters, they are also listed in Table 3. All calculations are self-consistent.

The band-structure calculation of Bagayoko et al. (1980), using Gaussian orbitals and a local exchange-correlation potential, gives a good fit to photo-emission spectra as well to the current QCBED experiment. Also, the relativistic field calculations by MacDonald et al. (1982) agree very well with the current experiment. Eckardt et al. (1984) show higher values than the previous studies and this experiment, even though they agree very well with experimental photo-emission spectra.

Charge Distribution

The agreement between the charge difference density maps (Fig. 5) of the Cu^{+2} ions plus free electrons model and our measurements indicate that Cu has two delocalized electrons per atom. This could be explained if one (or more) of the 10 3*d* electrons in the ground state ($3d^{10}4s$) promotes to the delocalized 4*s* or 4*p* bands (see Brewer, 1981).

Conclusion

Accurate low-order structure factors for copper have been measured by electron diffraction. The local heating of the electron beam has been measured to be 5 K under our experimental conditions. Charge density deformation maps, generated from the six inequivalent lowest order reflections, indicate that copper has two delocalized electrons per atom. This result may help to understand how cohesive energy relates to the number of bonding electrons (Brewer, 1981).

Acknowledgments

We thank Prof. Marthinsen (NTNU) and Prof. Zuo (University of Illinois at Urbana-Champaign) for useful discussions. J. Friis acknowledges the funding of the Research Council of Norway (NFR), project 135270/410. B. Jiang is funded by DOG DE-FG03-02ER45596. The experiments were done at the CHREM center at Arizona State University.

References

Bagayoko, D., Laurent, D.G., Singhal, S.P. & Callaway, J. (1980). Band structure, optical properties, and compton profile of copper. *Phys Lett A* **76**, 187–190.

Birkeland, C.R., Holmestad, R., Marthinsen, K. & Hier, R. (1996). Efficient beam-selection criteria in quantitative convergent beam electron diffraction. *Ultramicroscopy* **66**, 89.

Brewer, L. (1981). The role and significance of empirical and semiempirical correlations. In *Structure and Bonding in Crystals*, O'Keeffe, M. & Navrotsky, A. (Eds.), pp. 155–174. New York: Academic Press.

Doyle, P.A. & Turner, P.S. (1968). Relativistic Hartree–Fock X-ray and electron scattering factors. *Acta Cryst A* **24**, 390–397.

Eckardt, H., Fritsche, L. & Noffke, J. (1984). Self-consistent relativistic band structure of the noble metals. *J Phys F* **14**, 97–112.

Hahn, T.A. (1970). Thermal expansion of copper from 20 to 800 K—Standard reference material. *J Appl Phys* **41**, 5096–5101.

Hirsch, P.S., Howie, A., Nicholson, R.B., Pashley, D.M. & Whelan, M. (1977). *Electron Microscopy of Thin Crystals*. Malabar, FL: Robert E. Krieger Publ. Co. Inc.

Holmestad, R., Birkeland, C., Marthinsen, K., Høier, R. & Zuo, J.M. (1999). Use of quantitative convergent beam electron diffraction in materials science. *Microsc Res Technique* **46**, 130–145.

Jiang, B., Zuo, J.M., Chen, Q. & Spence, J.C.H. (2002). Orbital ordering in $LaMnO_3$—Estimates of structure factors and comparison of measurement method. *Acta Cryst A* **58**, 4–11.

Jiang, B., Zuo, J.M., Friis, J. & Spence, J.C.H. (2003*a*). On the consistency of QCBED structure factor measurements for TiO_2 (rutile). *Micros Microanal* **9**, 457–467.

Jiang, B., Zuo, J.M., O'Keefe, M. & Spence, J.C.H. (2003*b*). Charge density and chemical bonding of rutile, TiO_2. *Acta Cryst A* **59**, in press.

MacDonald, A.H., Daams, J.M., Vosko, S.H. & Koelling, D.D. (1982). Non-muffin-tin and relativistic interaction effects on the electron structure of noble metals. *Phys Rev B* **25**, 713–725.

Mackenzie, J.K. & Mathieson, A. (1979). The absolute measured value of f(220) for Cu—The importance of extrapolation to zero extinction. *Acta Cryst A* **35**, 5–57.

Mackenzie, J.K. & Mathieson, A. (1984). The experimental value of f(220) for copper. *Aust J Phys* **37**, 651–656.

Mackenzie, J.K. & Mathieson, A. (1992). Band-structure calculations and structure-factor estimates of Cu—Their complementarity. *Acta Cryst A* **48**, 231–236.

Petrillo, C., Sacchetti, F. & Mazzone, G. (1998). Relevance of charge-density measurements for high-precision calculations. *Acta Cryst A* **54**, 468–480.

Saunders, M., Fox, A.G. & Midgley, P.A. (1999). Quantitative zone-axis convergent-beam electron diffraction (CBED) studies

of metals. II. Debye–Waller-factor measurements. *Acta Cryst A* **55**, 480–488.

Schneider, J.R., Hansen, N.K. & Kretschmer, H. (1981). A charge density study of copper by gamma-ray diffractometry on imperfect single crystals. *Acta Cryst A* **37**, 711–722.

Sears, V.F. & Shelley, S.A. (1991). Debye–Waller factor for elemental crystals. *Acta Cryst A* **47**, 441–446.

Smart, D.J. & Humphreys, C.J. (1980). The application of electron diffraction to determine bonding change densities in crystals. *Inst Phys Conf Ser No. 526*, 211–214.

Spence, J.C.H. & Zuo, J.M. (1992). *Electron Microdiffraction*. New York: Plenum Press.

Tabbernor, M.A., Fox, A.F. & Fisher, R.M. (1990). An accurate reappraisal of the elemental form factors and charge density of copper. *Acta Cryst A* **46**, 165–170.

Takama, T. & Sato, S. (1982). Atomic scattering factors of copper determined by Pendellösung intensity beat measurements using white radiation. *Philos Mag B* **44**, 615–626.

Wakoh, S. & Yamashita, J. (1971). Theoretical form factors of 3D transition metals. *Phys Soc Jpn* **30**, 422–427.

Williams, D.B. & Carter, C.B. (1996). *Transmission Electron Microscopy*. New York: Plenum Press.

Zuo, J.M. (1998). Quantitative convergent beam electron diffraction. *Mater Trans, JIM* **39**, 938–946.

Zuo, J.M., Blaha, P. & Schwarz, K. (1997). The theoretical charge density silicon: Experimental testing of exchange and correlation potentials. *J Phys Condens Matter* **9**, 7541–7561.

Zuo, J.M., O'Keeffe, M., Kim, M. & Spence, J.C.H. (2000). On closed-shell interactions, polar covalences, d shell moles, and direct images of orbitals: The case of cuprite. *Angew Chem Int Ed* **39**, 3791–3794.

Zuo, J.M. & Weickenmeier, A. (1995). On the beam selection and convergence in the Bloch-wave method. *Ultramicroscopy* **57**, 375.

Paper 2

On the Consistency of QCBED structure factor measurements for TiO_2 (Rutile)

Microsc. Microanal. 9, 457–467, 2003
DOI: 10.1017/S1431927603030381

Microscopy AND Microanalysis

On the Consistency of QCBED Structure Factor Measurements for TiO_2 (Rutile)

Bin Jiang,[1]* Jian-Min Zuo,[2] Jesper Friis,[1,3] and John C.H. Spence[1]

[1]*Department of Physics, Arizona State University, Tempe, AZ 85287-1504, USA*
[2]*Department of Material Science and Engineering, University of Illinois, Urbana, IL 61801, USA*
[3]*Department of Physics, Norwegian University of Science and Technology, Trondheim, Norway*

Abstract: The same Bragg reflection in TiO_2 from 12 different (CBED) patterns (from different crystals, orientations, and thicknesses) are analyzed quantitatively to evaluate the consistency of the quantitative CBED method for bond-charge mapping. The standard deviation in the resulting distribution of derived X-ray structure factors is found to be an order of magnitude smaller than that in conventional X-ray work, and the standard error (0.026% for $F_X(110)$) is slightly better than obtained by the X-ray Pendellösung method applied to silicon. This is sufficiently accurate to distinguish between atomic, covalent, and ionic models of bonding. We describe the importance of extracting experimental parameters from CCD camera characterization, and of surface oxidation and crystal shape. The current experiments show that the QCBED method is now a robust and powerful tool for low-order structure factor measurement, which does not suffer from the large extinction (multiple scattering) errors that occur in inorganic X-ray crystallography, and may be applied to nanocrystals. Our results will be used to understand the role of d-electrons in the chemical bonding of TiO_2.

Key words: electron diffraction, CBED, structure factor, rutile

Introduction

The ultimate aim of this work is to understand the role of *d* electrons in the chemical bonding of TiO_2 (rutile) and the charge state of Ti(IV) ions common to many important electronic ceramics. Here we analyze the consistency of the convergent-beam electron diffraction (CBED) method used to measure the bond-charge density, by comparing measurements of the same structure factors in different crystals and orientations. The excellent agreement increases confidence that possible systematic errors, ranging from sample inhomogeneity to convergence of calculations, have been minimized. Some final structure factor measurements, and details of the experimental methods, are provided. By comparison with our earlier work on silicon, GaAs, Cuprite, and MgO (Zuo et al., 1998), a number of new problems arose, indicating the sensitivity of the method to TEM sample quality and shape (boundary conditions) resulting from the sensitivity of TiO_2 to ion beam thinning and the use of crushed samples. A new detector system, with improved dynamic range over our previous camera, had to be characterized, for which we give details. We compare a total of 12 different data sets (CBED patterns). For an earlier comparison of the same reflection refined at different thicknesses (and structure-factor phase measurement with an accuracy of about 0.1°), see Zuo and Spence (1993). Random errors as small as 0.026% are obtained here for rutile crystal, quite sufficient

Received October 23, 2001; accepted September 20, 2002.
*Corresponding author. E-mail: jiangb@asu.edu

to see bonding effects and test theoretical approximations, and the smallest random error yet obtained. In a subsequent paper, we will report details of the multipole analysis of the final charge density, and discuss its implications for the molecular orbitals that take part in bonding.

Several methods have been used to measure low-order structure factors: (1) the X-ray single crystal Pendellösung method, (2) Bragg diffraction by X rays and γ rays, (3) the critical voltage (CV) of electron diffraction, and (4) quantitative convergent beam electron diffraction (QCBED).

The X-ray Pendellösung method can measure structure factors very accurately (standard error 0.07% at best for silicon; Aldred & Hart, 1973). We use the term standard error to refer to the standard deviation of the mean value, and distinguish this from the standard deviation, which we also evaluate. (The X-ray community uses mostly standard error, especially for Pendellösung work.) The Pendellösung accuracy is about the same as the best accuracy obtained by CV and QCBED. The sensitivity to structure factors is about the same for CV and QCBED; however, accurate measurement of structure factors by CV requires known high-order structure factors (see below). The disadvantage of the Pendellösung method is that it requires large defect-free crystals, which severely limits its application to crystals such as silicon, diamond, GaAs, and germanium single crystals that have low defect density.

Conventional Bragg X-ray diffraction from inorganic materials normally suffers from large extinction errors (due to multiple scattering) for the strong low-order reflections that are crucial for charge density maps of bonding. Bragg γ-ray diffraction using high-energy radiation may reduce absorption and extinction effects, but does not eliminate them, and the flatter Ewald sphere may increase multiple scattering (Lippmann & Schneider, 2000).

The CV method of electron diffraction is capable of highly accurate measurements of the ratio of the two lowest order structure factors (Spence & Zuo, 1992). Errors may be as small as 0.1%. The disadvantage is that this method can only give the ratio of the two structure factors. One must be known accurately to calculate the other one.

Recent progress in energy-filtered QCBED has made extinction-free measurements of low-order structure factors possible on an absolute scale (Zuo et al., 1999). This method takes advantage of the small electron probe (of nanometer dimension, smaller than one "mosaic block") and of the sensitivity of QCBED to low-order bonding reflections that results from the Θ^{-4} dependence of electron scattered intensity on scattering angle Θ for low angles (Spence & Zuo, 1992). When combined with TEM, the crystal can be imaged at the atomic level, and it is easy to find a defect-free crystal region for electron diffraction, to which the dynamic diffraction theory can be applied. Using this method, combined with X-ray diffraction to measure the high-order structure factors, Zuo et al. (1999) recently directly observed the *d* orbital holes and Cu-Cu bonding in Cu_2O crystal (for discussion of this work, see Zuo et al., 2000). Readers are referred to our earlier paper (Jiang et al., 2002) and book (Spence & Zuo, 1992) for more details and background.

Experiment

TEM and Ω-Filter

CBED patterns were obtained on a Leo-921B Ω electron microscope operating at 120 keV, with in-column imaging Ω-filter and a Gatan MSC CCD camera. Two types of commercial energy filters are available—the in-column Ω energy filter and the postcolumn Gatan Imaging Filter (GIF). For electron diffraction, the geometric distortion, isochromaticity, and angular acceptance are the most important characteristics of the energy filters (Rose & Krahl, 1995). Theoretically the in-column Ω-filter has smaller distortion due to its midplane symmetry, and is particularly simple to use, with a large acceptance angle, acceptable variation of energy-window center energy with angle, and little or no alignment needed. The energy window used for diffraction recording is normally 10 eV.

CCD Characterization

A new 1,024 × 1,024 × 14 bit GATAN MSC CCD camera was installed in the Leo-912B microscope in March 2000. Detector characterization is a crucial aspect of QCBED work, and, for CCD cameras especially, the goodness-of-fit (GOF) indexes obtained depend sensitively on how the detector response is measured and deconvoluted. For a detailed comparison of CCD, image-plate, and film systems (with comparisons of measured modulation transfer function (MTF), detective quantum efficiency (DQE), and gain for each) see Zuo (2000). The CCD characteristics were measured by the noise method (Zuo, 1996), in which the shot noise from the electron beam is used to provide an equally weighted spectrum of spatial frequencies. The important characteristics of the CCD to be used in deconvolution of CBED data are MTF function, gain, and DQE.

Gain is defined as the ratio of the average number of CCD output counts $\bar{I}$ to the electron dose per pixel N_e:

$$g = \frac{\bar{I}}{\bar{N}_e}. \tag{1}$$

The gain was obtained by making absolute intensity measurements of the electron beam (using the calibrated Fuji image plate system) and comparing these with the numbers per pixel output by the Digital Micrograph program.

The resolution of the slow-scan (SSC) CCD camera is described by its point spread function. The best achievable resolution in the SSC camera is one pixel. For our CCD, additional spreading occurs, mainly in the scintillator and fiber-optics coupling (crosstalk). In both cases, the spreading has approximate rotational symmetry. The MTF function is defined as the modulus of the Fourier transform of the point spread function (PSF). If the PSF function is δ-function, the MTF will be unity for all spatial frequencies. The MTF function can be modeled for Gatan CCD cameras by the simple function (Zuo, 1996):

$$M(\omega) = \frac{a}{1+\alpha\omega^2} + \frac{b}{1+\beta\omega^2} + c. \tag{2}$$

Here ω is spatial frequency in units of 1/pixel. The MTF is given, in all essentials, by the noise spectrum in the Fourier transform of an image of a uniformly illuminated field, averaged over many exposures.

The DQE is defined as the square of the ratio of output signal-to-noise ratio to input signal-to-noise ratio. A figure of unity is only possible if every beam electron is detected, with no noise added and the ideal PSF. DQE can be shown (Zuo, 1996) to be given by

$$DQE(I) = \frac{mg\bar{I}}{\mathrm{var}(I)}, \tag{3}$$

where m is a mixing factor measuring crosstalk between pixels (obtainable from the area under the MTF), g is the gain, $\bar{I}$ is the average number of CCD counts per pixel, and $\mathrm{var}(I)$ is the variance in that number. These quantities are obtained by recording a uniformly illuminated field at different average intensity. The dependence of DQE on intensity has been modeled by an expression involving the parameters of the CCD (Zuo, 1996):

Table 1. Parameters for Measured MTF (Curves in Figure 1), DQE (in Figure 2), Mixing Factor and Gain of CCD Characteristics[a]

HV (kV)	a	α	b	β	c
119.52	0.113	3,396.7	0.858	6.67	0.0228
HV (kV)	**m**	**g**	**$\mathrm{var}(B)$**	**Δ**	**$1+F+1/mG$**
119.52	0.25767	1.55	2.40	4.57e-6	1.424

[a]Please refer to equations (1), (2), and (3) in the text for the definition of these parameters.

$$DQE = \frac{SNR_{\mathrm{out}}^2}{SNR_{\mathrm{in}}^2} = \left[1 + F + \frac{1}{mG} + \frac{\Delta\bar{N}_e}{m} + \frac{\mathrm{var}(B)}{mg^2\bar{N}_e}\right]^{-1} \tag{4}$$

where F, G, Δ, $\mathrm{var}(B)$ are constants. Readers are referred to Zuo (1996) for practical details of DQE measurement.

The measured gain, MTF, and DQE characteristics are shown in Table 1, and in Figures 1 and 2. Compared with our earlier 12-bit Gatan SSC CCD (Zuo, 1996), this new CCD has larger gain, and better MTF and DQE, which all contribute to the better quality and accuracy of the CBED data, resulting in smaller χ^2 values.

TEM Alignment

TEM alignment is very important for accurate QCBED measurement, particularly diffraction astigmatism correction. The TEM was aligned to its best condition to ensure the quality of the measured data. The diffraction astigmatism was corrected using a standard aluminum specimen, resulting in no observable astigmatism in the diffraction pattern. Figure 3 shows one of the ring patterns of an aluminum fine powder. Direct measurement of the circle shows that the deformation from circularity is negligible.

Beam Energy Calibration

It is well known that HOLZ lines shifts due to accelerating voltage and lattice constant changes are not independent; thus it is not possible to measure both high voltage and crystal constants from a single diffraction pattern. A crystal with known lattice constant was therefore used to calibrate the high voltage. The silicon (133) zone pattern shown in Figure 4 was used for this purpose. The "Extal" software

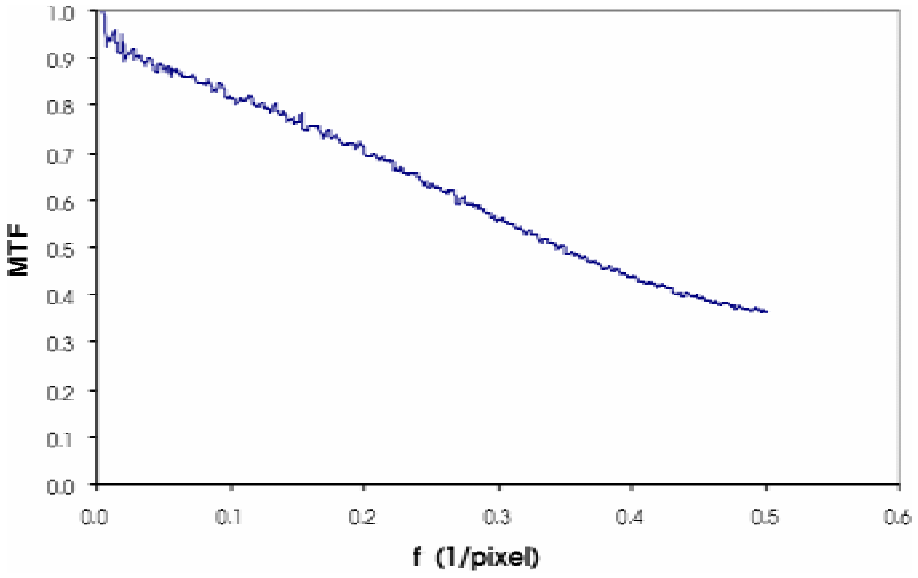

Figure 1. Experimental measured MTF of Gatan MSC 14-bit CCD camera.

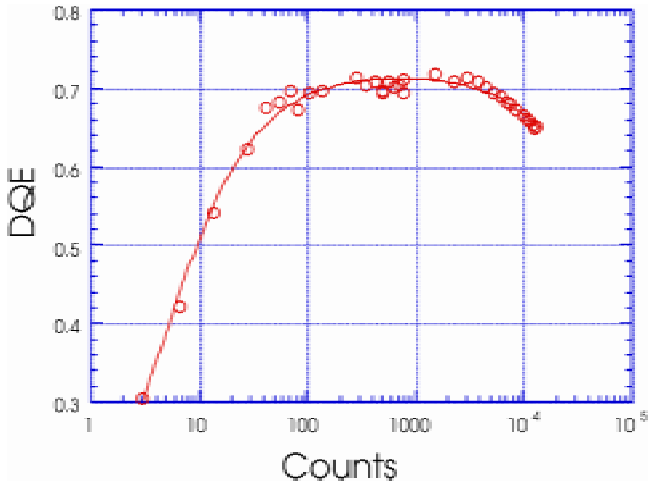

Figure 2. Experimental measured DQE curve of the Gatan MSC 14-bit CCD camera.

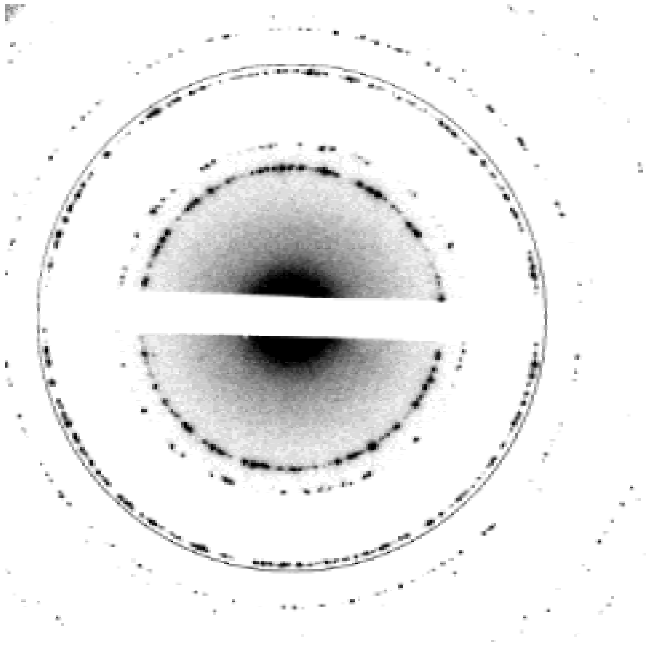

Figure 3. TEM diffraction astigmatism was corrected by a standard aluminum powder. The ring pattern is quite circular with no observable astigmatism.

(Zuo, 1998) was used to refine the high voltage, by matching of calculated patterns (including multiple scattering) to experimental CBED patterns. The high voltage was thus measured to be 119.52 keV.

Specimen Preparation for Rutile

Because rutile is rather sensitive to ion beam radiation, samples prepared by the standard ion milling specimen preparation method left a thin oxygen-deficient layer, giving extra diffraction spots. This introduces large random and systematic error in the refined data. This subtle effect on the refinement took some time to identify and resulted for a long time in reasonably good χ^2 figures, but obviously incorrect structure factors. We attribute the good χ^2 figures

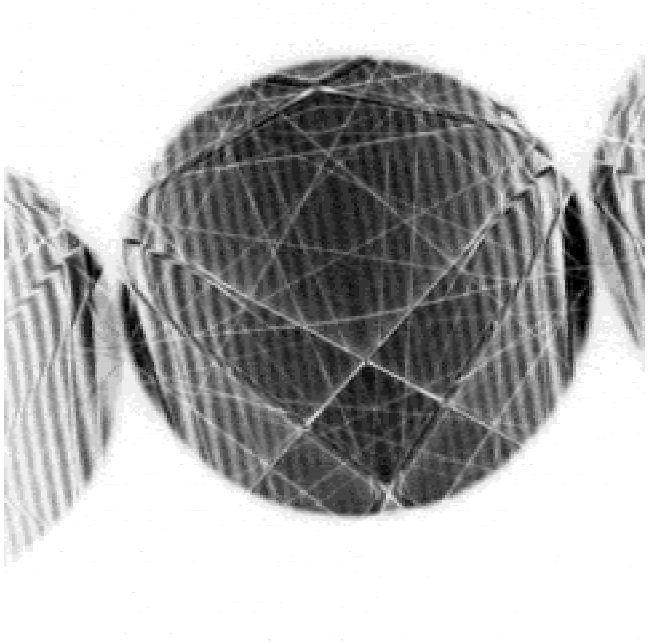

Figure 4. Silicon (331) zone axis pattern used for TEM high-voltage calibration. The high voltage was calibrated as 119.52 keV.

to the parallel-sided nature of the ion-beam samples (the EXTAL program does take into account a tilted, but parallel-sided sample). High accuracy in structure-factor measurement requires the thickness estimate to be accurate to within a few Ångstroms (Zuo et al., 1997). Crushed samples were finally used to ensure cleanness of the sample surfaces, and these produced both excellent χ^2 values at a deep minimum (see Fig. 6) and correct structure factors. Fortunately, large thin areas can be found on the edge of the crushed crystals for CBED experiments. The samples were crushed in a mortar and pestle under alcohol, and collected on holey carbon grids. This produced wedge-shaped cleavage surfaces, which introduced other problems due to the inclined boundaries. It was found that the best GOF factors were obtained from systematic rows running parallel to the wedge edge, which greatly limited the number of useful crystals. This problem is similar to the much earlier finding (Goodman, 1974) that CBED patterns from wedge-shaped crystals do not display the correct point group for a crystal, because the patterns show the symmetry of the sample (including its boundaries, which may destroy symmetry elements) rather than that of an infinite lattice. We use an LaB_6 source with a probe size of 10 nm (measured), smaller than in earlier work. The even smaller probe possible with a field-emission gun would reduce these artifacts.

Refinement

Specimen Thickness

The experimental conditions have to be chosen carefully. The thickness should be between 600 and 1,500 Å, depending on individual reflections for a 120-kV electron beam, and is returned by EXTAL at an early stage of the refinement. A reasonable thickness was chosen to ensure that the CBED fringes within the CBED disk could give accurate thickness information; normally three or more thickness fringes were required and the inclusion of 2g and −g reflections in the refinement improves the reliability of the technique. Higher accelerating voltage would produce more fringes.

Experimental Intensity Measurement

Due to the point-spread function H of the CCD camera, the raw data collected is the convolution between the PSF and the incident beam intensity, plus the noise introduced in the detection process. The raw image recorded can be written as

$$\chi = H \otimes I + n. \tag{5}$$

Here χ represents the image recorded by the CCD and I is the incident CBED pattern and $\otimes$ denotes convolution. The PSF has been experimentally measured, and its Fourier transformation is the modulation transfer function.

The effects of the PSF can be removed partially by deconvolution. But direct deconvolution in reciprocal space, using the measured MTF function, produces excessive amplification of noise, due to the amplification of high spatial frequencies, which reflects mostly pixel-to-pixel variations from noise. Therefore we use the Richardson–Lucy image restoration algorithm, which is optimized for images with Poisson noise (Snyder et al., 1993; Zuo, 2000). The image restoration works by repeat iteration using

$$Q(u,v) = \frac{H^*(u,v)}{H^*(u,v)H(u,v) + \alpha P(u,v)}. \tag{6}$$

The iteration is stopped when

$$\|\chi - H \otimes \hat{I}\| = \|n\|. \tag{7}$$

Here the χ and $\hat{I}$ are the recorded and deconvoluted CBED patterns, n is the estimated additional noise introduced during the recording process, and α (typically smaller than one) is a parameter.

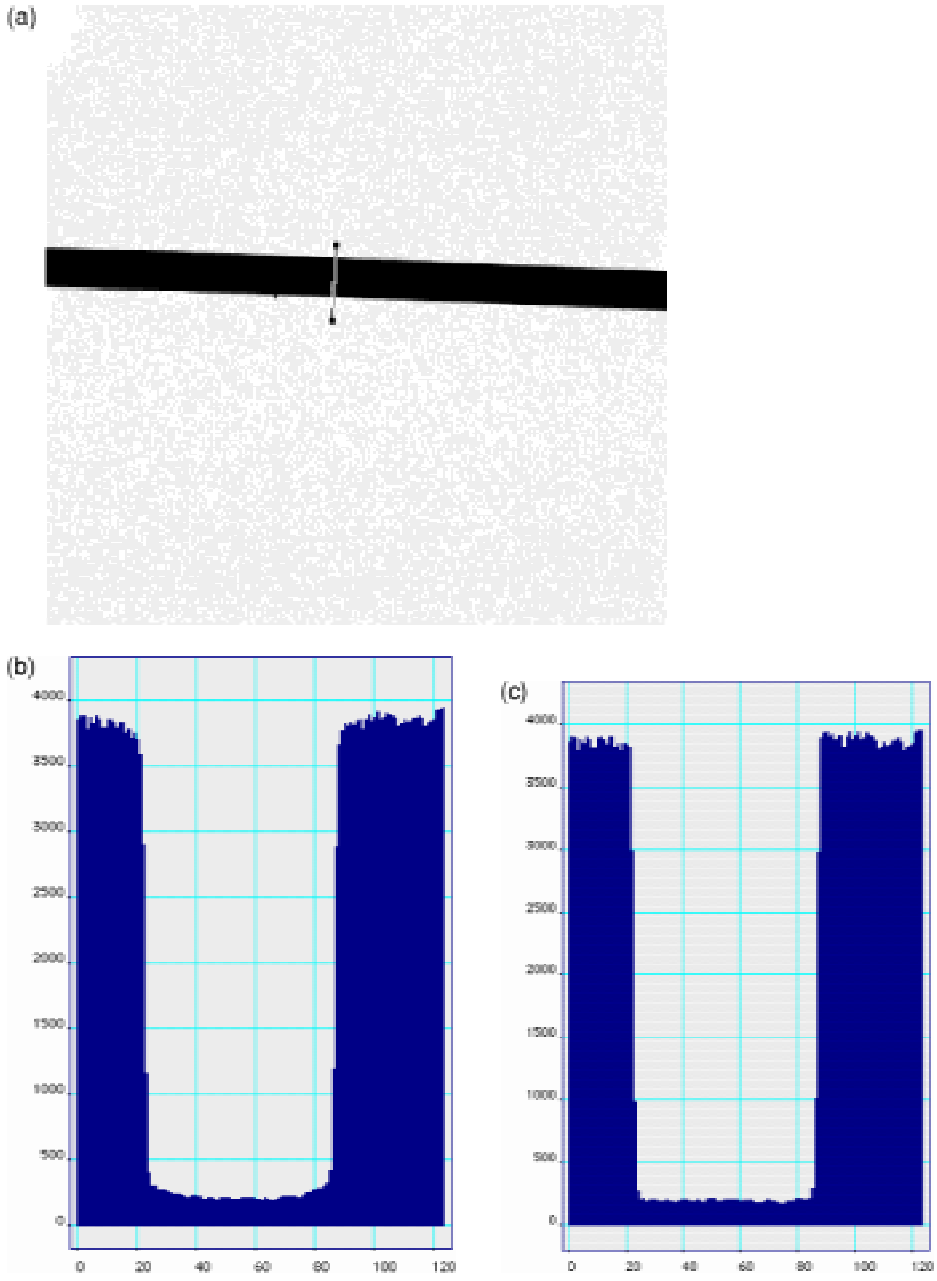

Figure 5. Image deconvolution example. Compare line scan profiles (**b**) and (**c**); it is clear that the deconvoluted image has a sharper edge. **a:** As recorded image. **b:** Line scan profile from image **a** (line scan position indicated in **a**). **c:** Line scan profile from deconvoluted image **a** (line scan indicated in **a**).

Figure 5 shows an example of a deconvoluted image. It is clear that the edge of the pattern is much sharper than the recorded one.

Refinement Convergence Tests

Our dynamical calculations typically include about 500 beams, both in the zero and higher order Laue zones. Beams selected for inclusion in the multiple scattering calculations were selected according to three criteria (Zuo & Weickenmeier, 1995): (1) proximity to the Ewald sphere; this is measured by $2KS_g$; (2) length of $g_{\max}$ vector; and (3) perturbation strength $\omega_{max}^{-1} = |U_g/2KS_h|_{\min}$.

The criteria $2KS_g$ is used as the weak-beam criterion. It selects the beams included in the diagonal matrix, whereas others are treated by Bethe's perturbation method. Here $g_{\max}$ is used as a cutoff parameter for high-order reflections. Because the width of the HOLZ lines falls off as g^{-3}, the intensity decreases by a factor of g^{-4}. As a result, the high-order reflections with $g > g_{\max}$ become localized, and their effects can be ignored. The third criteria $|U_g/2KS_h|_{\min}$ is called perturbation strength, and selects weak beams for

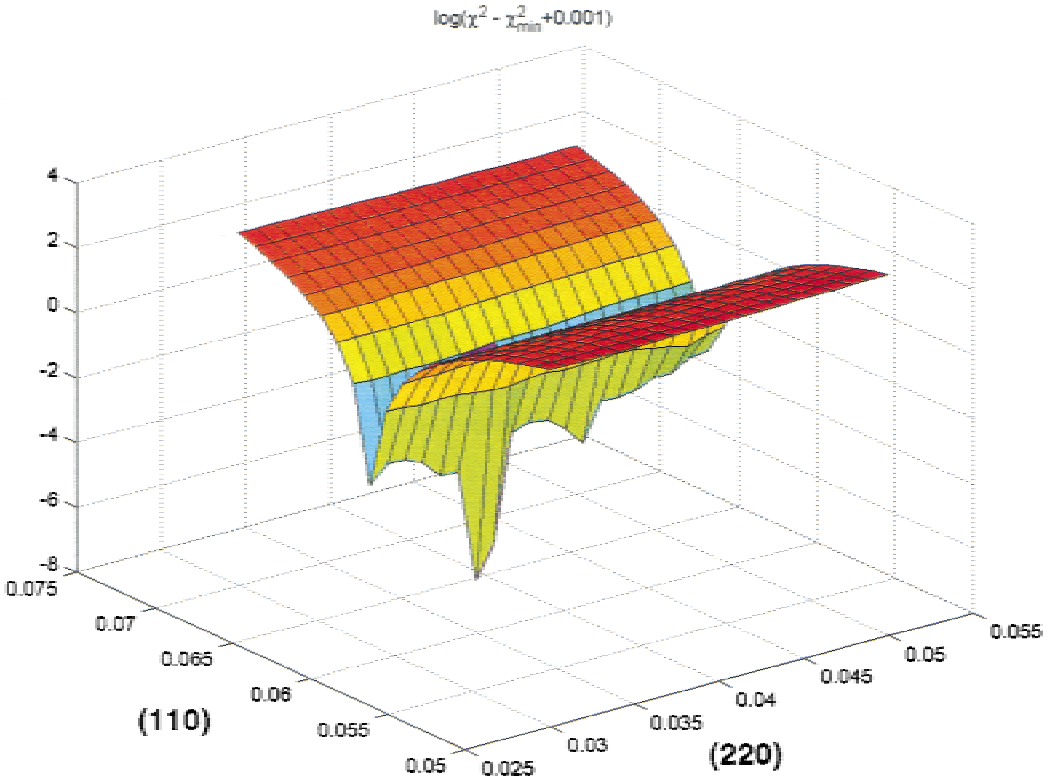

Figure 6. χ^2 versus structure factor (110) and (220) reflections of rutile crystal. It shows a deep global minimum. No other local minimum is found nearby.

perturbation treatment. The beams within the g_{max}, but with larger excitation error, will contribute to the beams and excitation error by perturbation. These criteria will be used to discard those beams with large excitation error. The beams selected in the refinement were tested for convergence by changing the above three criteria until the refined value converges. Normally the use of 3.0 (for $2KS_g$), 3.5 (for g_{max}), and 35 (for ω_{max}) were found to give a good refinement convergence for rutile crystals.

χ^2 Map

A preliminary refinement is used to obtain approximate values of thickness and orientation (assignment of K_t values to each pixel in the CBED pattern). The program then adjusts the following parameters for lowest χ^2: thickness, orientation, thermal background, the two structure-factor values being refined, and the two corresponding absorption coefficients. Absorption coefficients are taken from Bird and King (1990). The following parameters are not adjusted, and treated as known: all structure factors other than those under refinement, anisotropic, harmonic Debye–Waller factors (taken from Restori et al., 1987, who worked at the temperature of 100 K, were interpolated to our experimental temperature at 113 K), absorption coefficients other than the two being refined, accelerating voltage, cell parameters, and atom positions (obtained from Restori et al., 1987). The background beneath each disk (mainly phonon inelastic scattering, as plasmon-scattered electrons are removed by our energy filter) is assumed to be constant, and this constant, different for each CBED disk, is treated as a refinement parameter. Absorption parameters were found to need little adjustment, and to have a small effect. Experience shows that the simplex method is a very robust method to find the global minima (Zuo et al., 1998). To show that a global minima had been found in our refinement procedure, we did a χ^2 map versus the structure factors of the (110) and (220) reflections, for the case of (110) systematic refinement. This is shown in Figure 6. It clearly shows that near the global minima there is no other local minimum. This property ensures that the refinement program can find the real global minima. It is interesting to note that, for the (110) reflection, the minimum point is almost independent of the (220) reflection. This ensures the reliability of the

Table 2. QCBED Measurement on (110) and (220) Structure Factors of Rutile Crystal[a]

		χ^2	U(110)	Ua(110)	U(220)	Ua(220)
Crystal 1	(110) systematics	2.11	0.06349	0.00185	0.04322	0.00161
(111)-Zone-Axis	(tilt 8°)	1.28	0.06347	0.00169	0.04338	0.00130
		1.55	0.06348	0.00142	0.04350	0.00132
		1.56	0.06349	0.00151	0.04338	0.00183
	Average		0.06348	0.00162	0.04338	0.00152
Crystal 2	(110) systematics	1.17	0.06354	0.00128	0.04285	0.00127
(001)-Zone-Axis	(tilt 7°)	1.05	0.06360	0.00125	0.04300	0.00123
		1.87	0.06321	0.00140	0.04334	0.00142
		1.76	0.06331	0.00155	0.04291	0.00131
	Average		0.06341	0.00137	0.04303	0.00131
	(1−10) systematics	4.29	0.06388	0.00151	0.04304	0.00124
	(tilt 8°)	2.53	0.06341	0.00137	0.04298	0.00114
		2.47	0.06334	0.00136	0.04282	0.00123
		3.92	0.06380	0.00132	0.04324	0.00101
	Average		0.06361	0.00131	0.04308	0.00115
Average (12 data points)			0.0635	0.00146	0.0431	0.00133
Standard deviation (12 data points)			0.0002 (±0.3%)	0.00017	0.00024 (±0.56%)	0.00021
Standard error (12 data points)			0.00006 (±0.09%)	0.00005	0.00007 (±0.16%)	0.00006

[a]U(110) and U(220) are the elastic electron structure factor and Ua(110) and Ua(220) are the absorption part. Three data sets measured from (111) zone (110) systematics and (001) zone (110) systematics and (1−10) systematics. The experimental temperature is 113 K.

measured (110) reflection, and is one of factors that allows such high accuracy to be obtained by QCBED.

Error Analysis

The errors quoted in the tables were obtained using the following statistical formulas:

$$\text{Standard deviation: } \sigma = \sqrt{\frac{\sum_{j=1}^{N} (x_j - \bar{x})^2}{N-1}} \tag{8}$$

$$\text{Standard error: } \varepsilon = \frac{\sigma}{\sqrt{N}} \tag{9}$$

where N is the number of measurements. We note that σ is independent of the number of measurements; however, the error in the mean (the standard error) decreases with increasing number of measurements, as required.

QCBED Results for TiO_2 (110) Systematics

Table 2 shows the 12 data sets used for the consistency tests. These consist of CBED patterns from two different crystals, from which the same reflection was found in various different orientations and thicknesses. Each row in the table refers to a different thickness. The orientations were: (i) from (111) zone axis, tilted about 8° along the (110) systematics; (ii) from the (001) zone for (110) systematics (tilted 7°), and (iii) (1−10) systematics (tilted 8°). The results listed in Table 2 give the measured U(110), Ua(110), U(220), and Ua(220)

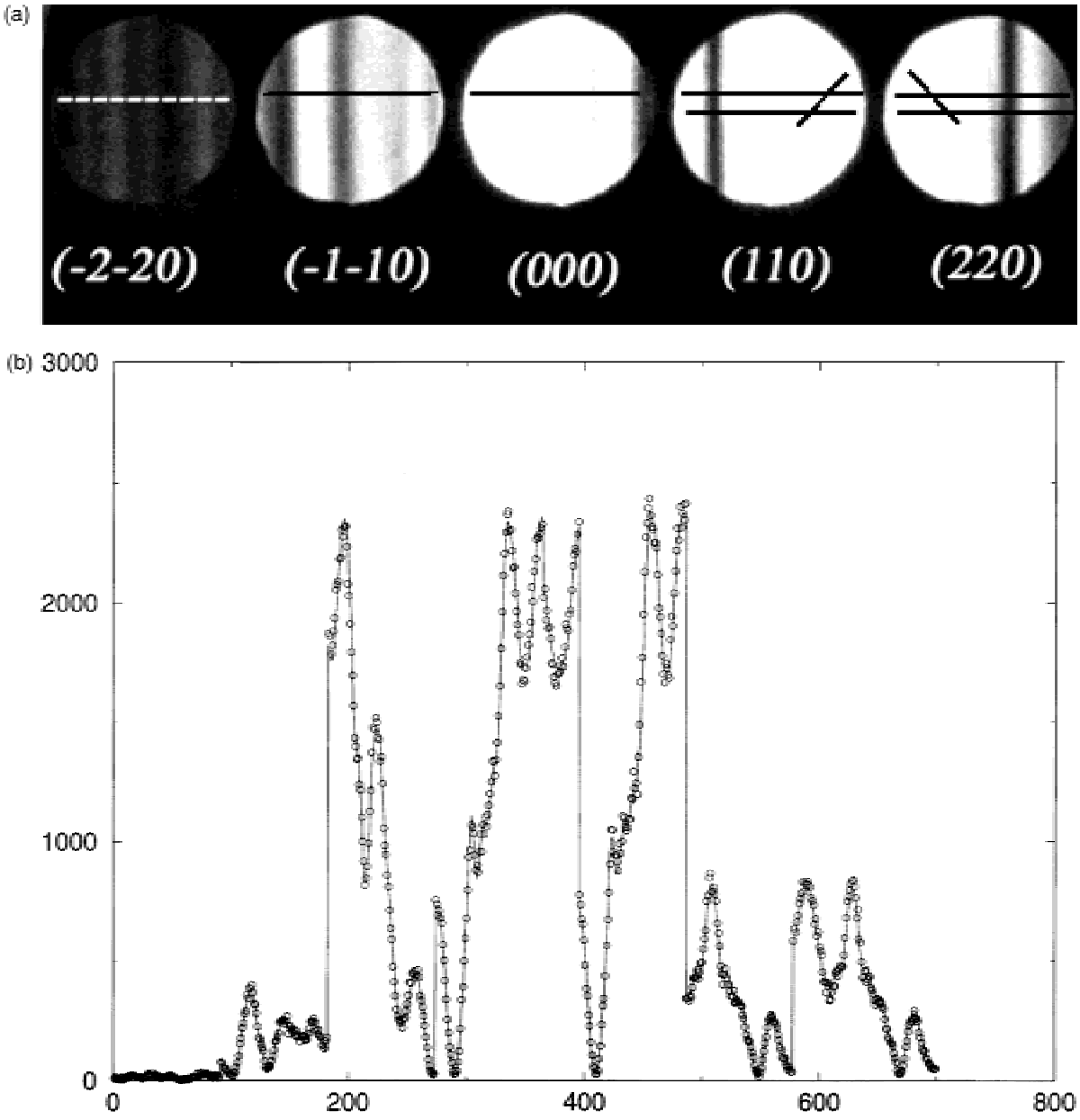

Figure 7. Example of the electron structure factor refinement for rutile crystal (110) and (220). **a:** Experimental recorded and deconvoluted CBED pattern. **b:** Best fit along the line indicated in **a**. The *x*-axis is pixel displayed sequentially and the *y*-axis in counts.

structure factors (in units of $Å^{-2}$), where Ua indicates an absorption parameter. Each measurement was done on a different diffraction pattern. The measurement was done by comparing the intensity of theoretical calculations and experimental intensities across the CBED disks (rocking curve), using the goodness of fit (χ^2) as the fitting criterion. Figure 7a,b gives an example of this fitting for the (110) and (220) reflections. About 500 beams are included in the calculations, not confined to the systematics row.

The different data sets are entirely consistent with each other. The overall standard deviation of the 12 values is 0.0002 and standard error (standard deviation of the mean) is $0.00006 = (0.0002/\sqrt{12})$. This is an error of about 0.09% in the measured U(110) and 0.16% in the measured U(220) electron structure factors.

Transforming these values into X-ray structure factors using the Mott formula (Spence & Zuo, 1992), using temperature factors for 110 K (Restori et al., 1987), the resulting

Table 3. Comparison of the X-Ray Structure Factors of (110) and (220) Reflections Measured by QCBED and Bragg X-Ray Diffraction[a]

		$F_x(110)$	$F_x(1-10)$	$y_{ext}(110)$	$F_x(220)$	$F_x(2\text{-}20)$	$y_{ext}(220)$
QCBED	Crystal 1 (111) zone	37.295	NA	NA	34.077	NA	NA
	Crystal 2 (001) zone	37.306	37.275	NA	34.240	34.266	NA
	Average	37.29 Standard deviation: (±0.032 or ±0.086%) Standard error: (±0.01 or ±0.026%)		NA	34.17 Standard deviation: (±0.15 or ±0.44%) Standard error: (±0.05 or ±0.14%)		NA
Gonschorek et al., 1982		38.89 (±0.17)	36.69 (±0.17)	NA	34.53 (±0.2)	34.36 (±0.2)	NA
Restori et al., 1987		37.78 (±0.18)	NA	0.864	34.48 (±0.26)	NA	0.945

[a]All the data here are assumed to be at the temperature of 100 K or converted to their 100 K values. (The X-ray structure factors are in units of electrons per cell.)

X-ray structure becomes $F_x(110) = 37.30 \pm 0.01$ (in units of electrons per unit cell), and $F_x(220) = 25.50 \pm 0.04$. The standard error (std. dev. of the mean) is 0.026% for $F_x(110)$ and 0.14% for $F_x(220)$. The accuracy is improved after transforming into X-ray structure factors owing to the Mott formula, as electron diffraction is more sensitive at smaller scattering angles.

Discussion

We have shown that the QCBED measurement method can give highly accurate and consistent data by comparing different measurements of equivalent reflections from different crystals in different orientations. This experiment on TiO_2 shows that the QCBED method is now a robust technique for low-order structure factor measurement if sufficiently sophisticated software is used and the detector is well characterized.

The accuracy obtained here on TiO_2 by QCBED is slightly better than the previously most accurate structure factor measurements, which were based on the X-ray single-crystal Pendellösung method, applied to silicon (Aldred & Hart, 1973). These two methods use a similar perfect-crystal Bloch-wave theory, and both require perfect crystals. That is the reason why they can give such accurate results. Compared with QCBED, however, the X-ray single crystal Pendellösung method requires large perfect crystals, and this has limited its application to the few semiconductor crystals that are available free of defects. The QCBED method, when combined with TEM imaging and the nanometer probe, can be applied to almost any kind of crystal. However, the QCBED method becomes less accurate than the X-ray method for large scattering angles, which are more sensitive to atomic positions and thermal effects than the bond-charge distribution.

A comparison with Bragg X-ray results is given in Table 3. The X-ray data sets are inconsistent with the same reflection from a different crystal, or equivalent reflections on the same crystal; thus the measurement depends on the crystal used. The difference between their measurements is much larger than their standard deviations, which indicates large systematic errors. These large systematic errors stem from the statistical description of the crystal used in the extinction correction. This may also be the main reason for the large difference between different groups. An accurate nonstatistical model is needed for improved extinction (multiple X-ray scattering) correction.

When combined with X-ray results for the higher order reflections, it should be possible to map out the charge density of TiO_2 accurately. According to band theory calculations, the oxygen $2s2p$ orbital hybridizes with titanium $4s4p3d$ orbitals to form bonding orbitals (Sorantin & Schwartz, 1991). The current measurements will make it

possible to test these band theory predictions, and to give accurate and reliable information on the role of *d* electrons in bonding in rutile.

Our experiments on rutile showed that QCBED is extremely sensitive to the quality of the TEM specimen. Rutile offers a good example of specimen problems with QCBED. We recommend that experimentalists carefully study the specimen before undertaking a QCBED analysis. First, crystals should be checked for point defects, strain, surface/interface relaxation, twin boundaries, and chemical inhomogeneity. All these inhomogeneous defects reduce the accuracy of the measured structure factors and increase the χ^2 factor. Second, check the crystal for nonstoichiometry. A deviation of chemical composition from the exact chemical formula would introduce large systematic errors in the structure factors that are fixed in the refinement procedures. Nonstoichiometry will produce diffuse scattering in point diffraction patterns, and may also be checked by X-ray microanalysis and by very accurate X-ray measurement of lattice constants. Nonstoichiometry will change the lattice constants. Thus it is possible that crystal constants could also be refined in order to calculate the exact chemical formula, and QCBED refinement could then be based on measured chemical ratios and crystals constants. Finally, crystals should be checked for any bulk or surface damage caused by the TEM specimen preparation procedures. The damage can be observed by high-resolution TEM imaging or from conventional electron diffraction patterns. We strongly recommend that experimentalists search for the best method for TEM specimen preparation for each material before undertaking a QCBED analysis. As this case showed, methods that produce a rough surface lead to a much poorer fit and less accurate values of the structure factors, as revealed by the error analysis.

Acknowledgments

This work was funded by DOE award DE-FG03-02ER45596 (J.C.H.S. PI). We thank Dr. M. O'Keeffe for discussions.

References

Aldred, P.J.E. & Hart, M. (1973). Electron-distribution in silicon 1. Experiment. *Proc Roy Soc Lond A* **332**, 223–238.

Bird, D.M. & King, Q.A. (1990). Absorptive form-factors for high-energy electron diffraction. *Acta Cryst A* **46**, 202–208.

Gonschorek, W. (1982). X-ray charge-density study of rutile (TiO_2). *Zeitschrift Fur Kristallographie* **169**, 187–203.

Goodman, P. (1974). Role of upper-layer interactions in electron-diffraction symmetries. *Nature* **251**, 698–701.

Jiang, B., Zuo, J.M., Chen, Q. & Spence, J.C.H. (2002). Orbital ordering in $LaMnO_3$: Estimates of structure factors and comparison of measurement methods. *Acta Cryst A* **58**, 4–11.

Lippmann, T. & Schneider, J.R. (2000). Topological analyses of cuprite, Cu_2O, using high-energy synchrotron-radiation data. *J Appl Cryst* **33**, 156–167.

Restori, R., Schwarzenbach, D. & Schneider, J.R. (1987). Charge density in rutile, TiO_2. *Acta Cryst B* **43**, 251–257.

Rose, H. & Krahl, D. (1995). Electron optics of imaging filters. In *Energy Filtering Transmission Electron Microscopy*, Reimer, L. (Ed.), pp. 43–149. Berlin: Springer.

Snyder, D.L., Hammond, A.M. & White, R.L. (1993). Image recovery from data acquired with a charge-coupled-device camera. *J Opt Soc Am A* **10**, 1014–1023.

Sorantin, P.I. & Schwartz, K. (1991). Chemical bonding in rutile-type compounds. *Inorg Chem* **31**, 567–576.

Spence, J.C.H. & Zuo, J.M. (1992). *Electron Microdiffraction*. New York: Plenum Press.

Zuo, J.M. (1996). Electron detection characteristics of slow-scan CCD camera. *Ultramicroscopy* **66**, 21–33.

Zuo, J.M. (1998). Quantitative convergent beam electron diffraction. *Mat Trans JIM* **39**, 938–946.

Zuo, J.M. (2000). Electron detection characteristics of a slow-scan CCD camera, imaging plates and film, and electron image restoration. *Microsc Res Technol* **49**, 245–268.

Zuo, J.M., Kim, M., O'Keeffe, M. & Spence, J.C.H. (1999). Direct observation of *d* orbital holes and Cu-Cu bonding in Cu_2O. *Nature* **401**, 49–52.

Zuo, J.M., O'Keeffe, M., Kim, M. & Spence, J. (2000). On closed-shell interactions, polar covalences, *d* shell moles, and direct images of orbitals: The case of cuprite—Response to the essay by S.G. Wang and W. H. E. Schwarz. *Angew Chem Int Ed* **39**, 3791–3794.

Zuo, J.M., O'Keeffe, M., Rez, P. & Spence, J. (1997). Charge density of MgO: Implications of precise new measurements for theory. *Phys Rev Lett* **78**, 4777–4780.

Zuo, J.M. & Spence, J.C.H. (1993). Measurement of individual structure-factors phases with 10th-degree accuracy—The 002 reflection in BeO studied by electron and X-ray-diffraction. *Acta Cryst A* **49**, 422–429.

Zuo, J.M. & Weickenmeier, A. (1995). On the beam selection and convergence in the Bloch-wave method. *Ultramicroscopy* **57**, 375–383.

Paper 3

Retrieval of anisotropic displacement parameters in Mg from convergent beam electron diffraction

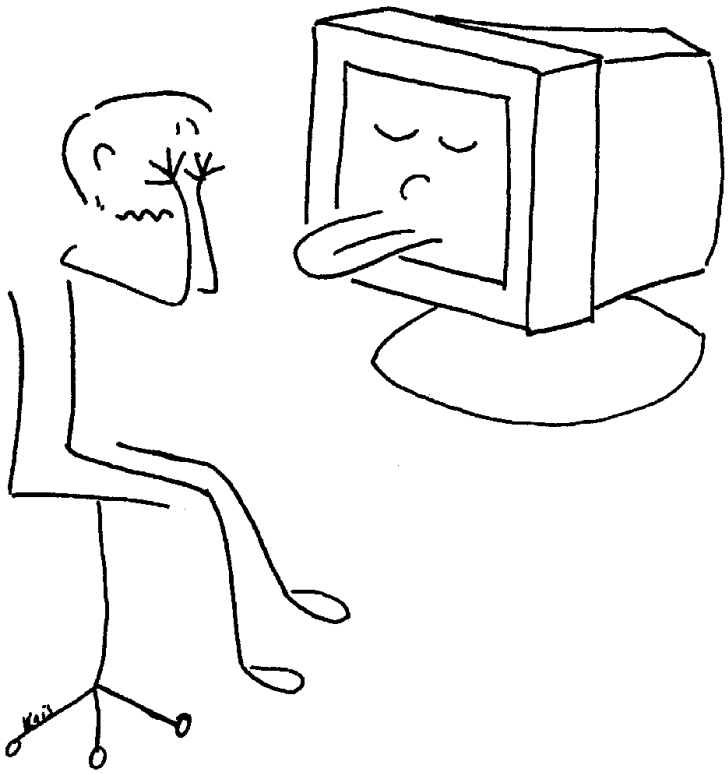

Retrieval of anisotropic displacement parameters in Mg from convergent beam electron diffraction experiments

J. Friis[†], K. Marthinsen[‡] and R. Holmestad[†]
[†]Department of Physics, Norwegian University of Science and Technology (NTNU), 7491 Trondheim, Norway
[‡]Department of Materials Technology, Norwegian University of Science and Technology (NTNU), 7491 Trondheim, Norway

Abstract. We present an accurate Wilson plot-like method, based on convergent beam electron diffraction, for measuring the anisotropic displacement parameters in magnesium, and compare it with the method proposed by Saunders *et al.* A generalization of this method to isotropic crystals with more than one type of atoms is also discussed.

1. Introduction

With quantitative convergent beam electron diffraction (QCBED) [1, 2] it is possible to very accurately measure the low order structure factors in small-unit cell crystals. This technique is based on a pixel to pixel comparison between an experimental CBED pattern and a Bloch-wave simulation. The input parameters (such as structure factors, beam direction, etc.) in the Bloch-wave simulation are refined until the best fit is obtained.

In structure factors measured by QCBED, the largest source of errors comes from uncertainty in the thermal displacement parameters (DPs). Even though the DPs might be known as a function of temperature, either from phonon calculations, or from X-ray or neutron measurements, the exact sample temperature is unknown. Several methods have therefore been proposed for measuring the DPs directly by electron diffraction [3-7]. Most of these methods, except [7], require separate experiments for the determination of DPs and structure factors. The same experimental conditions, e.g. sample temperature, can therefore not be guaranteed. We will here investigate a Wilson plot-like method based on the values of the refined electron structure factors, and compare it with the method proposed by [7].

2. CBED experiment and refinement

The experiments were performed using a 120 kV LEO 912B TEM with an in-column Ω-filter and a Gatan CCD camera. The systematic row orientation was used and the sample was cooled to liquid nitrogen temperature. Eleven low order structure factors, listed in Table 1, were measured and refined with the EXTAL program [2]. For Mg the DPs have been measured at different temperatures by neutron diffraction [8]. Hence, good initial estimates of the anisotropic DPs of $\langle u_1^2 \rangle = 0.0076$ Å^2 (**a**-direction, parallel to 2-fold axis) and $\langle u_3^2 \rangle = 0.0085$ Å^2 (**c**-direction, parallel to $\bar{6}$-fold axis) at the experimental temperature (around 110 K) have been used in the refinements.

Table 1. Refinement results. The scattering angles s are in units of Å^{-1} and the electron structure factors $U_{\mathbf{g}}$ are in units of 10^{-4} Å^{-2}.

hkl	1 0 0	0 0 2	1 0 1	1 0 2	1 1 0	1 0 3	2 0 0	2 1 0	0 0 4	2 0 4	2 2 0
s	0.181	0.193	0.205	0.264	0.313	0.341	0.361	0.385	0.478	0.528	0.626
$U_{\mathbf{g}}$	184.5	346.9	279.6	115.3	185.8	143.8	77.21	141.0	52.42	44.71	67.0
	±0.7	±0.4	±0.9	±0.5	±0.2	±0.3	±0.15	±0.3	±0.15	±0.16	±0.5

The measured electron structure factors $U_{\mathbf{g}}$ (Fourier coefficients of the crystal potential) are converted to X-ray structure factors $F_{\mathbf{g}}$ (Fourier coefficients of the electron density) with the Mott-Bethe formula [1]

$$F_{\mathbf{g}} = \sum_i Z_i T_{i,\mathbf{g}} \, \mathrm{e}^{-2\pi i \mathbf{g}\cdot\mathbf{r}_i} - \frac{8\pi^2 \varepsilon_0 h^2 \Omega s^2}{\gamma m_e e^2} U_{\mathbf{g}}. \tag{1}$$

The sum goes over all atoms, where Z_i and $T_{i,\mathbf{g}}$ are the atomic number and temperature factor of atom i, respectively. Ω is the unit cell volume, $s = \sin\theta/\lambda$ the scattering angle and $\gamma = 1 + E_0/(m_e c^2)$ a relativistic correction, with E_0 being the acceleration voltage of the microscope.

3. Determination of DPs using the method proposed by Saunders *et al.*

A strategy for determination of DPs by comparing the refined structure factors with calculations was proposed by [7]. In short, each refinement is performed for a range of fixed DP values, where the same DPs are used for conversion to X-ray structure factors. If the order of the structure factor is sufficiently high, so that bonding effects can be neglected, the X-ray structure factor obtained with the correct DPs should equal the calculated value from an independent atom model (IAM) [9].

In Fig. 1a this method is applied to the (204) structure factor ($\sin\theta/\lambda = 0.528$ Å^{-1}) of Mg. The neutron diffraction measurement [8] is used to relate the two anisotropic DPs for Mg to each other and to assign them to a temperature. The refined structure factors, converted to X-ray values intersect the IAM values at 102 K, corresponding to $\langle u_1^2 \rangle = 0.0074$ Å^2 and $\langle u_3^2 \rangle = 0.0082$ Å^2.

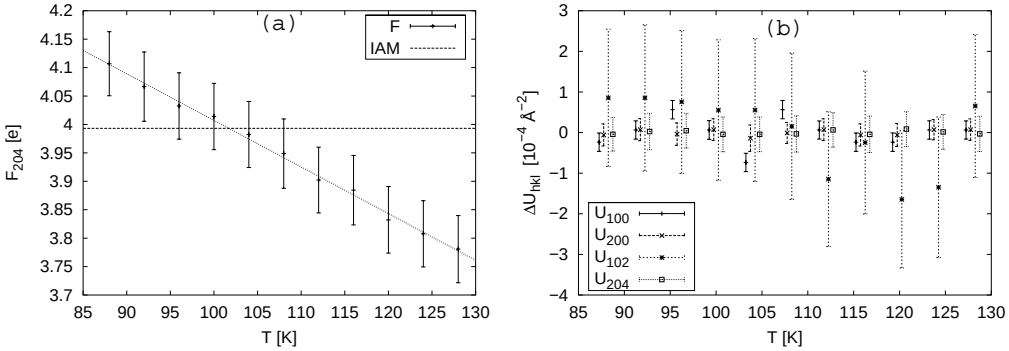

Figure 1. (a) The refined and converted (204) structure factor as a function of the temperature used in the refinement. The dashed line represent the IAM value. (b) The difference between electron structure factors and their mean value as a function of the temperature used in the refinement.

4. Wilson-like method for determination of DPs

The refinement procedure for low order structure factors itself is not very sensitive to the DPs, since they mainly affect the non-refined high order structure factors responsible for HOLZ-lines. This is demonstrated in Fig. 1b, where four structure factors are refined for a range of (fixed) temperatures. No dependence between $U_{\mathbf{g}}$ and the temperature is observed. However, one should keep in mind that this result is obtained in a systematic row orientation when strong HOLZ-lines are avoided. The case might be different in the zone-axis orientation used in [7]. The conversion to X-ray structure factors is, on the other hand, sensitive to the DPs because of the atomic temperature factors $T_{i,g}$ in Eq. (1). The method for determination of DPs presented here is purely based on this fact.

In the harmonic approximation the atomic temperature factor for Mg is

$$T_{\mathbf{g}} = \exp[-(h^2+hk+k^2)P - l^2 Q] \tag{2}$$

where

$$P = 2\pi^2 \frac{4}{3a^2}\langle u_1^2\rangle \quad \text{and} \quad Q = 2\pi^2 \frac{1}{c^2}\langle u_3^2\rangle. \tag{3}$$

Since Mg only has one atom species, the X-ray structure factors can be written as $F_{\mathbf{g}} = f_{\mathbf{g}} T_{\mathbf{g}} C_{\mathbf{g}}$, where $f_{\mathbf{g}}$ are static lattice scattering factors and $C_{\mathbf{g}} = \sum_i \exp(2\pi i \mathbf{g}\cdot\mathbf{r}_i)$. This, together with Eq. (1) and (2), gives

$$-\ln T_{\mathbf{g}} = -\ln\left[\frac{8\pi^2\varepsilon_0 h^2 \Omega s^2 U_{\mathbf{g}}}{\gamma m_e e^2 C_{\mathbf{g}}(Z-f_{\mathbf{g}})}\right] = \left(h^2+hk+k^2\right)P + l^2 Q. \tag{4}$$

Given $f_{\mathbf{g}}$, the left hand side of Eq. (4) can be calculated. Hence P and Q can easily be obtained by least square fitting. In Fig. 2 we have plotted the left hand side of Eq. (4) against the right hand side for the fitted values of P and Q. We do therefore expect the points to follow a straight line with a slope of 1. We have used $f_{\mathbf{g}}$ from both Dirac-Fock [10] and density functional theory (DFT) [11] calculations. The latter includes bonding effects and brings even the low order points nicely onto the line (Fig. 2b). Using the DFT values this gives $\langle u_1^2\rangle = 0.00777(4)$ Å^2 and $\langle u_3^2\rangle = 0.0082(1)$ Å^2. These values are so close to the initial values used that new refinements were not performed. However, if the initial DPs were less accurate, one would have to redo the structure factor refinement with the new DPs until convergence is achieved.

This method benefits from the large number (eleven) of measured structure factors. Usually one does not measure that many structure factors with the CBED technique. In

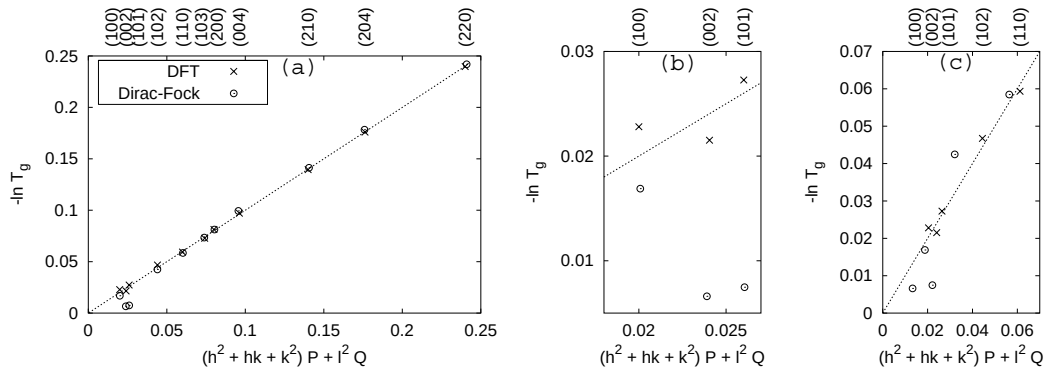

Figure 2. Wilson-like plot for low order data. The static lattice reference scattering factors are taken from both DFT (×) and Dirac-Fock (∘) calculations. The slope of the line is 1. (b) shows an enlargement around the three first structure factors in (a), where the disagreement between the two models is pronounced. In (c) the same fit is performed using only the five lowest order structure factors.

Fig. 2c we have therefore redone the fit by only considering the five lowest order structure factors. The fitted DPs now become $\langle u_1^2 \rangle = 0.0079(3)$ Å^2 and $\langle u_3^2 \rangle = 0.0082(7)$ Å^2. In this case it is really essential to consider bonding effects in the static lattice reference scattering factors $f_{\mathbf{g}}$. If even fewer structure factors are measured, it is probably sensible to constrain $\langle u_3^2 \rangle$ to $\langle u_1^2 \rangle$ or use an isotropic model.

This method can be generalized to crystals with more than one type of atoms, in the case where only one independent DP needs to be determined per atom type. This is the case for isotropic DPs, which we will consider here. We can then write $T_i = \exp(-B_i s^2)$, where the B_i are known as Debye-Waller factors. Eq. (1) can now be rewritten as

$$U_{\mathbf{g}} = \frac{\gamma m_e e^2}{8\pi^2 \varepsilon_0 h^2 \Omega s^2} \sum_i \left(Z_i - f_{\mathbf{g},i} \right) \mathrm{e}^{-2\pi i \mathbf{g}\cdot\mathbf{r}_i} \, \mathrm{e}^{-B_i s^2} \tag{5}$$

resulting in a set of equations (one for each **g**) each containing a sum of exponentials in $-B_i s^2$. These exponents can be determined with non-linear fitting, giving the Debye-Waller factors.

5. Discussion and conclusion

The very good fit in Fig. 2 shows that there is enough information in the CBED data to accurately determine DPs.

We have here compared two different methods for determining the DPs in Mg. The method proposed here differs from the one in [7] in that all structure factor refinements are initially carried out only once with assumed DPs. As seen from Fig. 1b, errors in the DPs will not affect the refined structure factors very much when a HOLZ-line free region is used in the refinement. The determination of DPs in the method proposed here is purely based on the Mott-Bethe formula, and involves all measured structure factors via least square fitting. Another improvement, is that DFT, instead an IAM, is used in the calculations of static lattice reference scattering factors. A minor drawback of this is that a systematic error in the DFT model will bias the experimental structure factors towards the DFT-values, making them less appropriate for testing the DFT model [12]. Nevertheless, we believe that the DPs obtained by this method are the most accurate as long as the number of refined structure factors exceeds the number of fitted DPs with a factor of at least two or three.

Acknowledgments

Helpful discussions with B Jiang and J C H Spence and fundings from the Research Council of Norway (project 135270/410) are gratefully acknowledged.

References

[1] Spence J C H and Zuo J M 1992 *Electron Microdiffraction* (Plenum Press, New York)
[2] Zuo J M 1999 *Microscopy Research and Technique* 46 220–233
[3] Holmestad R, Weickenmeier A L, Zuo J M, Spence J C H, and Horita Z 1993 *Inst. Phys. Conf. Ser.* 138 141–144
[4] Menon E S K and Fox A G 1998 *Philos. Mag. A*77 577–592
[5] Midgley P A, Sleight M E, Saunders M and Vincent R 1998 *Ultramicroscopy* 75 61–67
[6] Nüchter W, Weickenmeier A L and Mayer J 1998 *Acta Cryst. A*54 147–157
[7] Saunders M, Fox A G and Midgley P A 1999 *Acta Cryst. A*55 480–488
[8] Iversen B B, Nielsen S K and Larsen F K 1995 *Philos. Mag. A*72 1357–1380
[9] Doyle P A and Turner P S 1968 *Acta Cryst. A*24 390–397
[10] Su Z and Coppens P 1997 *Acta Cryst. A*53 749–762
[11] Blaha P, Schwarz K, Madsen G K H, Kvasnicka D, and Luitz J 2001 *WIEN2k*
[12] Friis J, Madsen G K H, Larsen F K, Jiang B, Marthinsen K, and Holmestad R 2003 Submitted

Paper 4

Magnesium: Comparison of Density Functional Theory Calculations with Electron and X-ray Diffraction Experiments

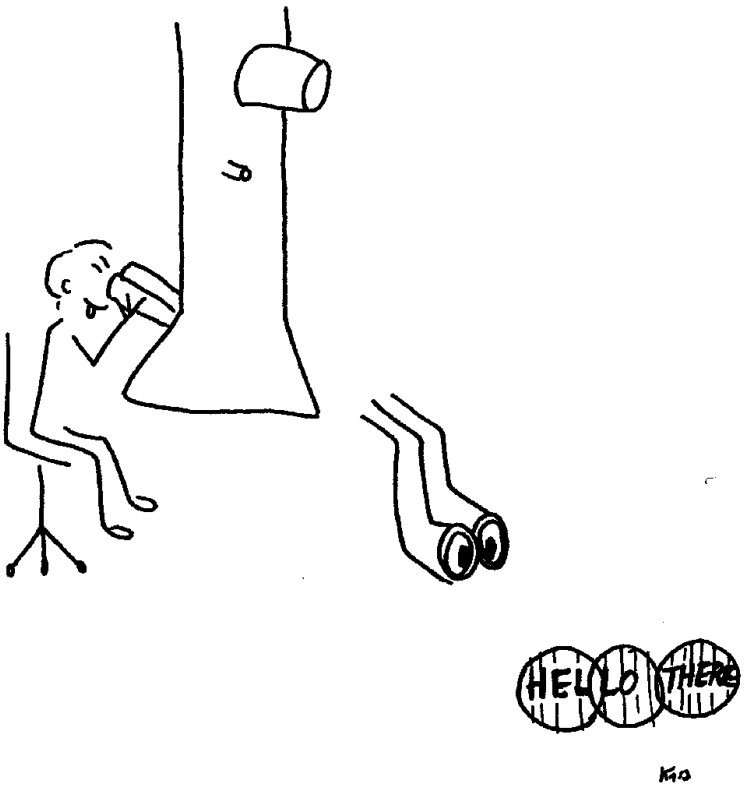

Magnesium: Comparison of density functional theory calculations with electron and x-ray diffraction experiments

J. Friis[a)]
Department of Physics, Norwegian University of Science and Technology, Norway

G. K. H. Madsen and F. K. Larsen
Department of Chemistry, University of Aarhus, DK-8000 Århus C, Denmark

B. Jiang
Department of Physics and Astronomy, Arizona State University, Arizona

K. Marthinsen
Department of Materials Technology, Norwegian University of Science and Technology, Norway

R. Holmestad
Department of Physics, Norwegian University of Science and Technology, Norway

(Received 25 July 2003; accepted 8 September 2003)

Accurate experimental structure factors for Mg have been measured and compared with density functional theory (DFT) to test some commonly used functionals and self-interaction correction (SIC) schemes. Low order structure factors, free of extinction and on absolute scale, were measured accurately by quantitative convergent beam electron diffraction. In addition, a complete set of structure factors up to $\sin\theta/\lambda = 1.6$ Å^{-1} was measured by x-ray diffraction at 10 K. The DFT calculations were performed using the full potential linearized augmented plane wave method. It was found that the agreement with experiment increases when going from the local density approximation (LDA) to the generalized gradient approximation (GGA) of Perdew, Burke, and Ernzerhofer and further to the GGA of Engel and Vosko. Applying the SIC of Perdew and Zunger to the core states for LDA does not improve the agreement with theory, while applying the SIC of Lundin and Eriksson results in a significantly improved agreement. This implies that the main source of error in the LDA functional comes from the description of the core densities. Using the functional which agrees best with experiment, a non-nuclear maximum is established in the calculated electron density of beryllium but not of magnesium. © *2003 American Institute of Physics.* [DOI: 10.1063/1.1622656]

I. INTRODUCTION

In density functional theory (DFT) new functionals are mainly tested against energies[1] or energy-derived properties such as structure or bulk moduli.[2,3] Although the electron density is the key quantity in DFT, direct testing against experimentally measured structure factors is relatively rare. One of the reasons for this is that a very high precision and accuracy of the experimental structure factors are needed to discriminate between the small discrepancies in the results of modern computational methods. Figure 1(b) shows furthermore that for a small unit cell system such as magnesium, the scattering of the valence electron density has dropped to a very low value already at the lowest symmetry allowed reflection ($\sin\theta/\lambda = 0.181$ Å^{-1}) of magnesium. Exactly these reflections are difficult to measure with x-ray diffraction due to extinction. The extinction effects can be taken into account by using the Pendellösung method and interpretation by dynamical theory, but this requires a perfect crystalline sample which has limited the method to a few crystals, such as Si (Ref. 4) and diamond.[5] Another problem is if the computational method is compromised by the use of limited basis sets or the pseudopotential approximation. In the present work, we overcome these two problems by the use of convergent beam electron diffraction (CBED) to measure the low order reflections and the full potential linearized augmented plane wave (LAPW) method[6–8] in the DFT calculations.

In a transmission electron microscope (TEM) it is possible for many crystals to focus the incident electron beam onto a region much smaller than one mosaic block. This technique produces a set of rocking curves for every diffracted beam simultaneously. The small probe and large amount of information, combined with the strong interaction between the fast incident electrons and the crystal potential, make electron diffraction sensitive to the strong, low order structure factors. It is therefore well suited for quantitative work.[9] The LAPW method has the clear advantage that the basis set quality is essentially controlled by only one parameter, namely the plane wave cutoff.[6–8] When basis set convergence is achieved, any deviation from experiment must be purely due to inadequacies of the applied exchange-correlation potential within the DFT.

Some tests of density functionals with systematic comparisons between accurate calculations and measured struc-

a)Electronic mail: jesper.friis@phys.ntnu.no

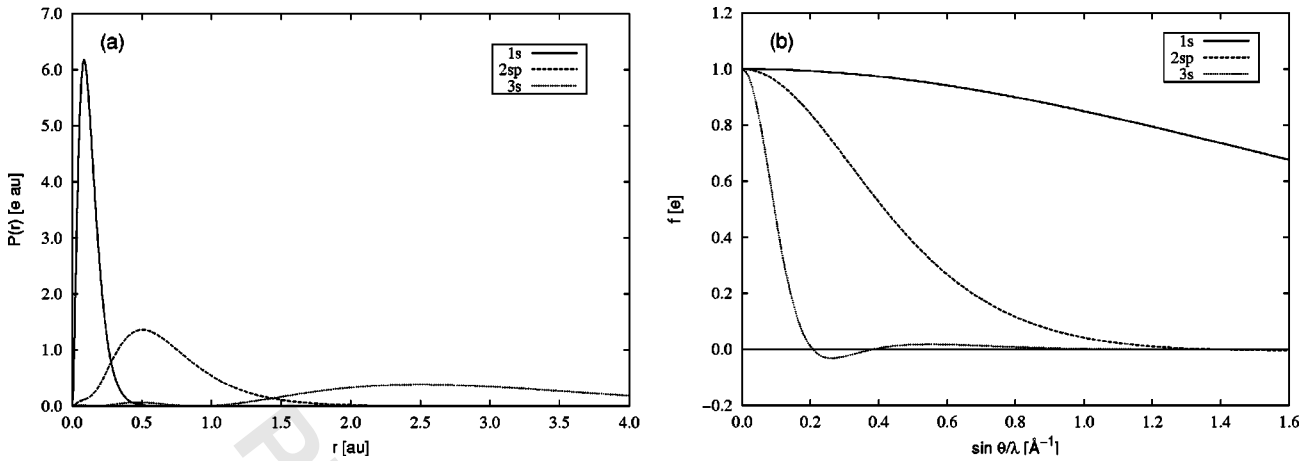

FIG. 1. (a) Radial density probability function $P(r)=4\pi\rho(r)r^2$ of different shells of atomic magnesium, normalized so that each shell contains one electron. Full line: $1s$-density. Broken line: $2sp$-density. Dotted line: $3s$-density. (b) Fourier transform of $P(r)$.

ture factors have been carried out for silicon,[10] germanium,[11] and beryllium.[12] Other tests against electron density derived properties, such as hyper fine fields[13] or electric field gradients,[14] have also appeared. Both these studies[13,14] highlight a well-known inadequacy of most density functionals, namely that the ground-state energy is not self-interaction-free. This is expected to be mainly a problem for core electrons or for highly contracted d- or f shells. The self-interaction correction (SIC) of Perdew and Zunger (PZ)[15] has been very successful in overcoming some of the shortcomings of DFT in the treatment of strongly correlated materials,[16] but the tests of the PZ-SIC have mainly been based on total energy derived properties.[16] Lundin and Eriksson (LE)[17] pointed out that the PZ-SIC is not fully self-interaction-free and constructed the LE-SIC so that it is fully self-interaction-free by construction.[17] The results of Novák *et al.*[13] showed that the LE-SIC is superior to pure local density approximation (LDA) and the PZ-SIC in predicting the hyperfine fields for the $3d$ ferromagnets. This could indicate that the LE-SIC provides a better electron density than the more common functionals. In this work we have therefore tested the effect of applying a SIC to the core electrons of Mg.

Simple hcp metals show a wide range of the c/a ratios. For Be this value is abnormally low, $c/a=1.5684$, in contrast to the almost ideal value of $c/a=1.6224$ for Mg. This lead to an interest in determining the charge density distribution of these metallic structures[18,19] and subsequently a controversy over the possible existence of a non-nuclear maximum (NNM) in the total charge density, in particular for beryllium.[12,20–24] Recently, the electron density in Be, Mg, Na, and Li was studied with the LAPW method,[12] and it was found that at ambient pressure the electron density in hcp Be and bcc Li exhibits NNM. While F centers have been found to manifest themselves as quite large and well defined NNM,[25–27] the NNM in simple metals are extremely small and we will further investigate their existence by establishing the functional that gives the best agreement with the experimental structure factors.

II. EXPERIMENTAL STRUCTURE FACTORS

A. Sample preparation

Both a single crystal magnesium block grown by zone refinement at the University of Aarhus and a 0.15 mm thick 99.8% assay Mg ribbon from Alfa Alsar were used for the TEM sample preparation. The former was cut to 3 mm disks with normal in the [110] direction and the latter to disks with normal in the [001] direction. As a first try, the samples were prepared with a precision ion polishing system, which however left a too uneven surface, even for incident ion beam angles as low as 4°. The rest of the samples were therefore prepared by dimpling to around 100 μm thickness and then electropolishing in a solution of 5% HNO_3, and 93.5% methanol at 10 V and 0.5 A at room temperature. As soon as a hole was created, the samples were cleaned with methanol and directly brought into the vacuum in the TEM to avoid oxidation.

In the zone-refinement preparation of a magnesium single crystal, a bar of the metal (more than 99.5 wt % Mg) of 15 mm diameter and 60 mm length filled the borehole in a BN crucible and was induction heated by a single loop coil in a high-temperature furnace. In order to prevent magnesium from reacting with oxygen or nitrogen, the furnace chamber was carefully fluxed with helium before heating the magnesium bar, and during the crystal synthesis, the helium pressure was maintained at 0.3 MPa in the oven. The pass velocity through the coil was 5 mm h^{-1}. The five-pass zone-refined bar developed into a few single crystals. The above-mentioned magnesium block used for the TEM sample preparation was cut from a single-crystal grain. During the zone refinement a little magnesium sublimed and condensed at the top of the BN container in the form of almost spherical single crystals.

One crystal with diameter of 0.25 mm and with well-developed {001} and {111} facets was selected for x-ray diffraction data collection.

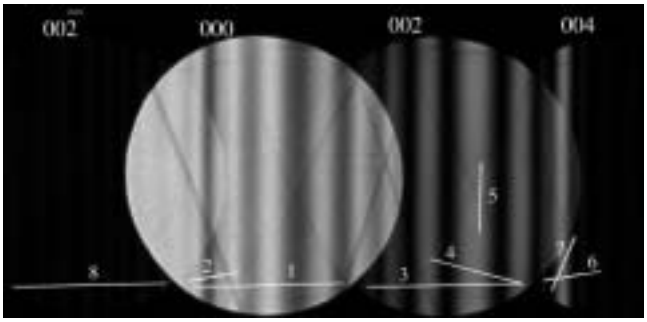

FIG. 2. CBED pattern of the (002) systematic row in magnesium. Eight rocking curves sensitive to the refined parameters are marked on the pattern.

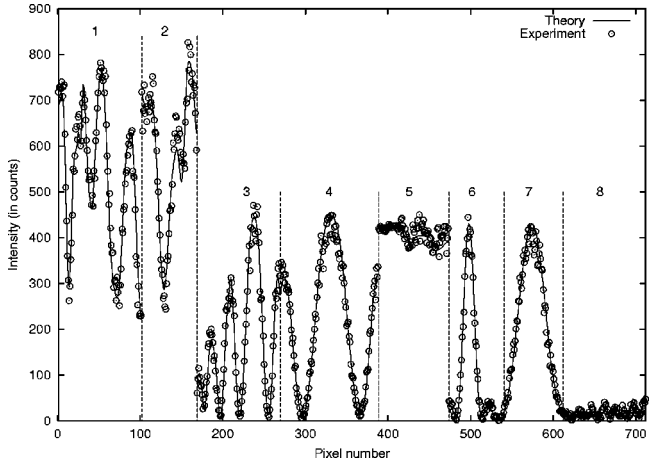

FIG. 3. Best fit between experimental (points) and theoretically calculated (lines) intensities after structure factor refinement of the (002) systematic row CBED pattern shown in Fig. 2. Seven hundred and twelve pixels along the rocking curves drawn on Fig. 2 were included in the refinement. Pixels belonging to different rocking curves are separated by vertical lines. The χ^2 for this particular refinement is 1.47.

B. Electron diffraction

1. The CBED experiment

The CBED experiment was performed in a LEO 912B transmission electron microscope, at Arizona State University. This microscope operates at 120 kV and is equipped with an in-column Ω-filter and a Gatan MSC CCD (14 bit dynamic range) camera. To reduce thermal diffuse scattering and to avoid contamination during the experiment, the sample was kept at liquid nitrogen temperature using a Gatan cooling double-tilt holder. The energy window of the Ω-filter was 5–10 eV, allowing only elastically and thermal diffuse scattered electrons to contribute.

The CBED patterns were recorded in a systematic row diffraction orientation in which the intensities are very sensitive to normally one or two low order structure factors, for which the Bragg condition is satisfied. Moreover, when selecting orientation, we also tried to reduce the number of high order Laue zone lines, since they depend on high order structure factors that are sensitive to the unknown sample temperature. An example of this geometry is shown in Fig. 2 for the (002) systematic row. The intensities along the rocking curves 3 to 7 are very sensitive to the (002) and (004) structure factors. The other rocking curves are included for increased sensitivity to sample thickness (curves 1,3,8), orientation (curves 2,5), and absorption (curve 1).

The CCD camera was well characterized,[28] allowing to compensate for nonlinearity and point spreading by postprocessing the recorded CBED patterns.

2. Structure factor refinement

The pixel intensities along the rocking curves are calculated with the Bloch wave method.[9,29] In short, the Schrödinger equation is solved in reciprocal space for the high energy beam electrons passing through the sample, for which exchange and correlation effects can be neglected.[30] The crystal potential is conveniently expanded into electron structure factors $U_{\mathbf{g}}=(2me/h^2)V_{\mathbf{g}}$, where $V_{\mathbf{g}}$ are the Fourier coefficients of the potential and m and e are the electron mass and charge, respectively. The electron structure factors are determined by a refinement procedure, minimizing

$$\chi^2=\frac{1}{n-p-1}\sum_i \frac{1}{\sigma_i^2}(I_i^{\mathrm{exp}}-cI_i^{\mathrm{theo}}-I_i^{\mathrm{bgr}})^2, \tag{1}$$

where the sum runs over the number of pixels n, and p denotes the number of refined parameters. I_i^{exp}, I_i^{theo}, and I_i^{bgr} are the experimental, theoretical, and background intensities of pixel i, respectively. σ_i is the standard deviation of I_i^{exp} and c is a scaling of the calculated intensities. Only structure factors corresponding to the normally one or two strongly excited Bragg reflections are refined. The structure factors have a refined complex component $U'_{\mathbf{g}}$ accounting for absorption, which mainly comes from the thermal diffuse scattered electrons that cannot be removed by the energy filter. In addition to the structure factors, the sample thickness, the electron beam orientation, the scaling c, and the background I_i^{bgr} (assumed constant for each diffraction disk) are also refined.

Lattice and anisotropic displacement parameters (ADPs) were not refined, but obtained by interpolation from earlier neutron diffraction experiments.[31] This was done by assuming that the actual temperature of the sample under the beam was 5 K higher than the readout temperature from the sample holder,[32] which variated between 107 and 112 K. Figure 3 shows the best fit after refinement of the rocking curves in Fig. 2.

In total, 36 refinements of 7 systematic rows were performed. The resulting structure factors are averaged and listed in Table I. The average and variance of the structure factors are calculated by

$$U_{\mathbf{g}}=\sum_i w_i U_{\mathbf{g}i}, \tag{2}$$

$$\sigma^2(U_{\mathbf{g}})=\sum_i w_{\mathbf{g}i}^2 s_{\mathbf{g}i}^2+\sum_i w_{\mathbf{g}i}(U_{\mathbf{g}i}-U_{\mathbf{g}})^2, \tag{3}$$

where $s_{\mathbf{g}i}$ is the standard deviation of refinement i and the weights $w_{\mathbf{g}i}$ are $(1/s_{\mathbf{g}i})/(\Sigma_i 1/s_{\mathbf{g}i})$.

The x-ray structure factors $F_{\mathbf{g}}$ are related to the electron structure factors through the reciprocal version of Poisson's equation, known as the Mott–Bethe formula.[9] For Mg,

TABLE I. Refinement results. The series is continuous up to (210) except for the missing (112) structure factor ($\sin\theta/\lambda=0.368$ Å^{-1}), for which the CBED patterns suffered from contamination. U are the experimental measured electron structure factors with absorption part U', while F^0 are the converted static lattice x-ray structure factors. % $\sigma(U)$ and % $\sigma(F^0)$ are the standard deviations (in percentage). Note the reduced standard deviations in the conversion of electron structure factors to x-ray structure factors for the low-order reflections ($\sin\theta/\lambda<0.35$ Å^{-1}). n is the number of refinements performed for each structure factor. Sample I is the single crystal from the University of Aarhus and II is the Mg ribbon.

h k l	$\sin\theta/\lambda$	U	U'	F^0	% $\sigma(U)$	% $\sigma(F^0)$	n	Sample
1 0 0	0.181	0.018 45(7)	0.000 35	9.01(1)	0.41	0.14	7	II
0 0 2	0.193	0.034 69(4)	0.000 57	17.56(6)	0.12	0.04	6	I
1 0 1	0.205	0.027 96(9)	0.000 23	14.92(2)	0.33	0.13	8	II
1 0 2	0.264	0.011 53(5)	0.000 32	7.90(2)	0.45	0.24	5	I
1 1 0	0.313	0.018 58(2)	0.000 87	14.59(2)	0.16	0.12	5	II
1 0 3	0.341	0.014 38(3)	0.000 44	12.01(2)	0.27	0.20	3	I
2 0 0	0.361	0.007 721(2)	0.000 31	6.68(1)	0.20	0.21	7	II
0 0 4	0.385	0.014 10(3)	0.000 60	12.74(3)	0.25	0.24	6	I
2 1 0	0.478	0.005 242(2)	0.000 23	5.29(2)	0.30	0.49	3	I
2 0 4	0.528	0.004 471(2)	0.000 23	4.74(2)	0.36	0.60	3	I
2 2 0	0.626	0.006 70(5)	0.000 32	7.76(1)	0.80	1.74	2	II

which has a hexagonal structure (space group $P6_3/mmc$, no. 194) and two atoms per unit cell at special positions c with $\bar{6}m2$ site symmetry, we have

$$F_{\mathbf{g}}=ZC_{\mathbf{g}}T_{\mathbf{g}}-\frac{8\pi^2\epsilon_0 h^2\Omega s^2}{\gamma me^2}U_{\mathbf{g}}. \tag{4}$$

Here Z, $T_{\mathbf{g}}$, ϵ_0, Ω, and s are the atomic number, the temperature factor, the vacuum permittivity, the unit cell volume, and the scattering angle, respectively. The trigonometric factor $C_{\mathbf{g}}$ is defined as the sum $\Sigma_j \exp(2\pi i\mathbf{g}\cdot\mathbf{r}_j)$, where $\mathbf{r}_j$ is the position of atom j, and equals $2\cos\{2\pi[(h+2k)/3+l/4]\}$ for Mg. The three symmetry-allowed sets of reflections have $C_{\mathbf{g}}=2,\sqrt{3}$ or 1, corresponding to $h=k,l=2n$; $h\neq k,l=2n+1$, and $h\neq k,l=2n$, respectively. Finally, $\gamma=1+E_0/(mc^2)$ is a relativistic correction, where E_0 is the accelerating voltage of the microscope.

The intensity distribution in the diffraction patterns depends on the temperature through the nonrefined structure factors, but the sensitivity is not strong enough to refine ADPs. However, the conversion from the electron structure factors to x-ray structure factors (Fourier coefficients of the electron density) is sensitive to the temperature. The choice of ADPs was therefore tested with Wilson-type fitting. The temperature factor can be written as

$$T_{\mathbf{g}}=\exp[-(h^2+hk+k^2)P-l^2Q], \tag{5}$$

where

$$P=2\pi^2\frac{4}{3a^2}\langle u_1^2\rangle,\quad Q=2\pi^2\frac{1}{c^2}\langle u_3^2\rangle, \tag{6}$$

and where $\langle u_1^2\rangle$ and $\langle u_3^2\rangle$ are the ADPs in the **a** and **c** lattice directions, respectively.

Given the temperature factors, x-ray structure factors can finally be calculated from Eq. (4). The so-obtained x-ray structure factors, converted into static lattice values $F_{\mathbf{g}}^0=F_{\mathbf{g}}/T_{\mathbf{g}}$ are shown in Table I. Taking the uncertainty in the temperature factors into account, the variance of $F_{\mathbf{g}}^0$ has been calculated as

$$\sigma^2(F_{\mathbf{g}}^0)=(f_{\mathbf{g}}^2+Z^2)\sigma^2(T_{\mathbf{g}})\sum_i \exp(-4\pi i\mathbf{g}\cdot\mathbf{r}_i)+\left(\frac{K\Omega s^2}{\gamma}\right)^2\sigma^2(U_{\mathbf{g}}). \tag{7}$$

By rewriting Eq. (4), using Eq. (5) and the fact that the x-ray structure factors for Mg are given by $F_{\mathbf{g}}=f_{\mathbf{g}}T_{\mathbf{g}}C_{\mathbf{g}}$, we obtain

$$-\ln T_{\mathbf{g}}=-\ln\left[\frac{8\pi^2\epsilon_0 h^2\Omega s^2 U_{\mathbf{g}}}{\gamma me^2 C_g(Z-f_{\mathbf{g}})}\right]=(h^2+hk+k^2)P+l^2Q. \tag{8}$$

Given $f_{\mathbf{g}}$, the left-hand side of Eq. (8) can be calculated. Hence, P and Q can easily be obtained by least-square fitting. In the present study we have used $f_{\mathbf{g}}$ obtained from both Dirac–Fock[33] and DFT[34] calculations. The latter includes bonding effects, which, as illustrated in Fig. 4, brings the (002) and (101) structure factors up to a straight line and reduces the standard deviations in the ADPs. Using the DFT

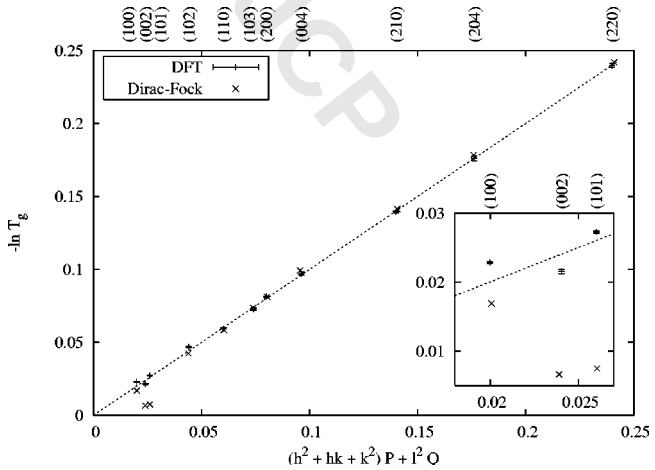

FIG. 4. Wilson-type plot of low-order electron diffraction data for determination of the ADPs in Eq. (8). Static lattice reference $f_{\mathbf{g}}$ is taken both from DFT and Dirac–Fock calculations. The first three points are shown enlarged in the small plot. The slope of the dotted line is 1.

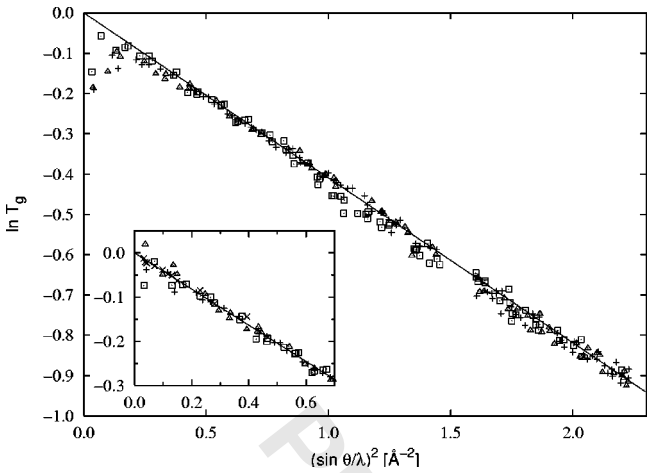

FIG. 5. Wilson plots. X-ray data: $\triangle$ $C_{\mathbf{g}}=2$. $+$ $C_{\mathbf{g}}=\sqrt{3}$. $\square$ $C_{\mathbf{g}}=1$. The small insert shows the the extinction corrected x-ray data, together with the electron diffraction data (marked with $\times$).

values, we obtain $\langle u_1^2\rangle = 7.77(4)\times 10^{-3}$ Å^2 and $\langle u_3^2\rangle = 8.20(10)\times 10^{-3}$ Å^2. Considering that the refinements only depend weakly on the ADPs, these values were so close to the initial values used in the CBED refinements that new refinements were not performed.

C. X-ray diffraction

1. X-ray experiment

X-ray diffraction data were collected with the crystal cooled to 10.2(5) K on a type 512 HUBER four-circle diffractometer equipped with a type CS202 DISPLEX closed-cycle He cryostat at the Department of Chemistry, University of Aarhus.[35]

Graphite monochromated Ag K_α ($\lambda = 0.5608$ Å) was used to collect a complete set of data from the single crystal bar up to $\sin\theta/\lambda = 1.50$ Å^{-1}. A total of 4282 reflections was measured, giving 294 unique data of 12.3 overall average measurement multiplicity. The internal agreement was $R_I(F^2) = 0.025$. The unit cell parameters were obtained by least-square fit to the setting angles of 60 reflections with $41.0° < 2\theta < 43.8°$, yielding $a = b = 3.1925(4)$ Å^{-1}, $c = 5.1795(9)$ Å^{-1}, $d_x = 1.768$ g cm^{-3}, and $\mu = 3.694$ g cm^{-3}.

Data were reduced using the local KRYSTAL program package.[36] Integration was performed with the $\sigma(I)/I$ method[37] and equivalent reflections were averaged using the program SORTAV.[38]

2. X-ray refinement

The structure factor in monoatomic crystals takes the form

$$F_{\mathbf{g}} = f_{\mathbf{g}} C_{\mathbf{g}} T_{\mathbf{g}}. \tag{9}$$

Comparing with Eq. (5), it is seen that $\ln T_{\mathbf{g}}$, as a function of $(\sin\theta/\lambda)^2 = (h^2+hk+k^2)/(3a^2)+l^2/(4c^2)$, should give a straight line for the each of the three symmetry-allowed sets of reflections. Figure 5 illustrates this and shows that the ADPs are reasonably isotropic, as expected for low temperature. Figure 5 also shows how the lowest order x-ray data deviate strongly from a straight line, showing that they are strongly affected by extinction. The high-order data nicely follow a straight line and thereby fix the scaling and ADPs. Figure 1(b) shows how the $2sp$ semicore shell gives a contribution out to $\sin\theta/\lambda > 1.2$ Å^{-1}. A possible core relaxation would influence the refined ADPs and we have therefore refined them only against data with a higher $\sin\theta/\lambda$ using the relativistic Dirac–Fock scattering factors of Su and Coppens,[39] yielding $\langle u_1^2\rangle = 4.86(7)\times 10^{-3}$ Å^2 and $\langle u_3^2\rangle = 5.10(7)\times 10^{-3}$ Å^2. Keeping these parameters fixed, we also tried to refine an isotropic extinction model.[40] The resulting x-ray structure factors corrected for extinction are shown in the small graph of Fig. 5. It is seen that the extinction correction brings the x-ray data onto a reasonably straight line. However, the deviations are still significant, considering that the scale is exponential and the expected deviations from a spherical atom model should be very small. No sign of anisotropic extinction was found in the data, and a model was therefore not attempted.

The small graph of Fig. 5 also shows the CBED data that have been multiplied with a $T_{\mathbf{g}}$, corresponding to the ADPs found from the high-order x-ray data. It is seen that the deviation is very small, as expected.

III. THEORETICAL MODELING

In the present study, we have employed the LAPW method as implemented in the WIEN2K package.[34] The $1s$ and $2s$ electrons were treated fully relativistically as core

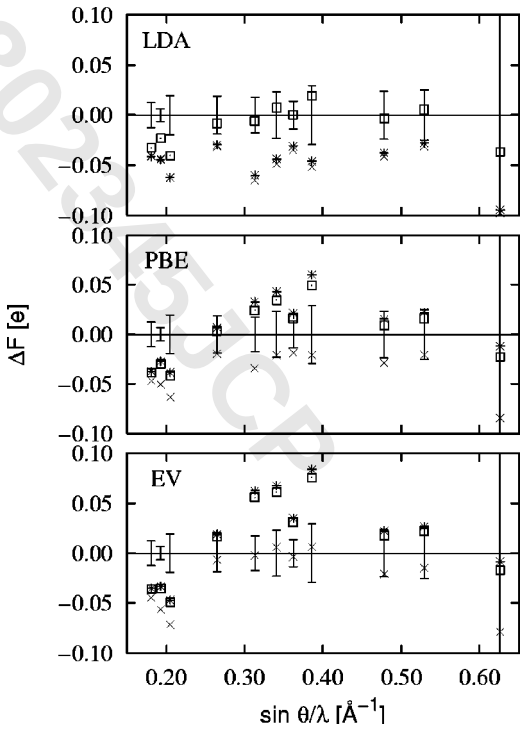

FIG. 6. Structure factor difference between theory and experiment compared with the estimated standard deviation of the experimental value. The differences have been carried out in the local density approximation (LDA), the generalized gradient approximation of Perdew, Burke, and Ernzerhofer (PBE), and that of Engel and Vosko (EV). The shape of the point indicates the self-interaction correction (SIC) applied to the core states $\times$ No SIC, $*$ PZ-SIC, and $\square$ LE-SIC.

TABLE II. Agreement factors $R(F)=[\Sigma|F_{calc}-F_{obs}|]/\Sigma F_{obs}$ and $R_w(F)=[\Sigma w|F_{calc}-F_{obs}|]/\Sigma wF_{obs}$ for various density functionals with the ED data. The symbols refer to Fig. 6.

	(×) $R(F)/R_w(F)$	PZ-SIC (∗) $R(F)/R_w(F)$	LE-SIC □ $R(F)/R_w(F)$
LDA	0.48/0.39	0.46/0.37	0.16/0.14
PBE	0.36/0.32	0.28/0.52	0.25/0.23
EV	0.27/0.26	0.38/0.34	0.37/0.33

TABLE III. Agreement factors for various density functionals with the high-order, $\sin\theta/\lambda>1.2$ Å^{-1}, x-ray data.

Method	$R_w(F)$ (%)	$\langle u_1^2\rangle$ (10^{-3} Å^{-2})	$\langle u_3^2\rangle$ (10^{-3} Å^{-2})
Dirac–Fock (Ref. 39)	0.89	4.86(7)	5.10(7)
LDA	0.89	4.78(7)	5.03(7)
PBE	0.89	4.81(6)	5.06(6)
EV	0.89	4.85(6)	5.09(6)
LDA LE-SIC	0.89	4.84(6)	5.08(7)

electrons, while the valence electrons were treated in the scalar relativistic approximation.[41] A local orbital was added to describe the $2p$ state and the electron density was expanded up to $L=10$. Similarly to the study of Si,[10] we have compared the LDA by Perdew and Wang,[42] the generalized gradient approximations (GGA) by Perdew, Burke, and Ernzerhofer (PBE),[1] and Engel and Vosko (EV)[43] functionals for Mg and will comment on the earlier findings. Due to the very recent work by Novák *et al.*[13] we have also tested the PZ-SIC[15] and LE-SIC[17] schemes.

A. Valence densities

Figure 6 shows the differences between the calculated structure factors and the ones measured by ED. The estimated standard deviations of the experimental values are also shown in the plot. Table II gives the overall agreement factors, which shows that there is a small improvement when going from LDA to PBE to EV, in agreement with the findings of Zuo.[10]

The results of applying a SIC to the core states are also shown in Fig. 6 and Table II. When applying the PZ-SIC[15] only a small improvement is achieved over the LDA results. On the other side a large improvement is gained by applying the LE-SIC, which indicates that it provides a better density. This conclusion agrees perfectly with that of Novák *et al.*,[13] with the added advantage that structure factors sample the whole electron density, not just the spin density in the small Thompson sphere around the nucleus as the hyperfine fields. Considering the conceptual attractiveness of the LE-SIC scheme[17] the agreement is quite satisfying. It is somewhat surprising that the application of SIC to the core states gives a smaller improvement when using GGA. This is probably because the GGA functionals are parametrized to confirm to certain exact relationships[1] or by optimizing the virial relationship.[43] When an SIC is applied to the core orbitals, these parameters can no longer be expected to hold.

Calculations where the SIC was only applied to the $1s$ core state were also performed. Only small differences were found for the low-order structure factors. This could be expected because the $1s$ contribution to the Mg scattering factor is very flat in this region, Fig. 1.

B. Core densities

The improvement of the R factor by applying the SIC to the core states suggests that the main discrepancies between the densities calculated with the standard DFT functionals and experiment are due to poor descriptions of the core densities. This is not surprising, since an inadequate treatment of self-interaction is mainly expected to be important for the core orbitals. It is noted that the LDA is exact for a free-electron gas which should be a good approximation of the valence electrons in Mg.

The low-order reflections analyzed in the previous section contain information about both the core, the semicore, and the valence density. The x-ray structure factors form a complete set out to 1.6 Å^{-1}, and as the high-order reflections are not influenced by extinction they give an excellent possibility for comparisons based only on contributions from the core density. By comparing the calculated electron density from the $2sp$ shell of a free-atom calculation with the calculated density in the crystal, we find a small relaxation of this semicore state which extends out to approximately 1.2 Å^{-1} in reciprocal space. As we also wish to compare with the Dirac–Fock atomic calculations of Su and Coppens[39] where this could be masked as thermal motion, we will only use reflections with $\sin\theta/\lambda>1.2$ Å^{-1}.

Table III shows that when the ADPs are refined, the R factor is the same for all core densities, while the ADPs vary. The EV and LDA LE-SIC functionals give thermal parameters that agree best with the ones obtained from the Dirac–Fock scattering factors.[39] Based on the fact that a Fock solution is explicitly self-interaction-free, we can assume that the Dirac–Fock method gives a good core density. Therefore, these results show that the LE-SIC and EV potentials give the best core densities. The poor agreement between EV and

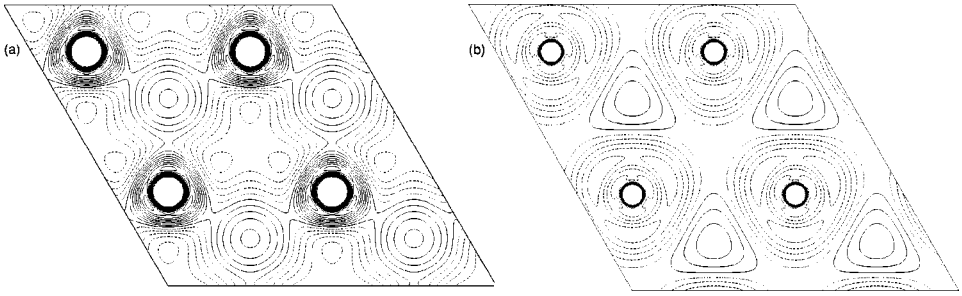

FIG. 7. Deformation map in the basal plane through the atoms parallel to (001) of the hexagonal unit cell of (a) Be and (b) Mg. Contours are plotted at 0.001 e/a.u.^{3} with negative contours as broken lines. The dotted line is the zero contour.

TABLE IV. Critical points in the electron density of beryllium at the experimental lattice constants (Ref. 20). The $(3,-3)$ CP refers to the NNM.

	$\rho(\mathbf{r}_c)$ (e/Å^3)	$-\nabla^2\rho(\mathbf{r}_c)$ (e/Å^5)	Position
$(3,-3)$	0.041 87	−0.006 260	(2/3,1/3,1/4)
$(3,-1)$	0.041 04	−0.004 876	(2/3,1/3,0.080 515)
$(3,+1)$	0.040 21	−0.007 889	(0,0,3/4)
$(3,-1)$	0.041 65	−0.001 099	(0.528 9,1.057 8,1/4)
$(3,+3)$	0.029 50	0.023 66	(0,0,0)

experiment for the low-order structure factors must then be due to a poor description of the valence electrons. The earlier study of Si (Ref. 10) showed that the *R* factor for EV potential was lower for the high-order reflections. This study kept the ADPs fixed to the ones obtained by a fit with atomic scattering factors. Thereby the lowest *R*-factor will be obtained by the functional, giving the core density in the best agreement with the method used to calculate the atomic scattering factors. Our conclusion is therefore based on the same assumption as Zuo *et al.*[10]

IV. THE ELECTRON DENSITY IN HCP METALS

Figure 7 shows the deformation density calculated with the LE-LDA functional in the (001) plane of Be and Mg. The Be plot shows a good agreement both in features and magnitude with the experimental deformation maps derived from high accuracy x-ray structure factors.[18] A main difference between the Be and the Mg maps is that Mg shows no depletion of charge in the octahedral holes. The Mg map is conspicuously more flat, in agreement with the expectation that Mg is closer to a free-electron metal.

The present results have shown that the measured CBED structure factors can be used to quantitatively discriminate between different DFT functionals which can be used for the discussion of the presence of NNM in these simple metals. Using the same kind of argumentation, it was earlier[12] found that the application of the PBE favored the existence of NNM and, compared to the LDA, improved the agreement between calculated and experimental structure factors for Be. It was therefore argued that it was very likely that an NNM would also be found if the unknown exact functional could be applied. In the present study (Table II) we have shown that the calculated charge density can be further improved by applying the LDA LE-SIC functional. If we apply the LDA LE-SIC functional to Be and Mg, an NNM ($(3,-3)$ critical point) is found for Be (Table IV) but not for Mg (Table V), in agreement with the earlier findings.[12] The NNM for Be is extremely small (Table IV) and of the same magnitude as the uncertainty of the electron density derived from experimental structure factors.[18,23] The procedure applied in the present study can be viewed as applying a model that is very flexible, but at the same time constrained to the physical constraint of self-consistency within a systematically constructed functional. We therefore argue that the present study is the closest yet to experimental evidence for the existence of NNM in Be.

TABLE V. Critical points in the electron density of magnesium at the experimental lattice constants (Ref. 20).

	$\rho(\mathbf{r}_c)$ (e/Å^3)	$-\nabla^2\rho(\mathbf{r}_c)$ (e/Å^5)	Position
$(3,+1)$	0.015 46	−0.000 282	(2/3,1/3,1/4)
$(3,+1)$	0.014 59	0.002 498	(0,1/2,0)
$(3,-1)$	0.014 70	0.000 874	(2/3,1/3,0.077 371)
$(3,-1)$	0.015 47	−0.000 110	(0.701 497,0.402 994,1/4)
$(3,+3)$	0.010 36	0.005 938	(0,0,0)

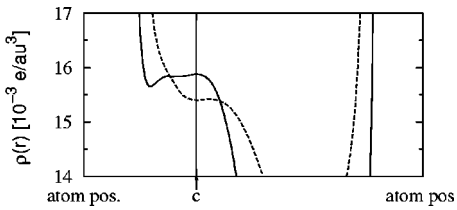

FIG. 8. Total electron density plotted along the $[1\,\bar{1}\,0]$ direction from atom to atom in the basal plane, Be (full line) and Mg (dashed line). The c-arrow marks the center of bipyramidal space where atoms lie directly above and below the basal plane. The Be curve exhibits a maximum going through s $(3,-3)$ critical point, while the Mg curve has a minimum at this point, a $(3,+1)$ critical point. The density of Be has been shifted down by 26×10^{-3} e/a.u.^{3} to bring the plots onto the same scale.

Figure 8 illustrates the variation of the total density between atomic positions in the Be and Mg hcp structures. It shows how the core density of Mg is more extended than the very contracted (unscreened) core density of Be, which means the existence of NNM is most probable for the elements belonging to the second period.[12]

V. CONCLUSION

It has been shown that sufficient accurate low-order structure factors can be measured by CBED to experimentally test DFT functionals. The core densities can be tested against high-order x-ray data that are not affected by extinction. It was found that the agreement with experiment increases when going from the LDA to the PBE to the EV. The improvement of the EV comes mainly from a better description of the core states. Applying the PZ-SIC to the core states for LDA did not improve the agreement with theory, while applying the LE-SIC of Lundin and Eriksson resulted in a significantly improved agreement. The LDA LE-SIC functional also agreed well with the x-ray data at scattering angles larger than 1.2 Å^{-1}. Using this functional an NNM in the electron density was found for Be but not for Mg.

ACKNOWLEDGMENTS

The experiment support at the CHREM center at ASU and the fundings by DOE DE-FG03-02ER45596 and the Research Council of Norway (NFR), Project 135270/410 are gratefully acknowledged.

[1] J. P. Perdew, K. Burke, and M. Ernzerhof, Phys. Rev. Lett. **77**, 3865 (1996).
[2] M. Fuchs, M. Bockstedte, E. Pehlke, and M. Scheffler, Phys. Rev. B **57**, 2134 (1998).
[3] S. Kurth, J. P. Perdew, and P. Blaha, Int. J. Quantum Chem. **75**, 889 (1999).
[4] M. Sakata and M. Sato, Acta Crystallogr., Sect. A: Found. Crystallogr. **46**, 263 (1990).

[5] M. A. Spackman, Acta Crystallogr., Sect. A: Found. Crystallogr. **47**, 420 (1991).
[6] O. K. Andersen, Phys. Rev. B **12**, 3060 (1975).
[7] E. Wimmer, H. Krakauer, M. Weinert, and A. J. Freeman, Phys. Rev. B **24**, 864 (1981).
[8] G. K. H. Madsen, P. Blaha, K. Schwarz, E. Sjöstedt, and L. Nordström, Phys. Rev. B **64**, 195134 (2001).
[9] J. C. H. Spence and J. M. Zuo, *Electron Microdiffraction* (Plenum, New York, 1992).
[10] J. M. Zuo, P. Blaha, and K. Schwarz, J. Phys.: Condens. Matter **9**, 7541 (1997).
[11] Z. W. Lu, A. Zunger, and M. Deutsch, Phys. Rev. B **52**, 11904 (1995).
[12] G. K. H. Madsen, P. Blaha, and K. Schwarz, J. Chem. Phys. **117**, 8030 (2002).
[13] P. Novák, J. Kuneš, W. E. Pickett, W. Ku, and F. R. Wagner, Phys. Rev. B **67**, 140403 (2003).
[14] R. Laskowski, P. Blaha, and K. Schwarz, Phys. Rev. B **67**, 075102 (2003).
[15] J. P. Perdew and A. Zunger, Phys. Rev. B **23**, 5048 (1981).
[16] A. Svane, W. M. Temmerman, Z. Szotek, J. Lægsgård, and H. Winter, Int. J. Quantum Chem. **77**, 799 (2000).
[17] U. Lundin and O. Eriksson, Int. J. Quantum Chem. **81**, 247 (2001).
[18] F. K. Larsen and N. K. Hansen, Acta Crystallogr., Sect. B: Struct. Crystallogr. Cryst. Chem. **40**, 169 (1984).
[19] Y. Kubota, M. Takata, and M. Sakata, J. Phys.: Condens. Matter **5**, 8245 (1993).
[20] B. B. Iversen, F. K. Larsen, M. Souhassou, and M. Takata, Acta Crystallogr., Sect. B: Struct. Crystallogr. Cryst. Chem. **51**, 580 (1995).
[21] R. Y. de Vries, W. J. Briels, and D. Feil, Phys. Rev. Lett. **77**, 1719 (1996).
[22] D. Jayatilaka, Phys. Rev. Lett. **80**, 798 (1998).
[23] B. B. Iversen, J. L. Jensen, and J. Danielsen, Acta Crystallogr., Sect. A: Found. Crystallogr. **53**, 376 (1997).
[24] A. M. Pendás, M. A. Blanco, A. Costales, P. M. Sánchez, and V. Luaña, Phys. Rev. Lett. **83**, 1930 (1999).
[25] R. F. W. Bader and J. A. Platts, J. Chem. Phys. **107**, 8545 (1997).
[26] G. K. H. Madsen, C. Gatti, B. B. Iversen, L. Damjanovic, G. D. Stucky, and V. I. Srdanov, Phys. Rev. B **59**, 12359 (1999).
[27] G. K. H. Madsen, B. B. Iversen, P. Blaha, and K. Sehwarz, Phys. Rev. B **64**, 195102 (2001).
[28] B. Jiang, J. M. Zuo, J. Friis, and J. C. H. Spence, Microsc. Microanal. (in press).
[29] J. M. Zuo, Mater. Trans., JIM **39**, 938 (1998).
[30] P. Rez, Acta Crystallogr., Sect. A: Found. Crystallogr. **34**, 48 (1978).
[31] B. B. Iversen, S. K. Nielsen, and F. K. Larsen, Philos. Mag. A **72**, 1357 (1995).
[32] J. Friis, B. Jiang, J. C. H. Spence, and R. Holmestad, Mater. Trans., JIM (in press).
[33] Z. Su and P. Coppens, Acta Crystallogr., Sect. A: Found. Crystallogr. **53**, 749 (1997).
[34] P. Blaha, K. Schwarz, G. Madsen, D. Kvasnicka, and J. Luitz, WIEN2K, *An Augmented Plane Wave Plus Local Orbitals Program for Calculating Crystal Properties* (Vienna University of Technology, Austria, 2001).
[35] F. K. Larsen, Acta Crystallogr., Sect. B: Struct. Crystallogr. Cryst. Chem. **51**, 468 (1995).
[36] A. C. Hazell, *A Suite of Crystallographic Programs for Data Reduction and Refinement* (Dept. of Chemistry, University of Aarhus, Århus, Denmark).
[37] M. S. Lehmann and F. K. Larsen, Acta Crystallogr., Sect. A: Found. Crystallogr. **30**, 580 (1974).
[38] R. T. Blessing, J. Appl. Crystallogr. **22**, 396 (1989).
[39] Z. Su and P. Coppens, Acta Crystallogr., Sect. A: Found. Crystallogr. **54**, 646 (1998).
[40] P. J. Becker and P. Coppens, Acta Crystallogr., Sect. A: Found. Crystallogr. **30**, 129 (1974).
[41] A. H. MacDonald, W. E. Pickett, and D. D. Koelling, J. Phys. C **13**, 2675 (1980).
[42] J. P. Perdew and Y. Wang, Phys. Rev. B **45**, 13244 (1992).
[43] E. Engel and S. H. Vosko, Phys. Rev. B **47**, 13164 (1993).

Paper 5

A Study of Charge Density in Copper

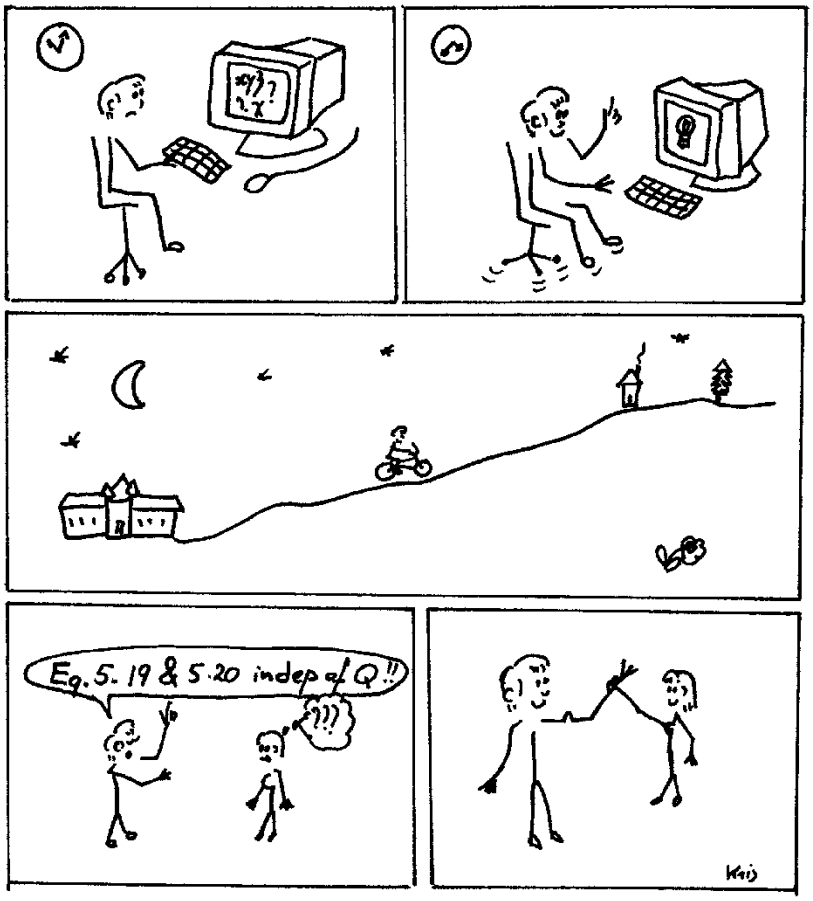

Acta Crystallographica Section A
Foundations of Crystallography
ISSN 0108-7673

A Study of Charge Density in Copper

J. Friis,[a]* B. Jiang,[b] K. Marthinsen[c] and R. Holmestad[a]

[a]Department of Physics, Norwegian University of Science and Technology (NTNU), 7491 Trondheim, Norway, [b]Department of Physics and Astronomy, Arizona State University, Tempe, AZ 85287-1504, USA, and [c]Department of Materials Technology, Norwegian University of Science and Technology (NTNU), 7491 Trondheim, Norway. Correspondence e-mail: jesper.friis@phys.ntnu.no

November 5, 2003

Quantitative convergent beam electron diffraction (QCBED) experiments allow absolute scale measurements of low order structure factors with very high accuracy. In this paper, eight low order structure factors for copper measured by QCBED have been combined with the higher order γ-ray structure factors in order to obtain a larger high-accurate experimental data set. The γ-ray values were relativistically corrected and rescaled. The new data set was then used for studying the charge distribution in copper. Charge deformation maps have been produced and both a *maximum entropy* and a *multipole analysis* have been applied to the data. The result is compared to *density functional theory* calculations. We find an almost spherical charge depletion around the atomic sites showing typical metal bonding in copper.

1. Introduction

Recently, very accurate measurements of low order structure factors in copper have been performed (Friis *et al.*, 2003). In this work we have enhanced the accuracy of the measurements somewhat further. The new data set is then combined with the corrected (Petrillo *et al.*, 1998) γ-ray measurements of Schneider *et al.* (1981), and used for a more detailed study of the charge distribution in copper.

The deformation density, defined as the difference between the observed density and the *procrystal* density, where independent atoms are placed at the atomic sites, describes the redistribution of electronic charge due to bonding. Since this charge redistribution mainly occurs in the valence region where the charge density varies slowly, the bonding effect is mainly seen in the differences between the lowest order observed and *independent atom model* (IAM) structure factors. Since these differences are very small (around or less than 1%), very accurate measurements are required. Such an accuracy is difficult to obtain for the strong low order reflections using ordinary X-ray diffraction, due to extinction and the contribution of anomalous scattering. A way to overcome this problem is to combine different techniques.

Copper has for a long time been used as a test case for theoretical models of elements containing the complicated *d* electron bands. It is non-magnetic, and is relatively uncomplicated by relativistic effects because of its small mass. It is therefore not surprising that there has been many experimental measurements of the structure factors.

By using *γ-ray diffractometry*, Schneider *et al.* (1981) could reduce the anomalous scattering and extinction effects in copper, compared to earlier powder and single crystal X-ray experiments (Batterman *et al.*, 1961; Jennings *et al.*, 1964; Hosoya & Yamagishi, 1966; Temkin *et al.*, 1972; Freud, 1973). However, the available scattering angles were at the same time reduced. Since it is difficult to obtain large perfect crystals of copper, required for traditional X-ray Pendellösung experiments, Takama & Sato (1982) measured a few low order structure factors using a *white beam X-ray Pendellösung method*. Although not as accurate as the ordinary Pendellösung method, this technique does not require so large single crystals. More recently, accurate structure factors have been measured by electron diffraction techniques. A big advantage of these methods is that they are performed in a *transmission electron microscope* (TEM), making it possible to select a perfect single crystalline region for the experiment. However, the accuracy of these techniques is reduced for higher order structure factors. Smart & Humphreys (1980) and Fox & Fisher (1988, in Tabbernor *et al.*, 1990) used the *critical-voltage method*, which is capable of measuring the ratio between structure factors as accurate as 0.1%. A limitation is that this method relies upon the accuracy of the reference used. The *intersecting Kikuchi-line method*, proposed by Gjønnes & Høier (1971), uses the sensitivity of the separation between high order Kikuchi-lines to certain structure factors. This method was combined with *convergent beam electron diffraction* (CBED) by Matsuhata *et al.* (1984) for measuring the $(\bar{1}11)$ and (020) reflections of copper. However, the most accurate experiments on copper so far are probably the *quantitative CBED* (QCBED) measurements by Saunders *et al.* (1999) and Friis *et al.* (2003). The strong multiple scattering of the electrons is here fully taken into account by using dynamical theory, which at the same time eliminates extinction and scaling problems. More detailed overviews of the above experiments on copper can be found in Tabbernor *et al.* (1990), Mackenzie & Mathieson (1992) and Friis *et al.* (2003).

The γ-ray experiment by Schneider *et al.* (1981) is probably the most referred structure factor measurement for copper. The reasons for this is probably the good internal consistency of the data and that the data set is comparably large; 19

IUCr macros version 2.0/β10: 2002/12/11 November 5, 2003

structure factors were measured up to $\sin\theta/\lambda = 1.6$ Å^{-1} at 50 K and room temperature (Schneider, 1976). However, compared to other experiments these structure factors are somewhat low. The absolute scale and even the extinction correction of the γ-ray data has therefore been questioned and several different corrections have been proposed. By applying an improved extinction correction scheme to the (220) structure factor, Mackenzie & Mathieson (1984) obtained a value closer to that of other experiments. On the other hand Tabbernor *et al.* (1990) pointed out that good agreement also can be achieved by rescaling the data set to fit the (111) reflection of Fox & Fisher (1988). The idea that the discrepancy is due to problems with absolute scale, and not to the extinction correction, is also approved by Schneider (Tabbernor *et al.*, 1990). In a new analysis of Schneider *et al.*'s (1981) data, Petrillo *et al.* (1998) chose a slightly smaller Debye-Waller factor for Cu at 50 K. More important, Petrillo *et al.* (1998) applied a kinematic correction (in the order of the experimental errors), which importance first was realized by Dewey *et al.* (1994). This correction is due to the relativistic energies of the γ-rays and can be interpreted as a relativistic change of the electron mass. Finally a scaling factor of 1.0042(62) was introduced in order to fit the relativistic Hartree-Fock free-atom structure factors (Doyle & Turner, 1968) for scattering angles $\sin\theta/\lambda > 0.5$ Å^{-1}.

In section 2., we give a brief overview of the QCBED experiment and in 3. we combine the QCBED data with γ-ray measurements. In the following sections we use this data set for studying the charge redistribution due to bonding in copper. In section 4. we discuss the deformation density obtained by a simple Fourier synthesis. In section 5. the results from the *maximum entropy method* (MEM) are discussed. Finally, in section 6., we will discuss the results of a *multipole analysis*.

2. QCBED measurements of structure factors

In the CBED technique, the electron probe in the TEM is focused down to the size of a few nanometers. This makes it easy to study perfectly crystalline regions of the sample. Since the CBED patterns show the rocking curve of every diffracted beam simultaneously, they are well suited for quantitative work (Spence & Zuo, 1992; Zuo, 1998). Because electrons interact strongly with the crystal potential and are multiple scattered when they pass through the sample, a full dynamic theory is required when analyzing the CBED patterns. Extinction, which is a problem in X-ray diffraction of the strong low order reflections in small unit-cell crystals, is therefore fully accounted for in QCBED. The QCBED method is based on a pixel to pixel comparison between the experiment and a Bloch wave simulation, where the Fourier coefficients of the crystal potential $V_{\mathbf{g}}$ are treated as refinable parameters (Zuo, 1998). A typical CBED pattern is shown in Fig. 1a for the (220) systematic row with some line scans, sensitive to the refined parameters, marked on it. Fig. 1b shows the best fit along the chosen line scans obtained with the Bloch-wave simulation.

For bonding studies, the interesting quantity is the electron density, of which Fourier components are the X-ray structure factors $F_{\mathbf{g}}$. These are directly related to $V_{\mathbf{g}}$ through the reciprocal space version of Poisson's equation (also known as the Mott-Bethe formula). The operation of this equation provides increased sensitivity to the low order structure factors (Spence & Zuo, 1992).

The structure factors reported in Table 1 under "this experiment" are the structure factors from Friis *et al.* (2003) with some new refinements. These additions have not led to any significant changes in the structure factor values, but the errors are somewhat decreased due to better statistics. Most notable is that the value of the (420) structure factor has been added to the data set. We believe that this experiment, together with the one of Saunders *et al.* (1999), is the most accurate measurement of the low order structure factors of copper done so far.

3. Combination with γ-ray data

In order to reduce truncation errors due to the limited set of measured structure factors in the study of charge density, the QCBED data have been combined with the γ-ray measurements of Schneider *et al.* (1981). However, three corrections have been applied to the γ-ray data (in the given order) before combining them with the QCBED data:

(i) Subtraction of the relativistic correction Δ, calculated by Petrillo *et al.* (1998), from the γ-ray values.

(ii) As suggested by Petrillo *et al.* (1998), we use the value $B = 0.153$ Å^2 from Svensson *et al.* (1969) as the 50 K Debye-Waller factor for copper, which is almost identical to the value obtained from a Wilson plot of the relativistically corrected data ($B = 0.152$ Å^2, Fig. 2). This should be compared to the Debye-Waller factor of $B = 0.167$ Å^2 obtained from a Wilson-plot of the original data (Schneider *et al.*, 1981).

(iii) Rescaling of the data with a scaling factor $k = 1.0084$, defined from

$$\begin{aligned} k\,|F^{\rm obs}| &= \exp(-Bs^2)|F^0| \\ \ln\left|\frac{F^0}{F^{\rm obs}}\right| &= \ln k + Bs^2, \end{aligned} \qquad (1)$$

in order to obtain a best fit to the QCBED data. Here $s = \sin\theta/\lambda$ is the scattering angle and F^0 are static lattice structure factors obtained from DFT calculations (using the WIEN2k program, Blaha *et al.*, 2001).

These corrections are all of the order of the standard deviations and are largest for the low order reflections. We have applied the same small increase of the standard deviations, due to the uncertainties introduced by the corrections, as used by Petrillo *et al.* (1998). The corrected and combined data sets are shown in Table 1, respectively labeled as "corrected" and "combined".

The new data set is plotted with error bars in Fig. 3 relative to values obtained from the IAM. Except for a few outliers, (600), (800) and (10,0,0), we see no significant difference between the combined and the IAM data sets for scattering angles $\sin\theta/\lambda > 0.5$ Å^{-1}.

4. Charge deformation density of copper

The kinematic non-forbidden structure factors for Cu take the form

$$F(s) = 4f(s)\exp(-Bs^2) \qquad (2)$$

where f is the atomic scattering factor (or form factor). For the IAM, several good parameterizations of the scattering factors exist (Macchi & Coppens, 2001; Peng, 1998; Su & Coppens, 1997). The most famous and widely used is probably the relativistic Hartree-Fock scattering factors of Doyle & Turner (1968), which are used for the IAM in this paper. A commonly used quantity for recognition of bonding features is the *deformation density*

$$\Delta\rho(\mathbf{r}) = \frac{1}{V}\sum_{\mathbf{h}} \left(F_{\mathbf{h}}^{\rm obs} - F_{\mathbf{h}}^{\rm IAM}\right) \exp(-2\pi i \mathbf{r}\cdot\mathbf{h}) \qquad (3)$$

defined as the difference between the crystal and the IAM densities. V is the unit cell volume. The deformation density shows charge accumulation in bonding regions, but quantitative applications cannot be drawn too long, since the deformation density depends on the definition of the reference density and is thermally averaged. Another practical limitation of deformation densities calculated from a set of measured structure factors is the errors due to series truncation. As shown in Fig. 5, these errors are mainly concentrated to high-symmetric regions. For copper it is common to plot the charge density in the (110)-plane since this plane contains both nearest, second nearest and third nearest neighbors. Fig. 4 shows the deformation density calculated from the 12 lowest order structure factors ($\sin\theta/\lambda \leq 0.79$ Å^{-1}) in the combined data set. The standard deviations of the deformation density, shown in Fig. 5, were calculated according to the formalism of Rees (1976) and Rees & Mitschler (1976). The strong dependency of the number of surrounding symmetry equivalent points, with maximum at high-symmetric regions, is an effect of truncation errors.

The deformation density in Fig. 4 shows, as expected from metallic bonded crystals, charge depletion at the atomic sites and a build up of charge in the interstitial regions. A maximum of 0.19 eÅ^{-3} is seen at the interstitial octahedral sites. However, this maximum is not significant due to the large standard deviations, $\sigma(\Delta\rho) = 0.26$ eÅ^{-3} at the octahedral sites.

In the following two sections more sophisticated methods are used in order to deal with the truncation and other errors due to the incompleteness of the data.

5. Maximum entropy fitting of direct-space charge density

The *maximum-entropy method* (MEM) is a method based on information theory to enhance information from limited or poor data. Applications in crystallography have been reviewed by Gilmore (1996). It has often been used to calculate the charge density distribution from a limited set of structure factors (Collins, 1982; Sakata & Sato, 1990; Papoular *et al.*, 1996). The basic idea is to find the charge distribution which maximize the entropy, under the constraint that structure factors calculated from this distribution must match the measured structure factors.

But, as pointed out by Jauch & Palmer (1993) and Jauch (1994), the traditional maximum entropy algorithm is limited when fine details, such as bonding deformation, are to be studied, and the charge density to be reconstructed has a large dynamic range. However, if one uses the deformation density $\Delta\rho(\mathbf{r})$ as the key quantity when maximizing the entropy, the dynamic range is substantially reduced and the small bonding features become more pronounced. Since MEM relates the charge density directly to probabilities, the use of the deformation density, which takes both positive and negative values, requires a *two channel method*. This method has successfully been used for magnetization densities (Papoular & Gillon, 1990), in neutron diffraction involving scattering lengths of opposite signs (Sakata *et al.*, 1993) and deformation densities (Papoular *et al.*, 1996).

In the two channel method the deformation density is split into two quantities, a positive $\rho^+(\mathbf{r})$ and a negative $\rho^-(\mathbf{r})$ part, such that $\Delta\rho(\mathbf{r}) = \rho(\mathbf{r}) - \rho^{\rm IAM}(\mathbf{r}) = \rho^+(\mathbf{r}) - \rho^-(\mathbf{r})$. The unit cell is divided into M pixels, each of size V/M centered at $\mathbf{r}_j$ and with densities $\rho_j^+ = \rho^+(\mathbf{r}_j)$ and $\rho_j^- = \rho^-(\mathbf{r}_j)$. The entropy functional, to be maximized, is given by

$$S[\Delta\rho] = -\sum_{j=1}^{M}\left[p_j^+ \ln p_j^+ + p_j^- \ln p_j^-\right], \qquad (4)$$

where $p_j^\pm = \rho_j^\pm/Q^\pm$, with $Q^\pm = \sum_j \rho_j^\pm$, are the corresponding probabilities for the positive and negative parts of the deformation density associated with pixel j. The maximization of $S[\Delta\rho]$ is performed under the constraint that the difference between the structure factors calculated from the MEM charge density and the IAM structure factors

$$\Delta F_{\mathbf{h}}^{\rm calc} = \frac{V}{M}\sum_{j=1}^{M}\left(Q^+ p_j^+ - Q^- p_j^-\right)\exp(2\pi i\mathbf{h}\cdot\mathbf{r}). \qquad (5)$$

agrees with the difference between the observed structure factors and IAM structure factors $\Delta F_{\mathbf{h}}^{\rm obs}$ within the standard deviation $\sigma_{\mathbf{h}}$. This condition is expressed as

$$\chi^2 = \frac{1}{N}\sum_{\mathbf{h}} \left|\Delta F_{\mathbf{h}}^{\rm obs} - \Delta F_{\mathbf{h}}^{\rm calc}\right|^2 / \sigma_{\mathbf{h}}^2 \lesssim 1\ . \qquad (6)$$

The problem is solved by maximizing the Lagrange functional $L[\rho] = S[\Delta\rho] - \lambda\chi^2$, where λ is the a Lagrange multiplier. At convergence $\nabla_\rho L = 0$, resulting in the normalized densities

$$p_j^\pm = m_j^\pm \exp\left(\mp\lambda\frac{\partial\chi^2}{\partial p^\pm}\right), \qquad (7)$$

where $m_j^\pm$ are prior density distributions. The deformation density is obtained by solving Eq. (5), (6) and (7) iteratively for both $p^\pm$ and λ, starting from a flat deformation density and $\lambda \gtrsim 0$.

It has been argued that a problem with two-channel MEM applied to the deformation density, is that Q^+ and Q^- are unknown. However, since the total amount of charge is conserved in the formation of the deformation density, we must have $Q^+ = Q^- = Q$. It is then easy to show that, by introducing a scaled Lagrange multiplier $\Lambda = \lambda Q$, one can move all dependence of Q into this Lagrange multiplier. Hence, the value one choose for Q doesn't matter, since the Lagrange multiplier

is already an unknown parameter that has to be given a suitable value in order to achieve convergence.

The MEND program (Sakata & Takata, 1994) modified by Burger (1998), was used to solve the problem. The unit cell was divided into $128 \times 128 \times 128$ pixels. In order to check that the algorithm only depends on the product of λ and Q, several different starting points with uniform prior deformation densities, $\Delta\rho^{+}_{0,j} = \Delta\rho^{-}_{0,j} = 0.05, 0.1, 1.0, 2.5$ eÅ^{-3}, were tried. In all cases the same convergence was achieved with λ_0 around $(5{\cdot}10^{-4}\,\text{eÅ}^{-3})/\Delta\rho_{0,j}$. The same results were also obtained with smaller grids of $32 \times 32 \times 32$ and $64 \times 64 \times 64$ pixels.

The deformation density for $\Delta\rho^{+}_{0,j} = \Delta\rho^{-}_{0,j} = 0.05$ eÅ^{-3} and $\lambda_0 = 0.01$ is shown in Fig. 6. This map is quite similar to the one obtained from direct Fourier synthesis. It shows an average interstitial charge surplus of 0.05 eÅ^{-3} and a less pronounced peak at the interstitial octahedral sites. Instead, small maxima are seen between the nearest neighbors, at the tetrahedral sites and at the $(1/4, 1/4, 1/2)$ positions (the positions furthest away from the atomic sites).

6. Multipole analysis

In multipole analysis the atomic charge density is expanded in terms of a series of multipolar functions centered at the nucleus. The multipole populations and radial expansion parameters, are determined from least square fitting to the measured structure factors. This method has the advantage that it provides an analytical expression for the charge density, allowing for easy calculation of physical properties based on the charge distribution. Another interesting feature is that the multipole populations can be related to orbital occupancies.

In the *valence-density formalism* of Hansen & Coppens (1978) the atomic electron density

$$\begin{aligned}\rho_{\text{atom}}(\mathbf{r}) &= P_c\rho_{\text{core}}(r) + P_v\kappa^3\rho_{\text{valence}}(\kappa r) \\ &+ \sum_{l=0}^{l_{\max}} \kappa_l'^3 R_l(\kappa_l' r) \sum_{m=0}^{l} P_{lm\pm}\, d_{lm\pm}(\theta,\phi). \qquad (8)\end{aligned}$$

is described by three parts; a spherically core part populated with P_c electrons, a spherically valence part which is allowed to expand ($\kappa < 1$) or contract ($\kappa > 1$) with population P_v and a series of multipolar functions accounting for an aspherically redistribution of the electron density, each populated with P_{lmp} electrons. The multipolar functions are characterized by the radial functions $R_l(\kappa_l' r)$ and the density functions $d_{lm\pm}(\theta,\phi)$, that are density-normalized real spherical harmonics (Coppens, 1997, Chap. 3). Because of the strong symmetry imposed by the cubic atom site symmetry of copper, all terms in the multipole expansion up to $l_{max} = 3$, except for the monopole will vanish (Kurki-Suonio, 1977). For the hexadecapoles ($l = 4$) only one independent cubic population parameter P_{hex} will remain.

In Jiang *et al.* (2003) a multipole analysis for the combined data set was performed. Assuming that the 3*d* radial wave function has a tail that does not contribute significantly to the measured reflections; a model that reproduces very well the observed structure factors could be obtained. This deformation of the 3*d* orbital was simulated by writing the 3*d* orbital as $3d_{\text{deformed}} = 3d^{10-n}4s^n$ with $n = 1.27$, where 3*d* and 4*s* here refers to Clementi & Roetti's (1974) Slater-type radial functions.

This model results in a negligible aspherical contribution to the charge density in copper ($P_{\text{hex}} = -0.0001$), which is also seen from the spherical charge depletion around the atomic sites in the deformation density (Fig. 7). The fact that spherical model seems to give a very good description of copper, also validates our special construction of the $3d_{\text{deformed}}$ radial function. More details are given in Jiang *et al.* (2003).

7. Discussion and conclusions

For comparison, several sets of low order scattering factors for copper are listed in Table 1. The theoretically calculated values are the IAM scattering factors by Doyle & Turner (1968), the self-consistent band structure calculation by Bagayoko *et al.* (1980) and a full-potential DFT calculation using the generalized gradient approximation (GGA) performed with the WIEN2k program package (Blaha *et al.*, 2001). Experimental values are the γ-ray diffractometry measurements by Schneider *et al.* (1981), the QCBED experiment by Saunders *et al.* (1999) and the QCBED experiment presented here. The two last rows show the scattering factors obtained by applying MEM and multipolar analysis to the combined data set. The difference between the scattering factors and the IAM values are plotted in Fig. 3. The difference between the DFT, MEM, observed and multipole scattering factors and the IAM values are also plotted in Fig. 3.

First of all, the R-factors show that the agreement between γ-ray measurements and our experiments increases a lot by the corrections. Compared to the old calculation by Bagayoko *et al.* (1980) the DFT calculation shows a significant improvement in the R-factor for our experiment. However, the agreement for the DFT calculation is worse, when the higher order corrected γ-ray data is also taken into account. Since the GGA method is usually more accurate for higher orders, this might imply that there are still some problems with the γ-ray data, despite the corrections.

In Jiang *et al.* (2003) it is seen from the DFT calculations that the scattering from the valence 3*d* and 4*s* orbitals is very small at $\sin\theta/\lambda = 0.8$ Å^{-1} and almost vanish for scattering angles larger than 1 Å^{-1}. One would therefore expect the true scattering factors to be very close to the IAM values for $\sin\theta/\lambda > 1.0$ Å^{-1}. This is the case for the DFT calculations and the multipole model, but not for the (600), (800) and (10,0,0) corrected γ-ray scattering factors.

It is clear from Fig. 3 that our multipole model fits the observed scattering factors very well. The only exceptions are the (600), (800) and (10,0,0) reflections, for which it gives the scattering factors expected from DFT. In fact, the agreement between DFT and the multipole model is excellent, and justifies our construction of the 3*d* multipolar orbital. The charge deformation density from the DFT calculation is shown in Fig. 8. It is very close to the multipolar deformation density in Fig. 7. Both these maps show a spherical charge depletion at the atomic

sites, typical for metallic bonding, but also a small charge surplus between the nearest neighbors.

The maximum entropy method tends to move the structure factors toward the IAM-values (Fig. 3), that are the structure factors maximizing the entropy for the two-channel method used in this work. This does not seems to provide much physical insight. However, MEM can be seen as a statistical method to reduce the problems with incomplete data sets and truncation errors in deformation density maps obtained by Fourier synthesis. And indeed, the MEM deformation density map (Fig. 6) shows similar features to those from DFT (Fig. 8), but the radius of the spherical charge depletion around the nucleus is too small.

In summary DFT and the multipole model seem to provide a very good description of copper, which shows typical metallic bonding.

We thank prof. J.C.H. Spence (Arizona State University) and prof. J.M. Zuo (University of Illinois) for helpful discussions. Funding from the Research Council of Norway (NFR), project 135270/410 is gratefully acknowledged. B. Jiang is funded by DOE DE-FG03-02ER45596.

References

Bagayoko, D., Laurent, D. G., Singhal, S. P. & Callaway, J. (1980). *Phys. Lett. A*, **76**, 187–190.

Batterman, B. W., Chipman, D. R. & Marco, J. J. D. (1961). *Phys. Rev.* **76**, 68–74.

Blaha, P., Schwarz, K., Madsen, G., Kvasnicka, D. & Luitz, J., (2001). *WIEN2k, An Augmented Plane Wave Plus Local Orbitals Program for Calculating Crystal Properties.* Vienna University of Technology, Austria.

Burger, K., (1998). *Enchanced Versions of the Maximum Entropy Program MEED for X-ray and Neutron Diffraction.* Inst. für Kristallographie, Universität Tübingen.

Clementi, E. & Roetti, C. (1974). *Atomic Data and Nuclear Data Tables*, **14**, 177–478.

Collins, D. M. (1982). *Nature*, **298**, 49–51.

Coppens, P. (1997). *X-Ray Charge Densities and Chemical Bonding.* Oxford University Press.

Dewey, M. S., Kessler, E. G., Greene, G. L., Deslattes, R. D., Sacchetti, F., Petrillo, C., Freund, A., Börner, H. G., Robinson, S. & Schillebeecks, P. (1994). *Phys. Rev. B*, **50**, 2800–2808.

Doyle, P. A. & Turner, P. S. (1968). *Acta Cryst. A*, **24**, 390–397.

Fox, A. G. & Fisher, R. M. (1988). Unpublished, see Tabbernor *et al. (1990).*

Freud, A. (1973). Ph.D. thesis, Technische Universität München.

Friis, J., Jiang, B., Spence, J. C. H. & Holmestad, R. (2003). *Micros. and Microanal.* **9**, 379–389.

Gilmore, C. (1996). *Acta Cryst. A*, **52**, 561–589.

Gjønnes, J. & Høier, R. (1971). *Acta Cryst. A*, **24**, 313–316.

Hansen, N. K. & Coppens, P. (1978). *Acta Cryst. A*, **34**, 909–921.

Hosoya, S. & Yamagishi, T. (1966). *J. Phys. Soc. Jpn.* **21**, 2638–2644.

Jauch, W. (1994). *Acta Cryst. A*, **50**, 650–652.

Jauch, W. & Palmer, A. (1993). *Acta Cryst. A*, **49**, 590–591.

Jennings, L. D., Chipman, D. R. & Marco, J. J. D. (1964). *Phys. Rev.* **135**, 1612–1615.

Jiang, B., Friis, J., Holmestad, R., Zuo, J. M., O'Keeffe, M. & Spence, J. C. H. (2003). Submitted.

Kurki-Suonio, K. (1977). *Isr. J. Chem.* **16**, 115–123.

Macchi, P. & Coppens, P. (2001). *Acta Cryst. A*, **57**, 656–662.

Mackenzie, J. K. & Mathieson, A. (1984). *Aust. J. Phys.* **37**, 651–656.

Mackenzie, J. K. & Mathieson, A. (1992). *Acta Cryst. A*, **48**, 231–236.

Matsuhata, H., Tomokiyo, Y., Watanabe & Eguchi, T. (1984). *Acta Cryst. B*, **40**, 544–549.

Papoular, R. J. & Gillon, B. (1990). *Europhys. Lett.* **13**, 429–434.

Papoular, R. J., Vekhter, Y. & Coppens, P. (1996). *Acta Cryst. A*, **52**, 397–407.

Peng, L. M. (1998). *Acta Cryst. A*, **54**, 481–485.

Petrillo, C., Sacchetti, F. & Mazzone, G. (1998). *Acta Cryst. A*, **54**, 468–480.

Rees, B. (1976). *Acta Cryst. A*, **32**, 483–488.

Rees, B. & Mitschler, A. (1976). *J. Am. Chem. Soc.* **98**(25), 7918–7924.

Sakata, M. & Sato, M. (1990). *Acta Cryst. A*, **46**, 263–270.

Sakata, M. & Takata, M., (1994). MEND. Nagoya Univ., Japan.

Sakata, M., Uno, T. & Takata, M. (1993). *J. Appl. Cryst.* **26**, 159–165.

Saunders, M., Fox, A. G. & Midgley, P. A. (1999). *Acta Cryst. A*, **55**, 471–479.

Schneider, J. R. (1976). *J. Appl. Cryst.* **9**, 394–402.

Schneider, J. R., Hansen, N. K. & Kretschmer, H. (1981). *Acta Cryst. A*, **37**, 711–722.

Smart, D. J. & Humphreys, C. J. (1980). In *Inst. Phys. Conf. Ser.*, 52, pp. 211–214. London, Bristol: The Institute of Physics.

Spence, J. C. H. & Zuo, J. M. (1992). *Electron Microdiffraction*. Plenum Press, New York.

Su, Z. & Coppens, P. (1997). *Acta Cryst. A*, **53**, 749–762.

Svensson, E. C., Brockhouse, B. N. & Rowe, J. M. (1969). *Phys. Rev.* **155**, 619–632.

Tabbernor, M. A., Fox, A. F. & Fisher, R. M. (1990). *Acta Cryst. A*, **46**, 165–170.

Takama, T. & Sato, S. (1982). *Philos. Mag. B*, **44(6)**, 615–626.

Temkin, R. J., Henrich, V. E. & Raccah, P. M. (1972). *Phys. Rev. B*, **6**, 3572–3581.

Zuo, J. M. (1998). *Materials Transaction, JIM*, **39**, 938–946.

Table 1
Theoretical and experimental static lattice scattering factors for Cu. The row labeled "combined" is the same as this experiment, but with the missing values replaced by the corrected γ-ray data. The agreement factors $R_{\text{this exp.}}$ and R_{combined} are given by $R = \left(\sum |F - F^{\text{ref}}|\right) / \sum F^{\text{ref}}$ and shows the agreement with the this experiment and the combined data, respectively.

			Bagayoko		Schneider *et al.* (1981)			Saunders	This			
			et al.		Original		Corrected	*et al.*	experiment			Multipole
h k l	$\sin\theta/\lambda$	IAM[a]	(1980)	DFT[b]	values	Δ[c]	values[d]	(1999)	(2003)	Combined	MEM	analysis
1 1 1	0.24	22.05	21.68	21.70	21.51(4)	-0.06	21.73(5)	21.78(2)	21.69(3)	21.69(3)	21.84	21.70
2 0 0	0.28	20.69	20.35	20.38	20.22(3)	-0.07	20.44(4)	20.44(2)	20.44(2)	20.44(2)	20.47	20.42
2 2 0	0.39	16.74	16.62	16.67	16.45(4)	-0.08	16.63(5)	16.72(11)	16.68(2)	16.68(2)	16.70	16.69
3 1 1	0.46	14.74	14.70	14.75	14.54(3)	-0.08	14.70(4)	14.78(13)	14.73(1)	14.73(1)	14.72	14.75
2 2 2	0.48	14.19	14.17	14.21	14.07(4)	-0.08	14.22(5)		14.24(7)	14.24(7)	14.20	14.21
4 0 0	0.56	12.42	12.42	12.48	12.29(5)	-0.08	12.42(6)		12.45(9)	12.45(9)	12.43	12.46
3 3 1	0.60	11.42	11.41	11.47	11.30[e]	-0.09	11.43(9)			11.43(9)	11.42	11.46
4 2 0	0.62	11.13	11.13	11.19	11.02(5)	-0.09	11.14(10)		11.18(9)	11.18(9)	11.14	11.16
4 2 2	0.68	10.16	10.16	10.21	10.08(5)	-0.09	10.19(10)			10.19(10)	10.16	10.19
3 3 3	0.72	9.58	9.58	9.63	9.49(5)	-0.09	9.59(9)			9.59(9)	9.58	9.61
5 1 1	0.72	9.58	9.58	9.64	9.53(5)	-0.09	9.63(9)			9.63(9)	9.58	9.61
4 4 0	0.78	8.82		8.86	8.84(7)	-0.09	8.93(11)		8.85(2)	8.85(2)	8.84	8.85
6 0 0	0.83	8.35		8.40	8.37(8)	-0.09	8.45(11)			8.45(11)	8.36	8.37
4 4 4	0.96	7.38		7.40	7.33(8)	-0.09	7.39(12)			7.39(12)	7.38	7.40
8 0 0	1.11	6.64		6.66	6.75(13)	-0.09	6.78(16)			6.78(16)	6.65	6.64
6 6 0	1.18	6.37		6.37	6.41(11)	-0.09	6.43(15)			6.43(15)	6.38	6.37
5 5 5	1.20	6.28		6.27	6.29(12)	-0.09	6.31(15)			6.31(15)	6.29	6.29
10 0 0	1.39	5.66		5.65	5.59(14)	-0.09	5.58(17)			5.58(17)	5.65	5.64
6 6 6	1.44	5.49		5.49	5.51(15)	-0.09	5.49(19)			5.49(19)	5.49	5.49
8 8 0	1.57	5.09		5.09	5.12(16)	-0.09	5.08(20)			5.08(20)	5.09	5.10
$R_{\text{this exp.}}$ (%)		0.69	0.31	0.15	1.09		0.24	0.24	—		0.27	0.10
R_{combined}(%)		0.64	0.30	0.30	0.96		0.14	0.24		—	0.38	0.27

[a] Calculated from Doyle & Turner (1968).
[b] Calculated with the WIEN2k program of Blaha *et al.* (2001).
[c] Kinematic correction of the γ-ray structure factors from Petrillo *et al.* (1998).
[d] Estimated standard deviations are from Petrillo *et al.* (1998).
[e] Estimated by interpolation.

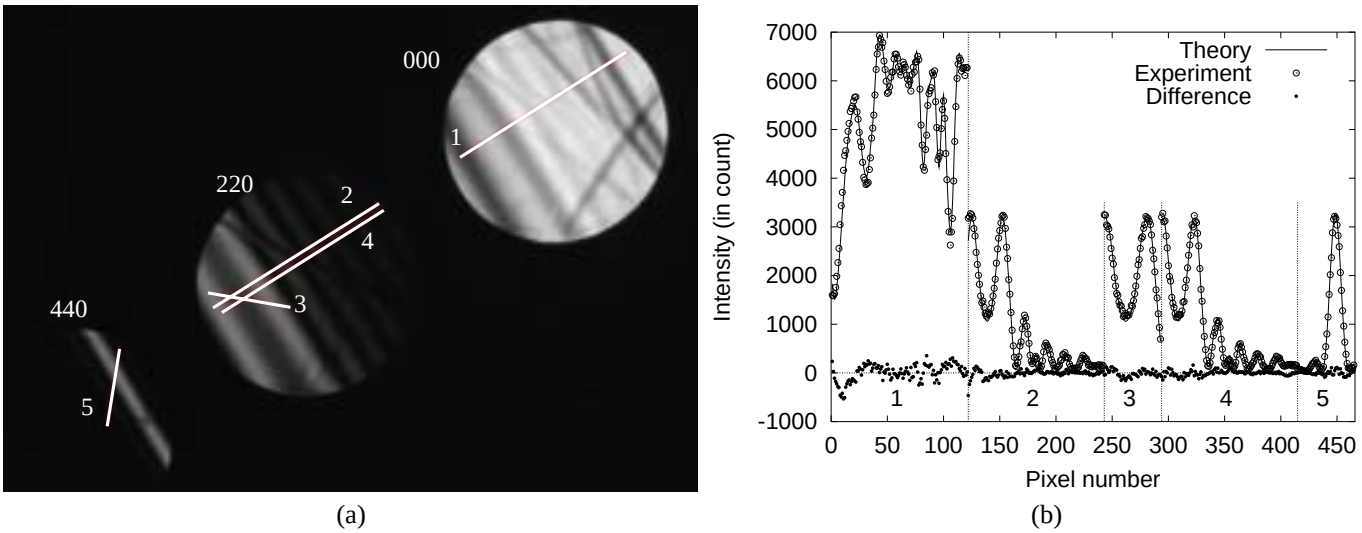

(a) (b)

Figure 1
(a) CBED pattern of the (220) systematic row in copper. The selected rocking curves are shown with white lines. (b) Best fit from Bloch-wave refinement of the selected rocking curves. The points are measured intensities while the solid line is calculated intensities. The discrepancy for each pixel between theory and experiment is also shown with dots.

IUCr macros version 2.0/β10: 2002/12/11 November 5, 2003

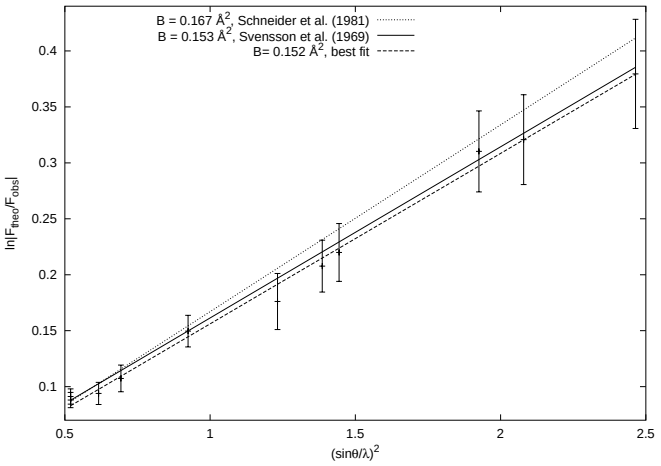

Figure 2
Wilson plot of the Δ-corrected γ-ray data at 50 K. The theoretical structure factors are taken from DFT calculations. The Debye-Waller factor *B*, scaling factor *k* and correlation coefficient *R* are shown for the best fit (dashed line), the used values (solid line) and Schneider *et al.* (1981) original values (dotted line), respectively. When only considering the nine highest orders *B* becomes 0.154 Å^2 for the best fit.

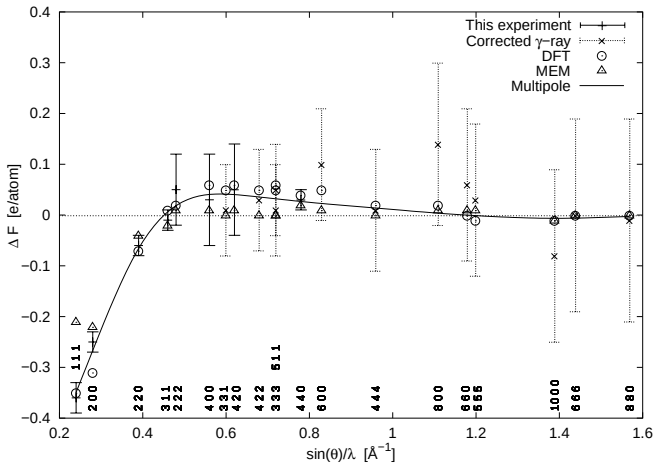

Figure 3
The difference between static lattice scattering factors and Doyle & Turner (1968) independent atom values versus scattering angle. Units in e/atom. The solid line is for the multipole analysis.

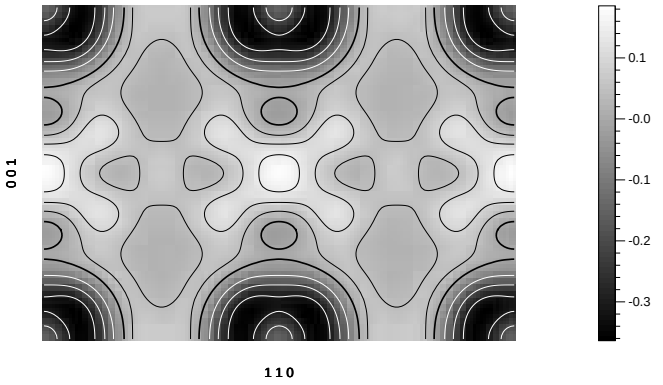

Figure 4
Electron deformation density calculated from the combined data set for $\sin\theta/\lambda \leq 0.79$ Å^{-1}. Zero is marked with a thick black contour line. Negative contours (white) are drawn with intervals of 0.1 eÅ^{-3} and positive contours (thin black) are drawn with intervals of 0.05 eÅ^{-3}.

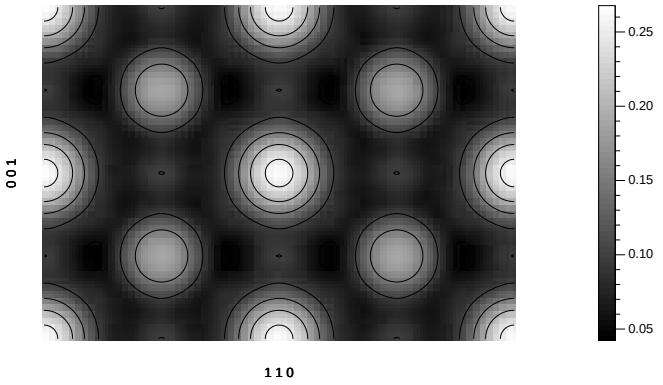

Figure 5
Standard deviation in the deformation density calculated from the combined data set, $\sin\theta/\lambda \leq 0.79$ Å^{-1}. Contour intervals are 0.05 eÅ^{-3}.

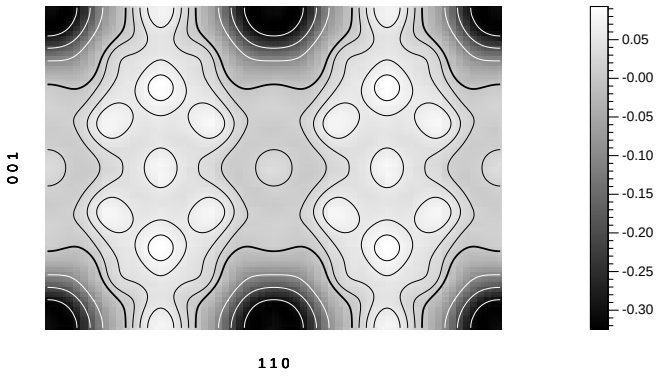

Figure 6
The deformation density from a two-channel MEM simulation. Zero level is marked with a thick black contour. Negative contours are at intervals of 0.05 eÅ^{-3} and positive at intervals of 0.02 eÅ^{-3}.

IUCr macros version 2.0/β10: 2002/12/11 November 5, 2003

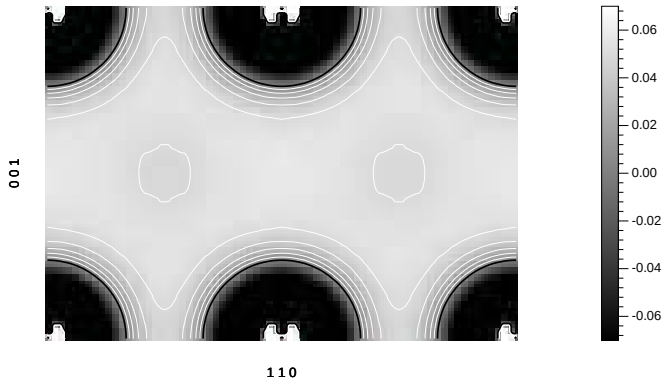

Figure 7
The deformation density of the (110) plane from multipole analysis. Note the small contour intervals of 0.002 eÅ^{-3}. The difference density is 0.081 eÅ^{-3} at the small local minimum in the octahedral sites, while it is close to 0.090 eÅ^{-3} in the rest of the interstitial region.

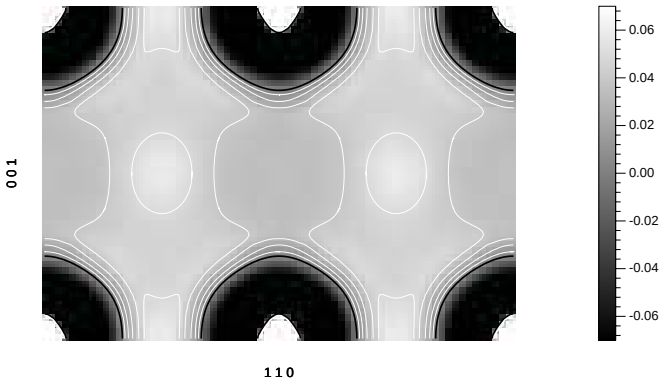

Figure 8
The deformation density of the (110) plane calculated from density functional theory. Negative contours (white) are at intervals of 0.1 eÅ^{-3} and positive contours (fine black) are at intervals 0.01 eÅ^{-3}.

Synopsis

A study of charge density in copper from combination of QCBED and γ-ray diffractometry structure factors.

IUCr macros version 2.0/β10: 2002/12/11 November 5, 2003

Paper 6

Electron Density and Implication for Bonding in Cu and Ag

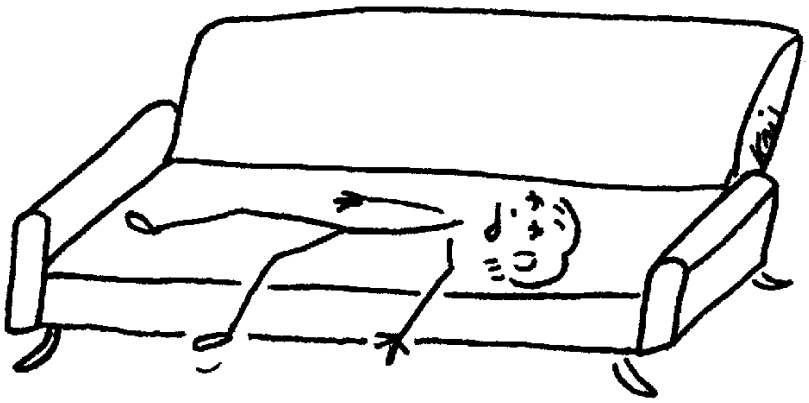

Electron Density and Implication for Bonding in Cu and Ag

B. Jiang[1*], J. Friis[2], R. Holmestad[2], J. M. Zuo[3], M. O'Keeffe[4] and J. C. H. Spence[1]

1 Department of Physics & Astronomy, Arizona State University, Tempe, AZ 85281, USA

2 Department of Physics, Norwegian University of Science and Technology (NTNU), 7491 Trondheim, Norway

3 Department of Material Science & Engineering, University of Illinois, Urbana, IL 61801, USA

4 Department of Chemistry, Arizona State University, Tempe, AZ 85287, USA

** Email: jiangb@asu.edu*

PACS number : 71.20.Be, 32.80.Cy, 95.30.Ky, 71.15.Mb

ABSTRACT

We report highly accurate measurements for the low-order Fourier components of the electron density in copper. These were obtained by transmission electron diffraction using a small probe and multiple scattering analysis. They were used to refine the Cu 3*d* radial wave function. An accurate charge-deformation map and a 3*d* orbital radial wave function were obtained by using a multipole refinement of the structure factors obtained from combined quantitative electron diffraction and ν-ray diffraction measurements. The results show a large change in the 3*d* orbital radial function from *d*-band formation and *d-s* band crossing (*d-s* hybridization). Band theory calculations are in excellent agreement with the measurements and show that the charge deformation in Ag is very similar to that in Cu Our findings are in general agreement with the monovalent description of these metals.

I Introduction

The measurement of valence electron radial wave functions and charge densities has long been recognized as a challenging problem. It requires highly accurate Fourier components of charge density and a sound multipole refinement model. The Fourier components of charge density are equal to the X-ray structure factors, whose amplitude, in principle, can be obtained experimentally by measuring the diffraction intensities. In simple inorganic materials like copper, it is difficult to obtain the crucial low-order structure factors by kinematic photon (X-ray or ν-ray) diffraction with sufficient accuracy for charge density analysis due to uncertainties in extinction corrections and other factors [1]. Electron diffraction, on the other hand, is inherently more sensitive for small scattering vectors and is free from extinction effects, so that low order structure factors can be obtained with much higher accuracy [1] . Using a combination of electron (for low order) and X-ray (for higher order) diffraction data, detailed information about the valence electron distributions has recently been obtained in simple inorganic crystals such as Cu [2], Mg [3], MgO [4], TiO_2 [5], Cu_2O [6].

First-principles electronic structure calculations provide an excellent account of properties such as cohesive energy, interatomic distances and elastic properties for metals like copper [7] but there is no unambiguous (and hence meaningful) direct way to project out orbital occupancies and wave function from plane-wave calculations. In contrast the analysis of experimental electron densities in crystals is very often made using a pseudoatom (multipole) fitting which approximates crystal charge density based on single-electron orbital radial wave functions and occupancies [8]. This simple model has

been found experimentally sufficient flexible to describe charge density in a variety of crystals.

Here we present our recent results on Cu and Ag, using experimental electron diffraction, band theory calculations, and multipole analysis. We find that a large change in the *d*-orbital radial wave function is required in the multipole model to account for the differences in X-ray structure factors of crystals and that obtained by superimposing spherical atoms. Brewer's hypothesis [9], that the binding energy per electron is approximately constant for metals, is also discussed.

II Method

In the multipole model, the atomic charge density in a crystal is expanded into three parts; the spherical inner-shell electrons (core electrons), spherical valence shells (monopoles), and a series of nucleus-centered local symmetry-adapted spherical harmonic functions which reflect the small but important non-spherical valence charge distribution (higher order multipoles) . The X-ray structure factors are fitted by adjusting the refinement parameters (monopoles and multipoles). Following Hansen and Coppens [10], the charge of a pseudoatom is described as:

$$\psi_{pseudoatom}(\vec{r}) = P_c * \psi_{core}(r) + P_v * \rho^3 * \psi_{valence}(\rho r) + \sum_{l=1}^{l_{\max}} \zeta_l^3 R_l(\zeta_l r) \sum_{m=0}^{l} P_{lm} d_{lm\partial}(\chi,\lambda) \qquad (1)$$

The first and second terms represent the spherical atomic core, which is well-described by atomic modelling and is fixed in our multipole refinement, and the spherical (monopole) valence charge density, respectively. The third term is a summation over the

multipoles. It should be noted that first two terms are real charge densities, while the third term only redistributes valence density non-spherically in real space. The volume integration of this term is zero. Slater type orbitals (STO) calculated by Su *et al* [11] were used for the density functions of the core, $\psi_{core}(r)$, and valence electron monopole, $\psi_{valence}(\rho r)$. The valence shell can be further divided into two monopoles to simulate the charge transfer between different orbitals on the same atom site (orbital hybridization effect) or orbital deformation effect. The multipole radial functions, $R_l(\zeta r)$, are calculated using single exponential functions, or an atomic orbital product. The refined parameters are the valence electron population, P_v, and its radial function scaling factor, ρ , and the multipole populations, $P_{lm\partial}$, and their radial function scaling factors, ζ_l. In the copper refinement, the radial function of the hexadecapole is constructed from a 3*d**3*d* orbital wave function. In this case, the radial scaling factor ρ will be refined. This simple model can produce meaningful information on bonding, as demonstrated in several cases, such as TiO_2, MgO, Cu_2O and Si [4-6, 12].

Accurate measurements of the low-order structure factors were made using the quantitative convergent-beam electron diffraction technique (QCBED) that we have developed recently[13]. The experiment was performed using a LEO-912 in-column T-energy-filtering transmission electron microscope (TEM) with a Gatan liquid nitrogen cooled sample holder. The TEM specimen used is a Cu foil sample prepared by electrolytic polishing and cooled down to 105 K to reduce phonon scattering. The electron illumination heating effect is considered and refined to be about 5 K [2]. A 10 eV energy-filtering slit was placed around the zero-loss peak to remove the contribution from inelastically scattered electrons, which form a background due to plasmon and other loss

processes. Off-zone-axis systematic diffraction patterns were collected for seven low order reflections and recorded on a Gatan CCD camera. The "Extal" software package [13] was used for CBED refinement – this takes full account of multiple scattering and "absorption" in Bloch-wave formalism. The small electron probe size (about 10nm diameter) ensures that the data are collected within a single mosaic block.

Band theory calculations were performed using the augmented plane wave plus local orbital method (APW+lo) [14], as implemented in the program Wien2K [15]. Exchange and correlation effects are treated within density functional theory, using the generalized gradient approximation (GGA) [16]. A muffin tin radius of 2.3 au is used for Cu and Ag.

III Results and Discussion.

We have measured seven low order structure factors for copper using QCBED. These are reported in table 1. Also reported in the table are the results of band theory calculation and multipole models. It is seen that theory and experiment are in excellent agreement. This is an important observation as the experimental results come with (small) error bars and they thus serve to provide limits to the possible error of the theory.

The QCBED data were merged with ν-ray diffraction results [17] for higher orders (where the electron diffraction is less accurate) and subject to multipole refinement using the program VALRAY [18]. The refinement parameters are the electron populations in the valence shell orbitals (monopoles), one cubic hexadecapole, with corresponding radial scaling parameters [11, 19]. It is seen from table 1 that there are significant differences between the multipole fits and QCBED/theory for low orders. To understand the origin of

these differences, the scattering factors of Cu orbitals are plotted in figure 1. We see that the 4*s* orbital affects reflections below s = 0.2 Å^{-1} ($s=sin\chi/\varsigma$ is the scattering vector), and contributes to small negative values between s=0.2 and s=0.4, while the 3*d* orbital contributes at higher scattering angles up to s=0.8. This analysis suggests that the differences in the X-ray structure factors for (111) (s=0.24 Å^{-1}), (200), (220) and (310) cannot be attributed to changes in the 4*s* orbital. A large deformation in the 3*d* orbital radial wave function must be responsible for these differences. To find a suitable model for multipole refinement, we see that for the low order reflections, the measured X-ray structure factors are systematically lower than those for neutral atoms, indicating partial delocalization of the 3*d* orbital. We suggest that the 3*d* orbital radial wave-function has a tail that does not contribute significantly to the measured reflections, and we use additional occupancy of the Cu 4*s* orbital to simulate this effect. Thus the 3*d* radial wave function in copper is written as $3d_{deformed}=3d^{10-n}4s^{n}$ (n is a refinement parameter) with small changes in the radial scaling factors to simulate 3*d* radial wave-function deformation effects.

This proved to be a good approximation, as shown by the multipole refinement results given in table 1. The results are given for a $3d^{10}4s$ model (only radial scale parameters are refined); for a $3d_{deformed}{}^{10}4s$ model (refinement considering 3*d* orbital deformation), and an agreement index *R*-factor (residual), calculated from the seven QCBED measurements alone. It is found that $3d_{deformed}$ constructed from the *d* orbital of the d^{9} electron configuration (3*d* orbital in Cu^{+2} ion) produces a better fit in multipole refinement, indicating that the localized 3*d* orbitals are more like 3*d* orbitals in Cu^{+2} ions, due to the reduced screening effect of delocalized 3*d* electrons. For the $3d^{10}4s$ model, R =

0.64 % and the fit is outside the range of experimental error (note especially (111) and (200)). For the $3d_{deformd}^{10}4s$ model, R = 0.08 % (ten times less) and all calculated values agree with experiment within experimental errors. The refined value of n is 1.27(6) (in table 2).

The resulting valence charge density difference map shown in figure 2 shows a spherical charge deficiency region (0.9Å in radius) around the copper atom and a charge surplus region between atoms. The charge surplus in the interstitial region is about 0.05 e/Å^3, or a 25% increase in valence electron density. Note the small hexadecapole population, which indicates a very small nonspherical charge deformation (see Table 2). Charge redistribution due to this is less than 10^{-6} e/Å^3 between nearest-neighbor atoms, much smaller than the valence electron density, which is about 0.2 e/Å^3. Thus, the covalent contribution to bonding can be neglected. This finding agrees with the theoretical result of Ogata *et al* [7], who concluded that Cu has a homogeneous charge distribution with little bond directionality.

There are two possible interpretations of the refined number n. Brewer [9] has proposed that the electronic configuration in copper is $3d^{10-n}4s^{1}4p^{n}$, with n=1.5. This hypothesis, with 3*d* electrons being promoted into 4*p* free-electron-like orbitals, is used to explain the strong cohesion in noble metals, such as Cu, Ag, Au, but has been questioned by several researchers [20]. This first possible explanation of our refinement would assume *dsp* hybridization, with 1.27 electrons 'promoted' from the 3*d* to the 4*sp* orbital. However, owing to the e_g and t_{2g} energy splitting (about 1 eV), in that case the charge deformation density would be non-spherical, there would be high-intensity white lines in L_3-edge electron energy-loss spectra (EELS) and X-ray absorption spectra (XAS); and the 3*d*

orbital holes would be expected to give rise to magnetic properties similar to those of the earlier 3 *d* metals. However experimental results show that EELS and XAS spectra have no white lines [21], copper is a weakly diamagnetic metal [20] and our charge density refinement shows a spherical deformation density. The ratio of the e_g and t_{2g} orbital electron populations is $\frac{1.99994(14)}{3}$ calculated from multipole population [8], equal to $\frac{4}{6}$ within error, thus, none-spherical charge deformation is negligible, in strong contrast to the very non-spherical distribution found for the formal d^{10} shell of Cu in Cu_2O [6]. Further evidence in support of a monovalent model in copper comes from the free electron plasma oscillations. The number of free electrons per atom contributing to the plasmon is 1.04(4), (where m^* is the electron effective mass and E_p is the plasmon energy), as calculated using the free electron model from the first plasmon energy using (E_p = 9.3 eV from measured optical properties and the free electron mass) [22]. This is in agreement with a monovalent description of Cu. An additional plasmon peak, however, also occurs at E_p = 19.3 eV, (not due to double scattering) [23], and if we use the free-electron plasmon model we then obtain 3.4 electrons per atom contributing to the bulk plasmon from this second peak. These 3.4 electrons may however stem from the relatively delocalized 3*d* electrons. The two volume plasmon energies in copper thus reflect the different properties of free electrons, and those of delocalized 3d electrons.

The second interpretation possible is that the Cu 3*d* orbital has large deformation, and so becomes much more diffuse compared with the neutral-atom ground state 3*d* orbital. Multipole refinement quantitatively measures the 3d-band orbital radial wave function in Cu, which is shown in figure 3. It is constructed from the $3d^{10-n}4s^n$ electron

configuration (with ρ_{3d}=1.006, ρ_{4s}=1.1, see table 2). We see that the 3*d* orbital in Cu has a long tail, and electrons are delocalized. Experimental Slater orbital parameters were fitted and are given in table 3. This kind of deformation cannot be simulated by refining radial scaling factors alone in the multipole model. That is the reason for the failure of the ground state neutral-atom model. It has been proposed that 3*d* band electrons contribute substantially to the cohesive energy of Cu by *d-s* orbital hybridization [24]. Thus of the total cohesive energy of 0.26 Ry, the calculated contribution from the 4s band is 0.11 Ry and thus *d-s* orbital hybridization contributes significantly to the cohesive energy of Cu (Note that renormalization energy is -0.4 Ry for Cu, therefore, *d-s* orbital hybridization contributes 0.19 Ry) [24].

We have also completed a multipole refinement for silver, to measure the 4*d* orbital deformation. Calculated X-ray structure factors were used and refined using similar refinement procedures. The results are listed in table 2. We conclude that charge deformation is again spherical (from the small multipole population) and the 4*d* orbital in silver has a similar amount of deformation to the 3*d* orbital in copper. The ratio of the e_g and t_{2g} orbital electron populations is, and again the charge deformation is very close to spherical. The Ag 4*d* orbital radial wave function is shown in figure 3 and the Slater orbital parameters are given in table 3. The number of free electrons, from the plasmon energy (E_p = 9.2 eV) is 1.0 [23]. We conclude that Ag is a monovalent metal.

It is important to point out that the orbital radial wave functions are deduced from the charge density refinement based on an atomic model. It is well known however, that electrons form bands in crystals and so loose their individuality. Our refinement thus provides an example of how a one-electron model can nevertheless retains useful validity

in the transition metals. We expect that this method can also be used in the transition metal compounds, where valence *d* orbitals form *d*-bands.

IV Summary

Accurate low order X-ray structure factors have been measured for copper by quantitative convergent beam electron diffraction. Charge density deformation maps refined using a multipole model show a spherical charge deformation in copper and silver. Valence *d* orbital radial wave functions obtained from multipole refinement, show a large deformation when compared with neutral atoms. Results support the monovalent metal model in Cu and Ag.

Funded by DOE DE-FG03-02ER45596 (JCHS P.I.). J. Friis funded by Research Council of Norway (NFR), project 135270/410. Thanks to Dr. P. Rez (ASU) and Dr. P. Blaha (Vienna Tech.) for helpful discussions.

Table 1. Measured (QCBED) and calculated structure factors for Cu. The column headed $3d^{10}4s$ is a multipole refinement with fixed orbital occupation; the column headed $3d_{deformed}{}^{10}4s$ ($3d_{deformed} = 3d^{10-n}4s^{n}$ with 3d orbital wave function from Cu^{2+} and 4s from neutral atom, and gives the best refined value of n=1.27). The residual R calculated for the seven structure factors listed shows the agreement of theory with QCBED experiment. The experimental structure factors are converted to their 0K static value.

hkl or R	$s=\sin(\chi)/\varsigma$	QCBED	Theory (CGA)	Neutral atom	$3d^{10}4s$	$3d_{deformed}{}^{10}4s$
111	0.240	86.76 (16)	86.80	88.18	87.94	86.81
200	0.278	81.76 (16)	81.52	82.71	82.47	81.67
220	0.393	66.72 (12)	66.70	66.99	66.74	66.75
311	0.460	58.94 (08)	59.02	59.00	58.77	58.99
222	0.481	56.96 (32)	56.89	56.80	56.58	56.84
400	0.555	49.80 (40)	49.93	49.68	49.49	49.82
440	0.785	35.41 (16)	35.44	35.27	35.17	35.40
R (%)			0.15	0.71	0.64	0.08

Table 2. Multipole refinement results for Cu and Ag. Refinements use the ion core plus *d* orbital from a d^9 configuration (*d*-orbital in Cu^{+2} or Ag^{+2} ion) and 4*s* or 5*s* orbitals from neutral atoms. Multipoles up to forth-order are chosen for refinement. The allowed multipoles are selected according to the index-picking rules of Kurki-Suonio [19]. The *d*-orbital deformation is included in the refinement (by refining *n*). The 4*s* or 5*s* electron population (P_s) is fixed at one. The corresponding kappa for monopoles or multipole is refined. (Note, Dawson normalization is used for multipole populations, see VALRAY manual for details [18].)

Parameters	Cu	Ag
$P_d = (10-n)$	8.73(6)	8.65(1)
$\rho_d = \rho_4$	1.006(5)	1.0083(7)
ρ_s	1.1(1)	1.15(1)
P_{hex}	-0.0001(2)	0.024(6)
R	0.06%	0.02%

Table 3 Slater orbital parameters of Cu 3*d* and Ag 4*d* radial wave functions. Radial wave function $R_{nl}(r)$ is defined by

$$R_{nl}(r) = \sum_i c_i \theta_i(r)$$

where,

$$\theta_i(r) = (2n_i!)^{-1/2} (2z_i)^{n_i+1/2} r^{n_i-1} e^{-z_i r}$$

See Clementi *et al* [25] for details.

Crystal	Parameters	Values
Cu	n	3 3 3 3 3
	c	0.02947 0.15822 0.52916 0.33576 0.23600
	z	1.80063 9.01160 4.81177 2.37701 0.91309
Ag	n	3 3 3 3 4 4 4 4
	c	0.00632 0.09693 0.30863 -0.45737 0.07110 -0.55814 -0.30714 -0.10501
	z	34.01846 15.42014 7.71913 5.10149 13.67176 3.49371 1.70772 0.80052

Figure 1 Scattering factors of Cu 3*d* and 4*s* orbitals. The scattering angles of lowest order reflections are shown. Note the contribution to these reflections from 4s orbital is small.

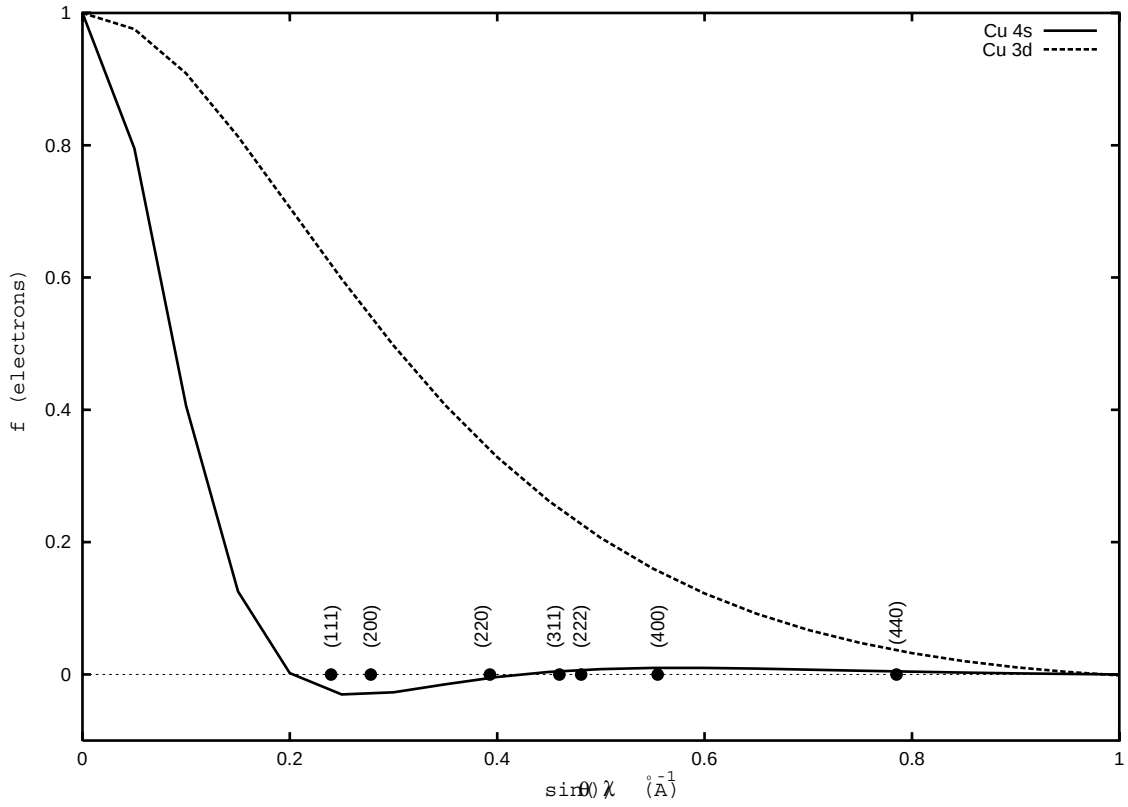

Figure 2. Valence charge density deformation map on the (110) plane of copper. The map shows the difference between an experimental charge density and a neutral atom model as reference. The dashed lines are for contours with $\div\psi < 0$, the solid lines are for contours with $\div\psi > 0$, the increment between contours is 0.01e/Å^3.

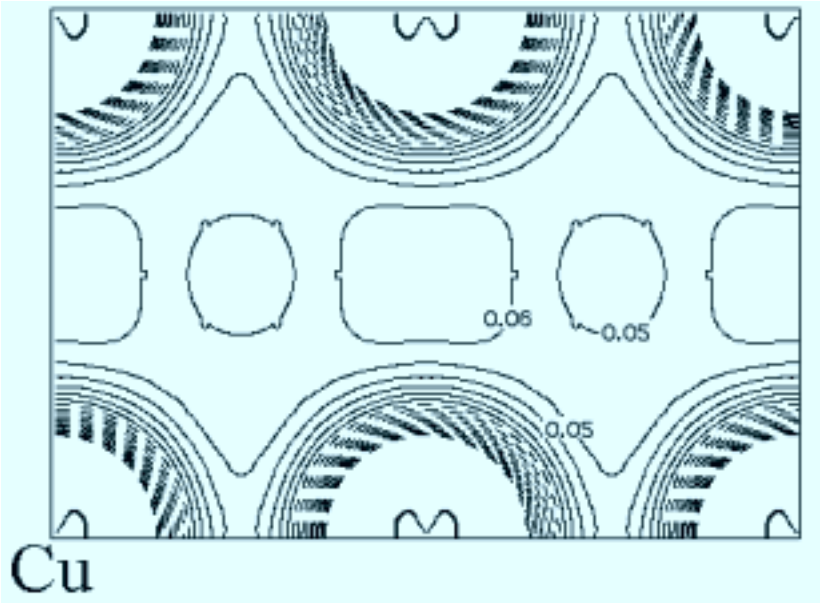

Figure 3 Cu 3*d* and Ag 4*d* orbital radial wave functions. It is seen that valence *d* orbitals in the crystal spread outward, owing to *d*-band formation and d-s band hybridization. This kind of deformation can not be simulated by refining scaling parameters in the multipole model. (Note, the charge density peak of 4*s* or 5*s* orbitals at nuclear center is omitted to construct 3*d* or 4*d* orbitals to conform to the requirement that *d* orbital approach zero at nuclear center. It has negligible effect on scattering factor.)

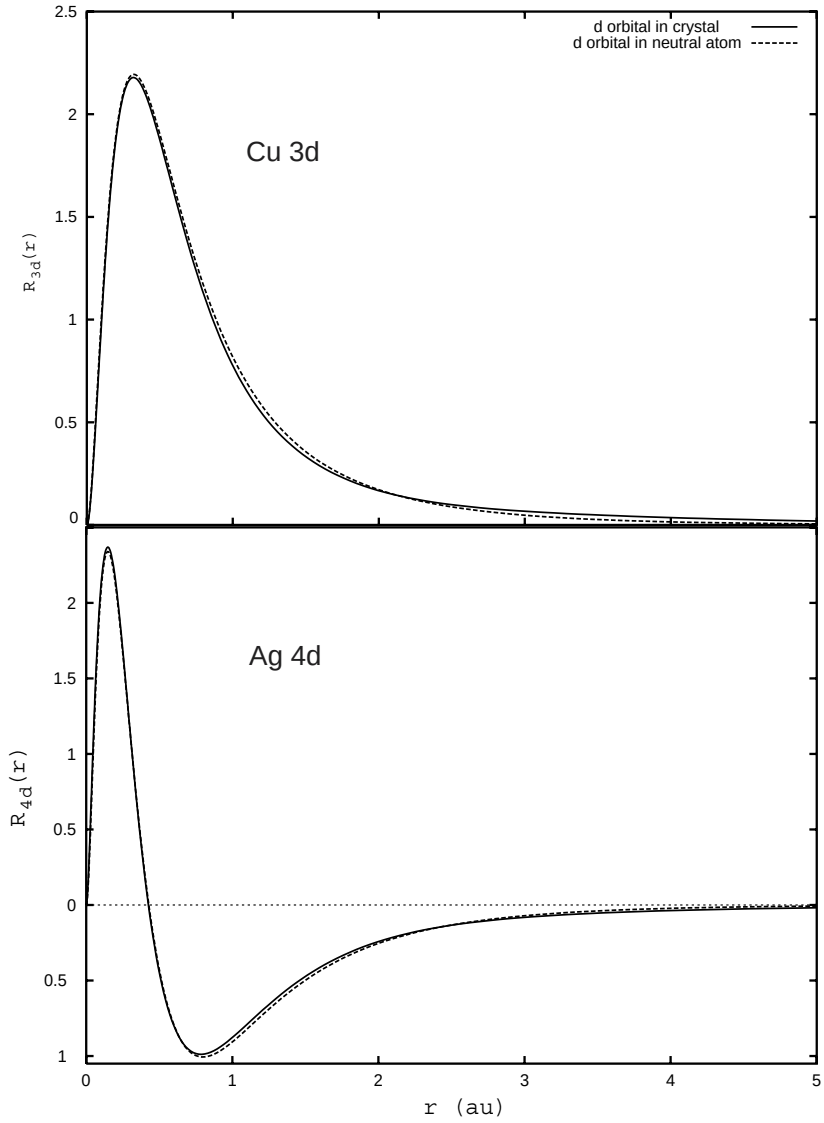

References

[1] B. Jiang, J. M. Zuo, Q. Chen, and J. C. H. Spence, Acta. Cryst. **A58**, 4 (2002).

[2] J. Friis, B. Jiang, J. C. H. Spence, and R. Holmestad, Micros. and Microanal. **9**, 379 (2003).

[3] J. Friis, G. H. K. Madsen, F. K. Larsen, B. Jiang, K. Martinsen, and R. Holmestad, J. Chem. Phys., in press (2003).

[4] J. M. Zuo, M. O'Keeffe, P. Rez, and J. C. H. Spence, Phys. Rev. Lett. **78**, 4777 (1997).

[5] B. Jiang, J. M. Zuo, N. Jiang, M. O'Keeffe, and J. C. H. Spence, Acta Cryst. **A59**, 341 (2003).

[6] J. M. Zuo, M. Kim, M. O'Keeffe, and J. C. H. Spence, Nature **401**, 49 (1999).

[7] S. Ogata, J. Li, and S. Yip, Science **298**, 807 (2002).

[8] P. Coppens, *X-ray Charge Densities and Chemical Bonding* (Oxford University Press, 1997).

[9] L. Brewer, in *Structure and Bonding in Crystals*, edited by M. O'Keeffe and A. Navrotsky (Academic Press, 1982), Vol. I, p. 143; L. Brewer, Science **161**, 115 (1968).

[10] H. K. Hansen and P. Coppens, Acta. Cryst. **A34**, 909 (1978).

[11] Z. W. Su and P. Coppens, Acta Cryst. **A54**, 646 (1998).

[12] J. M. Zuo, P. Blaha, and K. Schwarz, J. Phys.: Conden. Matt. **9**, 7541 (1997).

[13] J. C. H. Spence and J. M. Zuo, *Electron Microdiffraction* (Plenum Press, 1992); J. M. Zuo, Materials Transaction, JIM. **39**, 938 (1998).

[14] E. Sjostedt, L. Nordstrom, and D. J. Singh, Solid State Comm. **114**, 15 (2000).

[15] K. Schwarz, P. Blaha, and G. K. H. Madsen, Comp. Phys. Commun. **126**, 71 (2002).

[16] J. P. Perdew, K. Burke, and M. Ernzerhof, Phys. Rev. Lett. **77**, 3865 (1996).

[17] C. Petrillo, F. Sacchetti, and G. Mazzone, Acta. Cryst. **A54**, 468 (1998); J. R. Schneider, N. K. Hansen, and K. H., Acta. Cryst. **A37**, 711 (1981).

[18] R. F. Stewart, M. A. Spaceman, and C. Flensburg, *VALRAY User's Manual* (Carnegie Mellon University & University of Copenhagen, 2000).

[19] K. Kurki-Suonio, Isr. J. Chem. **16**, 115 (1977).

[20] W. Hume-Rothery, *The Structure of Metals and Alloys* (Richard Clay (The Chaucer Press), Ltd., London, 1969); P. S. Rudman, J. Stringer, and R. I. Jaffee, in *McGraw-Hill Series in Materials Science* (McGraw-Hill Book Company, Geneva and Villar, Switzerland, 1966).

[21] C. Bonnelle, Ann. Phys. (Paris) **1**, 439 (1966); M. H. Heinonen and J. A. Leiro, Phil. Mag. B **49**, L43 (1984); R. D. Leapman, L. A. Grunes, and P. L. Fejes, Phys. Rev. B **26**, 614 (1982); S. Kiyono, S. Chiba, Y. Hayasi, S. Kato, and S. Mochimaru, Jpn. J. Appl. Phys. S2 **17**, 212 (1978); J. Luitz, M. Maier, C. Hebert, P. Schattschneider, P. Blaha, K. Schwarz, and B. Jouffrey, Eur.Phys.J. **B21**, 363 (2001).

[22] H. Ehrenreich and H. R. Philipp, Phys. Rev. **128**, 1622 (1962).

[23] J. Deniel, C. Festenberg, H. Reather, et al., in *Springer Tracts in Modern Physics*, Springer, New York, 1970), Vol. 54, p. 101.

[24] C. D. Gelatt, H. Ehrenreich, and R. E. Watson, Phys. Rev. B **15**, 1613 (1977).

[25] E. Clementi and C. Roetti, Atomic Data and Nuclear Data Tables **14**, 177 (1974).

Part III

Unpublished results

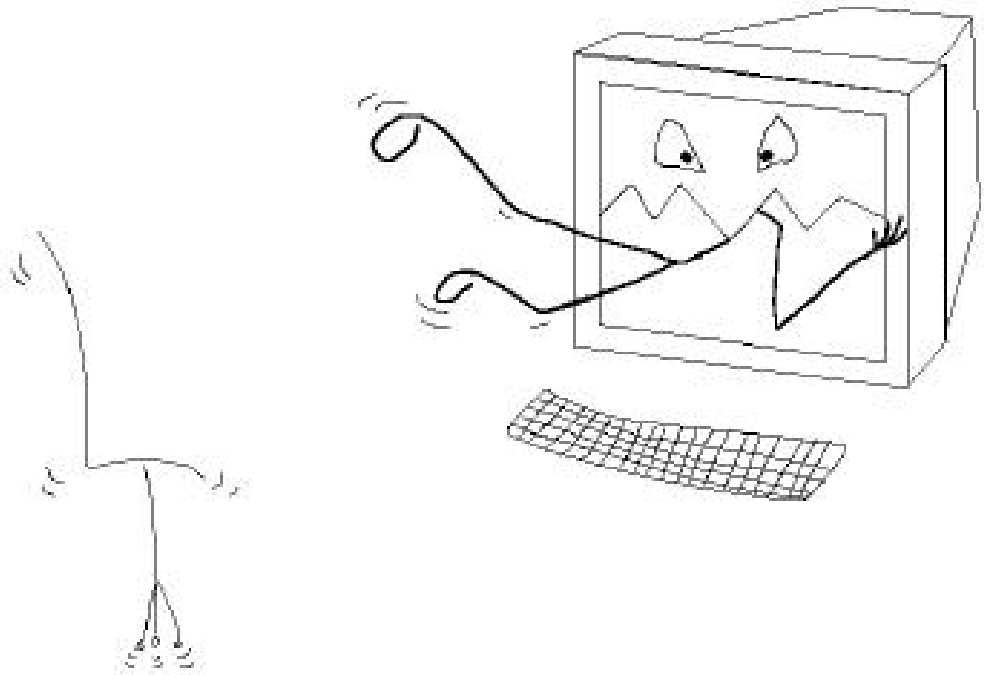

URN:NBN:no-7231

Chapter 1

QCBED measurements of $SrTiO_3$

1.1 Introduction

Strontium titanate ($SrTiO_3$) is a typical perovskite structure, with phase transitions from a cubic to a tetragonal structure at 110 K and from a tetragonal to an orthorhombic structure at 65 K (Table 1.1). A phase transition to a rhombohedral phase may also exist at 10 K. $SrTiO_3$ was intensively studied during the 1960s and 1970s because of the interesting phase-transitions (see e.g. Lytle, 1964; Devanarayanan & Narayanan, 1968; Shirane & Yamada, 1969; Golding, 1970; Blazey, 1971; Willemsen *et al.*, 1976).

Neutron diffraction experiments of $SrTiO_3$ were performed by Hutton *et al.* (1981). The intention of their work was to test the extinction model of Becker & Coppens (1974), but they also provide very accurate anisotropic displacement parameters (ADPs). More recent, quantitative convergent beam electron diffraction (QCBED) experiments have been performed for accu-

Table 1.1: Phases in $SrTiO_3$ when the temperature is lowered from room temperature to 35 K (Lytle, 1964). α is the linear thermal expansion coefficient in the cubic phase.

Temperature range (K)	Structure	Space group	Physical constants
300-110	Cubic	$Pm\bar{3}m$	$\alpha = 9.4 \times 10^{-6}\ K^{-1}$
110-65	Tetragonal	$I4/mcm$	$c/a = 1.00056$
65-35	Orthorhombic		$a : b : c = 0.9998 : 1 : 1.0002$

rate determination of lattice parameters and ADPs of the tetragonal low-temperature phase (Tsuda & Tanaka, 1995).

Since the material has got an important application as substrate for thin film high temperature superconductors, is simple with a small unit cell (around 4 Å), and is well characterized, $SrTiO_3$ seems to be a promising candidate for charge density studies by QCBED. Careful experiments of the cubic phase were performed by Bin Jiang at Arizona State University (ASU) and the experimental data were brought to Trondheim for structure factor refinements and further analysis. During our refinements, Zhurova & Tsirelson (2002) published their charge density studies, based on multipole analysis of X-ray measurements performed by Abramov *et al.* (1995). However, it seems possible to improve these X-ray results, by combining them with the present high-accurate low-order QCBED measurements.

1.2 Experiments

The experiments were performed with the Zeiss 912 electron microscope (operating at 120 kV) at ASU, equipped with an in-column Ω-filter and a 14 bit dynamic range 1k×1k CCD camera. With a liquid nitrogen sample holder, the temperature was kept just above the phase transition at 110 K. Readout temperatures from the holder varied from 108 K to 113 K, but we know by experience (Friis *et al.*, 2003a,b) that the true sample temperature is some degrees higher. There were no evidence that the tetragonal phase was reached in the diffraction patterns. After removing X-ray spots, the CBED patterns were deconvoluted with the LUCY algorithm (Zuo, 1999) in order to compensate for point spreading in the CCD.

1.3 Refinements

For structure factor refinements the high voltage, lattice parameters and ADPs need to be known in advance to high accuracy. The high voltage calibration of the microscope is described in Friis *et al.* (2003a).

1.3.1 Anisotropic displacement parameters

A schematic drawing of the $SrTiO_3$ structure is shown in Fig. 1.1. The Sr and Ti atoms are at cubic site symmetry positions $m\bar{3}m$ while the O atoms have the site symmetry $4/mmm$. Neglecting anharmonicity, the isotropic vibrations of Sr and Ti are therefore described by only one parameter, $2\pi^2 U_{\mathrm{Sr}} = \beta^{11}_{\mathrm{Sr}} = \beta^{22}_{\mathrm{Sr}} = \beta^{33}_{\mathrm{Sr}}$ and $2\pi^2 U_{\mathrm{Ti}} = \beta^{11}_{\mathrm{Ti}} = \beta^{22}_{\mathrm{Ti}} = \beta^{33}_{\mathrm{Ti}}$, respectively, where β denotes

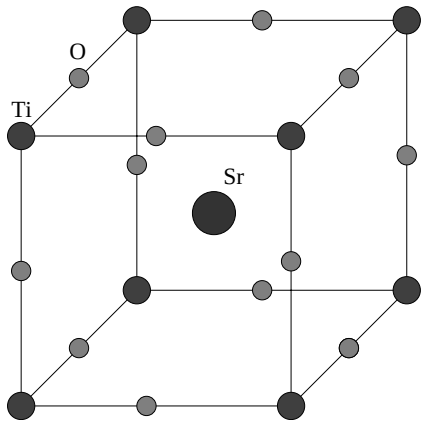

Figure 1.1: Schematic drawing of the $SrTiO_3$ structure.

the anisotropic displacement tensor (see Appendix B.3). The oxygen atoms can vibrate both in the plane spanned by the four closest Sr atoms, U_{O}^1, and along the line between the closest two Ti atoms, U_{O}^2. In the refinements we have used the ADPs found in the neutron diffraction experiment at 112(1) K by Hutton *et al.* (1981). The values of the ADPs derived from this experiment are $U_{\mathrm{Sr}} = 0.00252(5)$ Å^2, $U_{\mathrm{Ti}} = 0.00196(6)$ Å^2, $U_{\mathrm{O}}^1 = 0.00552(5)$ Å^2 and $U_{\mathrm{O}}^2 = 0.00228(5)$ Å^2.

1.3.2 Lattice constant

The lattice constant was determined from refinements of the high order Laue zone (HOLZ) line positions in the center disk, close to the [014]-zone axis. Dynamical calculations of the exact HOLZ-line positions (Zuo *et al.*, 1998), were performed for three areas in the central disk (Fig 1.2). The areas were chosen in order to avoid overlap with neighboring disks and to reduce the influence of low order structure factors, which might be affected by bonding and hence differ from their IAM values. Since only the HOLZ-line positions are of interest, the CBED pattern in Fig 1.2a was made binary using a threshold of 25% of the full image intensity (Fig 1.2b). The refinement was performed in a two step procedure. First, a full-intensity refinement of the experimental parameters (incident beam angle, sample thickness and pattern geometry) was performed. These values were then used as a starting point in the lattice parameter refinement of the binary pattern. The lattice parameter at the goodness-of-fit minimum was $a = 3.89975$ Å. Using this lattice parameter, it might be possible to derive the true experimental temperature, by e.g. comparing with the thermal expansion experiments (Devanarayanan & Narayanan, 1968; Golding, 1970; Willemsen *et al.*, 1976).

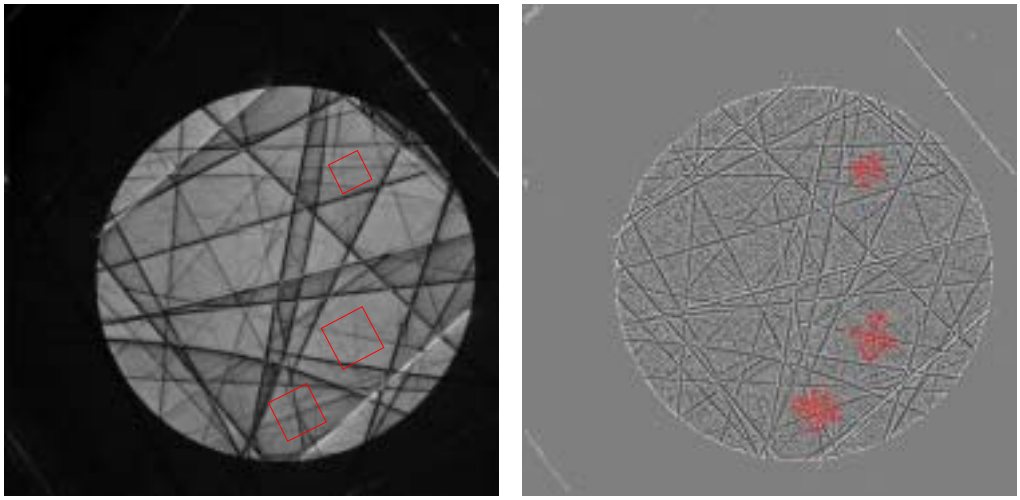

(a) (b)

Figure 1.2: Determination of the lattice constant. (a) CBED pattern of the central disk, close to the [014]-zone axis in $SrTiO_3$. The three areas chosen for lattice parameter refinement are shown. (b) A binary version of the CBED pattern in (a). The calculated HOLZ-line positions are shown in red.

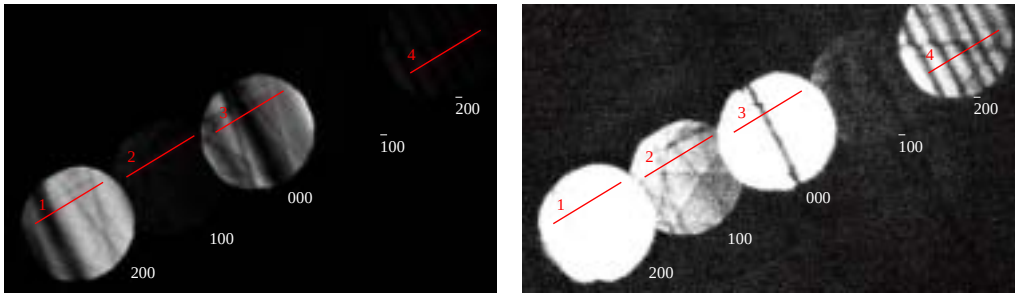

(a) (b)

Figure 1.3: A CBED pattern of the (100) systematic row in $SrTiO_3$. Since the (100) disk is too weak to show up in the full dynamical (color) range (a), the same pattern is also shown in a reduced color range (b). The four line scans used in the refinements are shown in red.

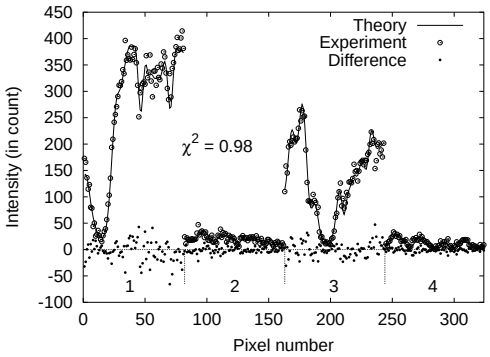

Figure 1.4: Best fit between theoretically calculated intensities (lines) and experiment (circles) after structure factor refinement of the (100) systematic row shown in Fig. 1.3. The differences between theory and experiment are shown with small dots. For this refinement of the (100) and (200) structure factors, 324 pixels were included along four line scans.

1.3.3 Preliminary structure factor refinements

Twelve structure factors have so far been refined. It was even possible to refine the very weak (100) reflection. For this very low order structure factor we had to choose a small condenser aperture in order to avoid overlapping disks. A CBED pattern of the (100) systematic row is shown in Fig. 1.3 with the corresponding best fit between theoretically and experimentally intensities in Fig. 1.4. For the refinement shown Fig. 1.4 we see that the χ^2 is even less than one. This is a much lower value than what is normally obtained with larger condenser aperture (around 1.5). Probably this low value is due to an overestimation of the standard deviation in the pixel intensities, since the characterization of the CCD was performed for an average count at about 3000.

The refined structure factors, converted to their corresponding X-ray values, are listed in Table 1.2 together with structure factors obtained from the independent atom model (IAM), density functional theory (DFT) calculations and the X-ray diffraction experiment used by Zhurova & Tsirelson (2002). Even though these are preliminary results, it is clear that the QCBED and X-ray results differ quite a lot. However, it is interesting to notice that for the weak (100) reflection, for which extinction effects should be small, the agreement between X-ray and QCBED is within one standard deviation. The general agreement of the DFT calculations is also better compared to the QCBED values than to the X-ray values.

Further work on $SrTiO_3$ includes some more independent refinements of

Table 1.2: Preliminary experimental and theoretical static lattice structure factors for the cubic phase of $SrTiO_3$. The IAM values are those of Doyle & Turner (1968) and the DFT values are calculated with WIEN2k (Blaha *et al.*, 2001) using the generalized gradient approximation (GGA) of Perdew *et al.* (1996). The X-ray data are from Zhurova & Tsirelson (2002) and QCBED is the present experiments. n is the number of independent QCBED refinements performed so far for each reflection.

hkl	$\sin\theta/\lambda$	IAM	DFT	X-ray	QCBED	n
100	0.128	7.891	7.801	7.86(5)	7.89(3)	5
110	0.181	42.48	41.06	40.63(10)	40.96(2)	1
111	0.222	29.43	30.38	30.65(10)	30.38(4)	3
200	0.256	56.13	56.51	56.91(14)	56.52(6)	9
211	0.314	34.27	34.14	33.95(8)	34.25(7)	5
220	0.363	45.39	45.41	45.06(11)	45.62(10)	1
310	0.405	30.13	30.30	30.23(7)	29.98(16)	3
311	0.425	19.84	19.77	19.77(5)	19.85(17)	4
222	0.444	39.31	39.31	38.89(10)	39.27(7)	3
321	0.480	27.34	27.42	27.34(6)	27.34(20)	4
400	0.513	35.39	35.52	35.07(10)	35.33(11)	4
422	0.628	30.49	30.54	30.43(7)	30.40(24)	4

the (110)-(220) systematic row and some fine adjustments of the refinements, which seem to have been trapped in local minima. A Wilson plot, based on DFT as a static lattice reference (Friis *et al.*, 2003b), should also be performed in order to check the consistency of ADPs taken from Hutton *et al.* (1981). The QCBED data set could then be combined with the 131 structure factors from Zhurova & Tsirelson (2002) for a multipole refinement. Including our very accurate low order structure factors and by comparing with DFT, it may be possible to describe the bonding in strontium titanate in detail.

References

Abramov, Y. A., Tsirelson, V. G., Zavodnik, V. E., Ivanov, S. A. & Brown, I. D. (1995). The chemical bond and atomic displacements in $SrTiO_3$ from X-ray diffraction analysis. *Acta Cryst. B* **51**, 942–951.

Becker, P. J. & Coppens, P. (1974). Extinction within the limit of validity of the Darwin transfer equations. I. general formalism for primary and

secondary extinction and their applications to spherical crystals. *Acta Cryst. A* **30**, 129–153.

Blaha, P., Schwarz, K., Madsen, G., Kvasnicka, D. & Luitz, J. (2001). *WIEN2k, An Augmented Plane Wave Plus Local Orbitals Program for Calculating Crystal Properties.* Vienna University of Technology, Austria.

Blazey, K. W. (1971). Optical absorbtion edge of $SrTiO_3$ around the 105-k phase transition. *Phys. Rev.* **27**, 146–148.

Devanarayanan, S. & Narayanan, P. S. (1968). Thermal expansion of strontium titanate. *Indian. Pure Appl. Phys* **6**, 714–716.

Doyle, P. A. & Turner, P. S. (1968). Relativistic Hartree-Fock X-ray and electron scattering factors. *Acta Cryst. A* **24**, 390–397.

Friis, J., Jiang, B., Spence, J. C. H. & Holmestad, R. (2003a). Quantitative convergent beam electron diffraction measurements of low order structure factors in copper. *Micros. and Microanal.* **9**, 379–389. Paper 1 in this thesis.

Friis, J., Marthinsen, K. & Holmestad, R. (2003b). Retrieval of anisotropic displacement parameters in Mg from convergent beam electron diffraction experiments. In *EMAG Proceedings. Inst. Phys. Conf. Ser. No. 165.* The University of Oxford, 3-5 Sep. Paper 3 in this thesis.

Golding, B. (1970). Thermal expansivity and ultrasonic propagation near the structural transition of $SrTiO_3$. *Phys. Rev. Lett.* **25**, 1439–1442.

Hutton, J., Nelmes, R. J. & Scheel, H. J. (1981). Extinction corrections for a highly perfect crystal ($SrTiO_3$). *Acta Cryst. A* **37**, 916–920.

Lytle, F. W. (1964). X-ray diffractometry of low-temperature phase transformations on strontium titanate. *J. Appl. Phys.* **35**, 2212–2215.

Perdew, J. P., Burke, K. & Ernzerhof, M. (1996). Generalized gradient approximation made simple. *Phys. Rev. Lett.* **77**, 3865–3868.

Shirane, G. & Yamada, Y. (1969). Lattice-dynamical study of the 110°K phase transition in $SrTiO_3$. *Phys. Rev.* **177**, 858–863.

Tsuda, K. & Tanaka, M. (1995). Refinement of crystal structure parameters using convergent-beam electron diffraction: the low-temperature phase of $SrTiO_3$. *Acta Cryst. B* **51**, 942–951.

Willemsen, H. W., Armstrong, R. L. & Meincke, P. P. M. (1976). Thermal expansion near the displacive phase transition in $SrTiO_3$. *Phys. Rev. B* **14**, 3644–3648.

Zhurova, E. A. & Tsirelson, V. (2002). Electron density and energy density view on the atomic interactions in $SrTiO_3$. *Acta Cryst. B* **58**, 567–575.

Zuo, J. M. (1999). Accurate structure refinement and measurement of crystal charge distribution using convergent beam electron diffraction. *Microscopy Research and Technique* **46**, 220–233.

Zuo, J. M., Kim, M. & Holmestad, R. (1998). A new approach to lattice parameter measurements using dynamic electron diffraction and pattern matching. *Journal of Electron Microscopy* **47**, 121–127.

Part IV

Appendix

URN:NBN:no-7231

Appendix A

Mott formula

A.1 A short derivation of Mott formula taking the thermal motion into account

This derivation of the Mott formula follows the derivation in Spence & Zuo (1992) but treats the thermal motion more rigorous.

The electron atomic scattering factor is defined by

$$f^e(\mathbf{s}) = \mathcal{F}\{V\} = \int V \ \mathrm{e}^{-4\pi i \mathbf{s}\cdot\mathbf{r}} d\mathbf{r} \tag{A.1}$$

where $\mathcal{F}$ denotes the Fourier transform, $V = V(\mathbf{r})$ is the atomic potential and $\mathbf{s}$ is the scattering vector. The thermal average of Eq. (A.1) is given by

$$\begin{aligned}
\langle f^e(\mathbf{s})\rangle &= \int \langle V\rangle \ \mathrm{e}^{-4\pi i \mathbf{s}\cdot\mathbf{r}} d\mathbf{r} \\
&= -\frac{1}{16\pi^2\mathbf{s}^2}\int \langle V\rangle \nabla^2 \mathrm{e}^{-4\pi i \mathbf{s}\cdot\mathbf{r}} d\mathbf{r} \\
&= -\frac{1}{16\pi^2\mathbf{s}^2}\int \left(\nabla^2\langle V\rangle\right) \mathrm{e}^{-4\pi i \mathbf{s}\cdot\mathbf{r}} d\mathbf{r} \\
&= -\frac{1}{16\pi^2\mathbf{s}^2}\int \left\langle \nabla^2 V\right\rangle \ \mathrm{e}^{-4\pi i \mathbf{s}\cdot\mathbf{r}} d\mathbf{r}
\end{aligned} \tag{A.2}$$

where we in the third step have used integration by parts and assumed that $V(\mathbf{r}) \to 0$ when $\mathbf{r} \to \infty$. From Poisson's equation we have

$$\left\langle \nabla^2 V\right\rangle = \left\langle -\frac{|e|}{\epsilon}(\rho_n - \rho)\right\rangle = -\frac{|e|}{\epsilon}\left(\langle\rho_n\rangle - \langle\rho\rangle\right) \tag{A.3}$$

where ρ_n and ρ are the nucleus and electron charge densities, respectively. By inserting Eq. (A.3) into (A.2) we obtain

$$\begin{aligned}\langle f^e(\mathbf{s})\rangle &= \frac{|e|}{16\pi^2\epsilon\mathbf{s}^2}\int(\langle\rho_n\rangle-\langle\rho\rangle)\ \mathrm{e}^{-4\pi i\mathbf{s}\cdot\mathbf{r}}d\mathbf{r}\\ &= \frac{|e|}{16\pi^2\epsilon\mathbf{s}^2}\left[\mathcal{F}\langle\rho_n\rangle-\mathcal{F}\langle\rho\rangle\right]\end{aligned}\tag{A.4}$$

If $\mathbf{u}$ is the thermal displacement of an atom, the time-averaged nucleus density for that atom is[1]

$$\langle\rho_n(\mathbf{r})\rangle=\int Z\delta(\mathbf{r}-\mathbf{u})P(\mathbf{u})\ d\mathbf{u}=ZP(\mathbf{r})\tag{A.5}$$

where $P(\mathbf{u})$ is the displacement probability distribution of the nuclei and Z is the atomic number. The Fourier transform of $\langle\rho_n(\mathbf{r})\rangle$ is then given by

$$\mathcal{F}\langle\rho_n\rangle=ZT(\mathbf{s})\tag{A.6}$$

where $T(\mathbf{s})=\mathcal{F}\{P(\mathbf{u})\}$ is the temperature factor. Inserting Eq. (A.6) into (A.4) yields

$$\langle f^e(\mathbf{s})\rangle=\frac{|e|}{16\pi^2\epsilon\mathbf{s}^2}\left[ZT(\mathbf{s})-\left\langle f^X(\mathbf{s})\right\rangle\right]\tag{A.7}$$

where $f^X(\mathbf{s})=\mathcal{F}\{\rho\}$ is the X-ray scattering factor. By rearranging Eq. (A.7) we obtain

$$\left\langle f^X(\mathbf{s})\right\rangle=ZT(\mathbf{s})-\frac{16\pi^2\epsilon\mathbf{s}^2}{|e|}\left\langle f^e(\mathbf{s})\right\rangle\tag{A.8}$$

We introduce the structure factors

$$\begin{aligned}F_{\mathbf{g}} &= \sum_j\left\langle f^X(\mathbf{s})\right\rangle\ \mathrm{e}^{-2\pi\mathbf{g}\cdot\mathbf{r}_j}\\ V_{\mathbf{g}} &= \frac{1}{\Omega}\sum_j\langle f^e(\mathbf{s})\rangle\ \mathrm{e}^{-2\pi\mathbf{g}\cdot\mathbf{r}_j}=\frac{h^2}{2m|e|}U_{\mathbf{g}}=\frac{h^2}{2m_0\gamma|e|}U_{\mathbf{g}}\end{aligned}\tag{A.9}$$

where $F_{\mathbf{g}}$ and $U_{\mathbf{g}}$ are known as the X-ray structure factor and the electron structure factor, respectively. By multiplying Eq. (A.8) with a phase factor $\mathrm{e}^{-2\pi\mathbf{g}\cdot\mathbf{r}_j}$ and sum over all atoms in the unit cell, we obtain

$$\begin{aligned}F_{\mathbf{g}} &= \sum_j Z_jT_j(\mathbf{s})\ \mathrm{e}^{-2\pi\mathbf{g}\cdot\mathbf{r}}-\frac{16\pi^2\epsilon\Omega\mathbf{s}^2}{|e|}V_{\mathbf{g}}\\ &= \sum_j Z_jT_j(\mathbf{s})\ \mathrm{e}^{-2\pi\mathbf{g}\cdot\mathbf{r}}-\frac{8\pi^2\epsilon h^2\Omega\mathbf{s}^2}{m_0\gamma|e|^2}U_{\mathbf{g}}\end{aligned}\tag{A.10}$$

[1] An interesting discussion with Tsirelson & Olaussen (2003) about the the validity of Eq. (A.5) motivated this appendix.

This equation gives a relation between the X-ray and electron structure factors and is usually referred to as Mott[2] formula.

References

Mott, N. F. (1930). The scattering of electrons by atoms. *Proc. R. Soc. London A* **127**, 658–665.

Spence, J. C. H. & Zuo, J. M. (1992). Electron Microdiffraction. Plenum Press, New York.

Tsirelson, V. & Olaussen, K. (2003). Private communications.

[2]In the literature this formula is also known as the Mott-Bethe formula. Some authors refer instead to the relation between electron and X-ray scattering factors, Eq. (A.8). The name has probably its origin in a relation similar to Eq. (A.8) derived by Mott (1930).

Appendix B

Structure factor error analysis

Here follows a short description of the error analysis applied to the structure factor measurements of Mg (Friis *et al.*, 2003b) and $SrTiO_3$ (Part III).

B.1 Motivation

Doing QCBED experiments, it is common to take several diffraction patterns under different experimental conditions (e.g. different geometry and sample thickness) in order to get better statistics and to be able to check the consistency of the data. From each refinement one gets a value for the standard deviation based on the depth of the χ^2 minimum. However, these standard deviations are usually underestimated, since uncertainties in the non-refined parameters are neglected. Therefore it is common to obtain the standard deviation as a simple spot check standard deviation of the measured structure factor values (Jiang *et al.*, 2003; Friis *et al.*, 2003a).

However, a more rigorous analysis, as shown in the two next sections, should also use the information in the standard deviation of the individual refinements and, more importantly, take the uncertainties in the temperature factors into account.

B.2 The expectation value and variance

Lets assume that we have performed n refinements of a certain reflection resulting in the structure factors U_i and standard deviations s_i, with $i = 1..n$. If we assign a weight w_i, with $\sum_i w_i = 1$, the weighted average of the structure factors is

$$\bar{U} = \sum_i w_i U_i. \tag{B.1}$$

It is possible to show that the expectation value and variance of the true structure factor are given by $\bar{U}$ and

$$s^2 = \sum_i w_i^2 s_i^2 + \sum_i w_i (U_i - \bar{U})^2, \tag{B.2}$$

respectively. In the analysis of Mg and $SrTiO_3$ the weighting were, as normally, simply chosen proportional to $1/s_i$, i.e.

$$w_i = \frac{1/s_i}{\sum_j 1/s_j}. \tag{B.3}$$

The expectation value of $\bar{U}$ equals the expectation value of the refinements $\mu = E(U_i)$ as seen from

$$E(\bar{U}) = E\left(\sum_i w_i U_i\right) = \sum_i w_i E(U_i) = \sum_i w_i \mu = \mu, \tag{B.4}$$

where we have assumed that the measurements U_i are independent.

Similarly, we want to show that $E(s^2)$ equals the distribution variance of the measurements $V(U_i)$. Since, the variance of $\bar{U}$ is

$$V(\bar{U}) = V\left(\sum_i w_i U_i\right) = \sum_i w_i^2 V(U_i) = \sum_i w_i^2 E(s_i^2) \tag{B.5}$$

we have

$$\begin{aligned} E(s^2) &= E\left(\sum_i w_i^2 s_i^2\right) + E\left(\sum_i w_i (U_i - \bar{U})^2\right) \\ &= \sum_i w_i^2 E(s_i^2) + E\left(\sum_i w_i (U_i - \mu)^2 - (\bar{U} - \mu)^2\right) \\ &= V(\bar{U}) + \underbrace{E\left(\sum_i w_i (U_i - \mu)^2\right)}_{V(U)} - \underbrace{E\left((\bar{U} - \mu)^2\right)}_{V(\bar{U})} \\ &= V(U) \end{aligned} \tag{B.6}$$

Q.E.D. □

B.3 Error in the final X-ray structure factors

We are often interested in X-ray structure factors at a certain temperature (e.g. at static lattice temperature where $T_j(\mathbf{s}) = 1$, $\forall j$). The Mott formula (A.10) gives the X-ray structure factor F^{initial} at the experimental temperature. In the case of only one kind of atoms (at equal site symmetry) in the unit cell, the structure factor at the wanted temperature is simply

$$F^{\text{final}} = \frac{T^{\text{final}}}{T^{\text{initial}}} F^{\text{initial}}. \tag{B.7}$$

For more than one atom in the unit cell F^{final} can be approximated by

$$F^{\text{final}} \approx \frac{\sum_j f_j T_j^{\text{final}} \, \mathrm{e}^{-2\pi i \mathbf{g}\cdot\mathbf{r}_j}}{\sum_j f_j T_j^{\text{initial}} \, \mathrm{e}^{-2\pi i \mathbf{g}\cdot\mathbf{r}_j}} F^{\text{initial}}, \tag{B.8}$$

where f_j is the scattering factor of the jth atom. Note that if only one kind of atoms is present, Eq. (B.8) reduces to Eq. (B.7).

From the Mott formula (A.10) the variance of F^{initial} is given by

$$V(F^{\text{initial}}) = \sum_j \left(Z_j \, \mathrm{e}^{-2\pi i \mathbf{g}\cdot\mathbf{r}}\right)^2 V(T_j) + \left(\frac{C\Omega s^2}{\gamma}\right)^2 V(U) \tag{B.9}$$

where

$$C = \frac{8\pi^2 \epsilon h^2}{m_0 |e|^2} = 131.2625 \text{ Å} \tag{B.10}$$

if U and $T_i^{\text{initial}}; i = 1..n$ are independent.

The temperature factor is, in the harmonic approximation, given by

$$T_j = T_j(\mathbf{s}) = \mathrm{e}^{-\beta_j^{ik} g_i g_k} \tag{B.11}$$

where $\beta_j^{ik} = 2\pi^2 \langle u^i u^k \rangle_j$ and where $\langle u^i u^k \rangle_j$ is the anisotropic displacement tensor for atom j. Summation over repeated indices is implicitly assumed according to Einsteins summation convention. The variance of T_j can now, using the Gauss approximation formula for the variance of a function of a stochastic variable X

$$V(g(X)) \approx V(X)[g'(E(X))]^2, \tag{B.12}$$

be written as

$$V(T_j) = \mathrm{e}^{-2\beta_j^{ik} g_i g_k} V(\beta_j^{ik} g_i g_k) = T_j^2 \sum_{ik} (g_i g_k)^2 V(\beta_j^{ik}) \approx \sum_{ik} (g_i g_k)^2 V(\beta_j^{ik}) \tag{B.13}$$

where we in the last step have used that T_j is close to unity at low temperatures and small scattering angles (which is the case for QCBED).

By taking the variance of Eq. (B.8) and use (B.9) and (B.12) it follows that the variance of F^{final} is given by

$$\begin{aligned} V(F^{\text{final}}) &\approx \sum_j \left(Z_j \, \mathrm{e}^{-2\pi i \mathbf{g}\cdot\mathbf{r}_j}\right)^2 V(T_j) + \left(\frac{C\Omega s^2}{\gamma}\right)^2 V(U) \\ &+ 2\sum_j \left(f_j \, \mathrm{e}^{-2\pi i \mathbf{g}\cdot\mathbf{r}_j}\right)^2 V(T_j). \end{aligned} \tag{B.14}$$

B.4 Correction due to lattice expansion

Since the structure factors depend on the lattice parameters, via the scattering factor, a small correction is needed in order to account for the change in lattice parameters, when converting structure factors between temperatures. When converting from a higher to a lower temperature, this effect tends to counteract the reduction of the structure factor, caused by the smearing accounted for by the temperature factor T_j. However, this is a very small effect of the size of the uncertainties (around 0.2% when converting from liquid nitrogen temperature to static lattice, see e.g. the rescaled values in Table 1. in Tabbernor *et al.* (1990)).

This effect can easily be accounted for by also considering the change of scattering angle in Eq. (B.8)

$$F^{\text{final}} \approx \frac{\sum_j f_j(s^{\text{final}}) T_j^{\text{final}} \, \mathrm{e}^{-2\pi i \mathbf{g}\cdot\mathbf{r}_j}}{\sum_j f_j(s^{\text{initial}}) T_j^{\text{initial}} \, \mathrm{e}^{-2\pi i \mathbf{g}\cdot\mathbf{r}_j}} F^{\text{initial}}. \tag{B.15}$$

References

Friis, J., Jiang, B., Spence, J. C. H. & Holmestad, R. (2003a). Quantitative convergent beam electron diffraction measurements of low order structure factors in copper. *Micros. and Microanal.* **9**, 379–389. Paper 1 in this thesis.

Friis, J., Madsen, G. K. H., Larsen, F. K., Jiang, B., Marthinsen, K. & Holmestad, R. (2003b). Magnesium: Comparison of density functional theory calculations with electron and X-ray diffraction experiments. *J. Chem. Phys.* **119**. In press. Paper 4 in this thesis.

Jiang, B., Zuo, J. M., Friis, J. & Spence, J. C. H. (2003). On the consistency of QCBED structure factor measurements for TiO_2 (rutile). *Micros. and Microanal.* **9**, 457–467. Paper 2 in this thesis.

Tabbernor, M. A., Fox, A. F. & Fisher, R. M. (1990). An accurate reappraisal of the elemental form factors and charge density of copper. *Acta Cryst. A* **46**, 165–170.